SYNTHESIS OF METAL NANOPARTICLES BY ELECTROLYTICAL STM AND ELECTROCHEMICAL DISCHARGES

THÈSE N° 3752 (2007)

PAR

Ashwin LAL

M.Sc. in Physics, Indian Institute of Technology Kanpur, Inde

et de nationalité indienne

EPFL

ÉCOLE POLYTECHNIQUE
FÉDÉRALE DE LAUSANNE

Lausanne, EPFL

2007

कर्मण्येवाधिकारस्ते मा फलेषु कदाचन ।
मा कर्मफलहेतुर्भूर्मा ते सङ्गोऽस्त्वकर्मणि ॥

Set thy heart upon they work, but never on its reward.
Work not for a reward; but never cease to do thy work.

Bhagavad Gita

ii

Abstract

As conventional fabrication techniques reach their limits novel techniques are needed for fabrication of structures in the nanometer range. This thesis investigates new methods to create metal nanostructures or nanoparticles with an STM tip or a sharp metal tool working inside an electrolyte. Electrochemical synthesis has the advantage that since deposition/etching are controlled by electrode potentials, it can be relatively simple to control and in addition STM allows *insitu* observation.

Mathematical models based on finite difference have been developed to estimate electric field and ion distributions in the tip-sample gap region and quantitatively describe the dominant structuring methods – (a) double-layer mixing, (b) ultra-short voltage pulses and (c) diffusion governed deposition. Further, Monte Carlo analysis is used to look at cluster formation for the particular case of 2d growth. The mathematical models provide important insights and can be used for optimization.

Experimental work with STM has been carried out on two systems – (a) deposition of Pt on graphite (HOPG) and (b) deposition of platinum on gold (Au(111)), from solutions containing chloroplatinic ions. In the case of HOPG, microsecond voltage pulses of large amplitudes ($\sim$5 V) are shown to produce local structures in the $\sim$10-100 nm range. It is shown that deposition occurs from ions adsorbed on the tip surface. In the case of Au(111), by applying a train of nanosecond voltage pulses between tip and surface, Pt clusters of $\sim$10 nm and 1-2 monolayers high can be created in a zone of $\sim$50 nm. Deposition occurs from platinic ions adsorbed on Au surface. The role of the pulse parameters, tip material and geometry and solution concentration are discussed. General rules are established for local deposition by train of ultra-short voltage pulses.

The last part of the thesis presents a method to produce metal nano particles by using electrochemical discharges. Electrochemical discharges occur under extreme current densities in an aqueous electrolyte and is characterized by a sudden breakdown of the conductivity accompanied by the formation of an insulating gas layer around the electrode. Electrical discharges occur across the gas layer. In this work, it is shown that this method is applicable to a large number of metals and is suitable for alloy nanoparticles. A simple method to control the size of the particles is developed. Metal nano particles ranging from a few nm to $\sim$200 nm can be synthesized.

Keywords : Scanning Tunneling Microscope (STM), Electrolytical STM, nanstructuring, nanoparticle, finite difference method, electrochemical discharges.

iv

Résumé

Puisque les techniques conventionnelles de la fabrication atteignent ses limites, on a besoin des techniques originales pour la fabrication des stuctures dans la gamme du nanomètre. Cette thèse est une prospection des nouvelles méthodes pour créer des nanostructures métalliques ou des nanoparticules à l'aide d'une pointe STM ou un outil métallique bien pointu immergé dans un électrolyte. L'avantage de la synthèse électrochimique est que la deposition/gravure sont controlées par les potentiels d'électrode, ça peut être relativement simple à contrôler. De plus, le STM permet l'observation *insitu*.

Les modèles mathématiques fondés sur les différences finies ont été développés pour estimer le champ électrique et la distribution des ions dans la région intersticielle de la pointe-échantillon et décrire quantitativement les méthodes dominante pour structurer – (a) interférence double-couche, (b) les pulses ultra-courts de tension et (c) la déposition qui est gouvernée par la diffusion. En plus, l'analyse Monte Carlo est utilisée pour regarder la formation des agrégats pour le cas particulier de la croissance 2D. Les modèles mathématiques fournissent un aperçu important et qui peuvent être employés pour l'optimisation.

Les expérience à l'aide de STM ont été effectuées sur les deux systèmes – (a) la déposition de Pt sur graphite (HOPG) et (b) la déposition de Pt sur or (Au(111)), des solutions contenant des ions chloroplatinique. Dans le cas de HOPG on a constaté que les pulses de tension de l'ordre de la microseconde et de grande amplitude ($\sim$5 V) produisent des structures locales de l'ordre de $\sim$10-100 nm. On a montré que la déposition se produit grâce aux ions adsorbés à la surface de la pointe. Dans le cas de Au(111) on peut crèer des agregats de Pt de $\sim$10 nm et 1-2 mono couche dans une zone de $\sim$50 nm par l'application d'une série des pulses de tension de l'ordre de la nanoseconde entre la pointe et la surface. La déposition se produit grâce aux ions platinique adsorbés sur la surface Au. Les rôles des paramètres des pulses, matériau et la géométrie de la pointe et la concentration de la solution sont discutés. Les régles générales sont établies pour la déposition locale par une série de pulses ultra-court de tension.

La dernière partie de la thèse présent une méthode pour produire des nano particules métalliques par l'usage des décharges électrochimiques. Les décharges électrochimiques se produisent sous une densité de courant extrême dans un électrolyte aqueux et qui sont caractèrisées par un brusque claquage de la conductivité accompagnée par la formation d'une couche de gaz isolant autour de l'électrode. Les décharges électriques se produisent à travers la couche de gaz. Dans ce travail, on a montré que cette méthode est applicable à de nombreux métaux et qu'elle est aussi appropriée pour le nanoparticules d'alliage. Une méthode simple pour contrôler la taille des particules a été développée. On peut produire les nanopar-

ticules de metal dans une gamme de quelques nm à ~200 nm.

Mots clé : Microscope à balayage à effet tunnel (STM), STM Electrolytique, nanostructuration, nanoparticule, méthode des différence finie, décharges électrochimiques.

Acknowledgements

During the course of this thesis work, I have been supported and helped by many people and I wish to express my gratitude towards them.

First of all I wish to thank Prof. Hannes Bleuler for providing me the opportunity to work on this thesis and for the faith he showed in me to carry out this work. I am indebted to Prof. Comninellis for introducing me to the exciting world of electrochemistry. I thank him for the support I received from him and his lab and also for pushing me when it was needed. Many thanks to Rolf Wüthrich with whom I had many discussions and exchange of ideas. I would like to acknowledge Prof. Siegenthaler for teaching me some of the 'tricks of the trade' of the electrolytical STM.

My work at EPFL started with Dr. Yoichi Miyahara, Dr. Jean-Marc Breguet and Ricardo Perez. I had an excellent experience with them. With them I got involved with STMs and AFMs and my fascination for these instruments continues to grow.

Several students did their diploma or semester work with me which helped me in no small way and with many of them I had valuable discussions. The two Dutch exchange students, Lucas Hof and Jurgen Duivenvoorden, and Lionel Flaction made important contributions.

Big thanks to our secretaries Mme Heidi Banz and Evelyn Rovero who have been most helpful and accomodating.

The workshop people, Jean-Jacques, Pascal and Claude Amendola made the fabrication of various components easy for me and their support is acknowledged.

The office and lab colleagues Hans Langen, Valia Fascio, Kenichi Fujisaki, Arvid Bergander, Laurent Sache, Francois Barrot, Ulrich Spaelter and many others made working an enjoyable experience.

I thank my parents and my sister for their constant love and encouragement. A very special and warm thanks to my wife, Shilpi, without whose patience and motivation this thesis would have been impossible. Finally I would also like to thank my little daughter, Ishi, who sometimes accompanied me in the late hours of the night as I wrote this thesis.

List of Symbols

Greek Symbols

α Transfer coefficient

ϵ_0 Electric permittivity of free space (8.854187817^{-12} F m^{-1})

ϵ_r Dielectric constant

η Transition probability from an occupied to empty state (s^{-1})

Γ Barrier transmission coefficient

λ Transition probability from an empty to occupied state (s^{-1})

μ^i Mobility for ith species (cm^2 s^{-1} V^{-1})

ω Angular velocity (rpm)

Φ Particle diameter (nm)

ψ Quantum mechanical wavefunction

ρ Charge density (C m^{-3})

σ Gaussian spread in units of lattice constant

σ_{ri} Characteristic function of the square, $\sigma_{ri} = 0, 1$

τ Voltage pulse period (μs)

τ_p Voltage pulse width (μs, ns)

Θ Mean bubble coverage fraction

θ Tip angle ($^\circ$)

φ (a) Electric potential (V, mV)
        (b) Voltage pulse amplitude (V)

φ_{sample} Sample potential (V, mV)

x

φ_{tip} Tip potential (V, mV)

$\zeta(r)$ Density of states at r

Roman Symbols

$\vec{j}^i_{diff}(\vec{r})$ Diffusional flux for ith species (s^{-1} m^{-2})

$\vec{j}^i_{em}(\vec{r})$ Electromigrational flux for ith species (s^{-1} m^{-2})

c Capacitance per unit area (μF cm^{-2})

D^i Diffusion coefficient for ith species (cm^2 s^{-1})

D^s Surface diffusion coefficient (cm^2 s^{-1})

d_{dl} Double layer thickness (Å, nm)

d_{tip} Tip diameter (nm)

E (a) Electrode potential (V)
(b) Energy of electron (eV)

e Electron charge (1.60217646 $\times$ 10^{-19} C)

$E^{0'}$ Formal electrode potential (V)

E_b Energy barrier (eV)

E_F Fermi energy level (eV)

g Tip-sample gap (nm, Å)

h Planck's constant (6.626068 $\times$ 10^{-34} m^2 kg s^{-1})

I Current (A)

I_T Tunneling current (nA)

I_{crit} Critical Current (A)

j Current density

J_T Tunneling current density (A m^{-2})

k^0 Standard reaction rate constant (cm s^{-1})

k^0_t True standard reaction rate constant (cm s^{-1})

k_B Boltzmann constant (1.3806503 $\times$ 10^{-23} m^{2}kg s^{-2} K^{-1})

m mass (kg)

n Number of atoms

n^i Number concentration for i^{th} species (nm^{-3})

$p^*(m)$ Probability ratio, mass m to mass zero, of being in reaction zone

P_i Probability of occupation of site i

$p_m(r)$ Probability density for mass m particles at r

q^i Number of electronic charges on i^{th} species

r_i Electrochemical cell inner radius (mm)

r_o Electrochemical cell outer radius (mm)

r_r Radius upto which reaction can occur (mm)

r_{tip} Tip radius (nm)

s Potential barrier width (Å)

T Temperature (K)

t time (s)

U_0 Potential energy barrier (eV)

U_m Energy barrier (eV)

V Potential difference (V)

V_d Water decomposition potential (V)

V_{crit} Critical Voltage (V)

w Mean potential energy barrier above the Fermi level (eV)

W_m Potential energy for a particle of mass m (J)

x_H Distance to Helmholtz plane (Å)

x_{IHP} Distance to inner Helmholtz plane (Å)

x_{OHP} Distance to outer Helmholtz plane (Å)

Contents

Chapter 1

Introduction

Nanotechnology holds the promise to entirely new generation of products that are stronger, faster, lighter, more efficient and more precise. As conventional fabrication techniques reach their limits novel techniques are needed for fabrication of structures in the nanometer range. Scanning probe microscopes, originally used for imaging, have been successfully used to modify surfaces at the nanometer scale. While SPM based nanostructuring is a serial process and therefore slow, it can nevertheless be used to create test structures and moreover they offer the opportunity to manipulate the surface at the smallest scale i.e. atom by atom. A key advantage of SPM based structuring is that one can visaulize and characterize the structure *insitu*. Arrays of simultaneously operating tips can overcome the speed issue and open several applications. In this respect it is interesting to look at the "Millipede" project from IBM® – a new high density data storage system (upto 1 Terabit/in^2) based on a large array of AFM cantilevers [1]. 'Bits' are 'written' on a polymer media by individual cantilever tips using a thermal mechanism. The same cantilevers 'read' the bits as well.
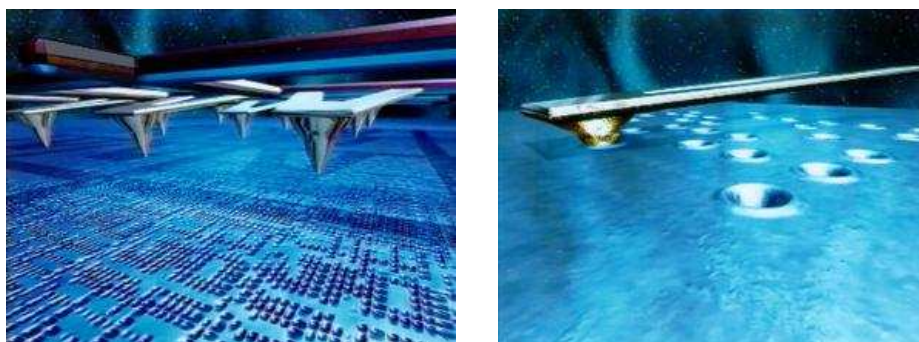

Figure 1.1: An animated view of the Millipede nanomechanical storage device illustrates how an individual tip creates an indentation in a polymer surface (right) and how a large number of such tips are operated in parallel (left). Courtesy of IBM® Zurich Research Laboratory. Unauthorized use not permitted.

It has been shown that an STM tip or a sharp metal tool operating inside an electrolyte can be used to modify surfaces locally. As the deposition/etching are controlled by elec-

trode potentials, it can be relatively simple to control. Since the electrochemistry can vary strongly from system to system, a wide variety of ways have been developed to create localized structures [2, 3]. Prominent among these methods are (a) jump-to-contact, (b) dissolution from tip, (c) double-layer cross talk, (d) defect induced and (e) ultra-short voltage pulses. Depositions in the 10-100 nm range and etching to sub-μm precision have been achieved.

On another note, there is considerable research on noble metal nano particles for their use as electrocatalysts, e.g. for fuel oxidation and oxygen reduction in low temperature fuel cells. In this scope this thesis presents some new electrochemical methods to fabricate metal nanoparticles. Due to the interest in platinum nanoparticles, it has been chosen for investigation. The thesis can be divided into two parts – (a) localized nanoparticle generation with electrolytical STM and (b) creation of nanoparticles by electrochemical discharges.

Nanoparticle formation with ESTM

The first part of the thesis deals with local metal deposition with an STM tip operated in an electrolyte.

Chapter 2 is devoted to background and literature survey. It starts with an introduction to the STM and it's principle. The chapter looks at some nanostructuring examples by STM or AFM in air or vacuum. There is a section on electrolytical STM and its role in electrochemistry. A large section of the chapter is devoted to STM based nanostructuring methods developed to work in electrolyte. The chapter also contains a general introduction to nanoparticles and common methods for their sysnthesis.

Chapter 3 describes quantitatively many of the electrolytical STM based nanostructuring methods. It starts with equilibrium electrostatic field distribution in the tip-substrate region first in a dielectric medium and then in an electrolyte. The latter case is a solution of the Poisson Boltzmann equation and gives the *double layer* mixing, an effect which has been used for local dissolution of metals [4, 5]. It next looks at the dynamics – time evolution of fields and charge densities in the STM tip-substrate gap, focussed towards the initial phase after potential modification, corresponding to ultra-short voltage pulses. Another section describes the role of diffusion in the tip-substrate geometry particularly for replenishment and deposition from tip. The chapter ends with a look at cluster formation for the particular case of 2d growth. The results from the modelling are connected to the experiments described in subsequent chapters.

Most experimental work regarding STM was done with a home built STM. The STM instrumentation is described in chapter 4. The STM was designed specially to have very low drift in electrolyte and to offer high degree of control to carry out different structuring tasks. The STM is controlled by a linux based open source and freely available software called GXSM [6]. The chapter also describes procedures to prepare tips for use in electrolyte.

Experimental work done on two systems - (1) Pt deposition on graphite (HOPG) and (2) Pt deposition on gold (Au(111)) from $[PtCl_6]^{2-}$ containing solutions are described in chapters 5 and 6 respectively. The two systems differ radically from each other. In the case of Pt on HOPG, the conclusion is that local deposition occurs from Pt ions adsorbed on the tip and is aided by prior defect generation. This is close to the system Ag on HOPG investigated earlier [7, 8]. In the case of Pt on Au(111) a novel idea, based on nanosecond

pulses [9], is introduced – to convert, locally, metal ions adsorbed on the substrate surface by using a train of nanosecond voltage pulses. The role of pulse parameters has been investigated and general rules to control the deposition are established.

Nanoparticles by electrochemical discharges

In the second part of the thesis, a method to produce nanoparticles from electrochemical discharges is presented. Electrochemical discharges occur under extreme current densities in an aqueous electrolyte. The phenomenon is characterized by a sudden breakdown of the conductivity accompanied by the formation of an insulating gas layer around the electrode [10]. Discharges or sparks occur across this gas film. If the electrolyte contains metal salt and if the working electrode is the cathode, while most of the discharge current is used up for production of H_2 bubbles, a part of it converts M^+ to M which group to form clusters. The clusters are prevented from depositing on the electrode surface by the gas film. The method has been used for several metals and allows to create particles from 10-150nm. A mechanism to control the size has been developed based on rotation speed of the working electrode. It is estimated that this method should allow to control the size of particles to $\sim$10 nm quite easily.

Chapter 2

Literature Review

Nanotechnology, in a way, owes it's birth to the invention of the Scanning Tunneling Microscope (STM). Invented by Binnig and Rohrer in 1981, the STM allows "seeing" the surface of a conducting solid with atomic resolution [11, 12, 13]. The development of this technique led to the invention of a family of microscopes called scanning probe microscopes (SPM). SPMs utilize a fine probe which is brought in close proximity to the surface of the sample and scanned over the surface. Interactions between the probe and the surface are used to generate a view of the surface. The STM uses quantum tunneling between conducting tip and surface to generate the surface topography. Atomic Force Microscope (AFM) is another member of this family. Invented in 1986 by Binnig, Quate and Gerber [14], the AFM uses atomic forces between a cantilever and the surface to generate images of the surface. Both STM and AFM can provide very high lateral and vertical resolution down to sub-nanometer range. SPMs are quite versatile; they can be adapted for different environments like vacuum, liquids and can be utilized not only for imaging but also for nano-structuring, nano-manipulation and for determining physical properties at the nanometer scale. Binnig and Rohrer received the Nobel Physics prize for their invention in 1986.

2.1 STM principle

The principle behind the STM is quantum mechanical tunneling. If there exists a potential energy barrier higher than the energy of a particle, then, according to classical physics, the particle can not traverse the barrier. But quantum mechanically, there is a non-zero probability for actually "tunneling" through the energy barrier. When an STM tip (metal wire) is brought close to a conducting substrate, while still not touching it, the electrons see an energy barrier at the tip-substrate gap. This section describes how the tunneling current can be calculated in a simple case showing the dependencies on barrier height and width.

Elastic tunneling through a 1-d rectangular potential barrier

[The section closely follows the description by Wiesendanger [15] and for more details the reader may refer to it and the references cited within.]
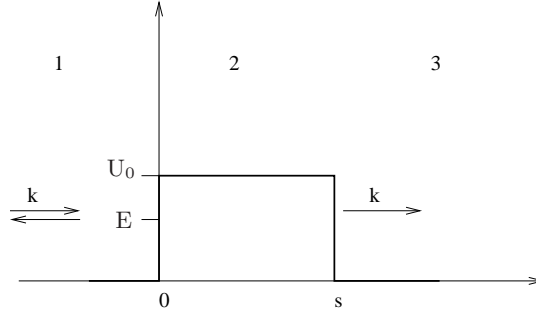
Figure 2.1: One-dimensional potential barrier with height U_0 and width s.

Consider a 1-d potential barrier as shown in in Fig. 2.1 where an electron is incident from the left side with known energy, E and mass m. Assuming elastic tunneling, i.e. the energy of the electron is unchanged, we can write the time-independent Schrödinger equations for the electron wavefunctions, ψ_j, for the three regions ($j = 1, 2, 3$). For region 1:

$$-\frac{\hbar^2}{2m}\frac{d^2\psi_1}{dz^2} = E\psi_1$$
$$\psi_1 = e^{ikz} + Ae^{-ikz}$$
$$\text{with } k^2 = 2mE/\hbar^2.$$

(2.1a)

For region 2:

$$-\frac{\hbar^2}{2m}\frac{d^2\psi_2}{dz^2} + U_0\psi_2 = E\psi_2$$
$$\psi_2 = B'e^{ik'z} + C'e^{-ik'z} = Be^{-\kappa z} + Ce^{\kappa z}$$
$$\text{with } \kappa^2 = -k'^2 = 2m(U_0 - E)/\hbar^2.$$

(2.1b)

For region 3:

$$-\frac{\hbar^2}{2m}\frac{d^2\psi_3}{dz^2} = E\psi_3$$
$$\psi_3 = De^{ikz}$$

(2.1c)

where $\hbar$ is Planck's constant divided by 2π.

For tunneling, the interesting quantity is the ratio of the transmitted current j_t to the incident current density j_i, denoted as Γ and called the barrier transmission coefficient.

$$j_t = -\frac{\hbar^2}{2m}\left(\psi_3^*(z)\frac{d\psi_3}{dz} - \psi_3(z)\frac{d\psi_3^*}{dz}\right)$$
$$= \frac{\hbar k}{m}|D|^2$$
$$j_i = \frac{\hbar k}{m}$$

(2.2)

and therefore

$$\Gamma = \frac{j_t}{j_i} = |D|^2 \tag{2.3}$$

D and therefore Γ can be calculated exactly by matching the wavefunctions ψ_j and their first derivatives $d\psi_j/dz$ at the points $z = 0$ and $z = s$ where there are discontinuities in the potential.

$$\Gamma = \frac{1}{1 + (k^2 + \kappa^2)^2/(4k^2\kappa^2)\sinh^2(\kappa s)} \tag{2.4}$$

Under the approximation of $(\kappa s \gg 1)$ which means the transmitted current is much smaller than the incident current or *strongly attenuating barrier*

$$\Gamma \approx \frac{16k^2\kappa^2}{(k^2 + \kappa^2)^2}e^{-2\kappa s} \tag{2.5}$$

with the decay rate

$$\kappa = [2m(U_0 - E)]^{1/2}/\hbar$$

The dominating term in Γ is the exponential part $\exp(-2\kappa s)$. The exponential dependence of Γ on the barrier width s and the square root of an "effective" barrier height $(U_0 - E)^{1/2}$ is typical for tunneling. For a barrier width of 5 Å and an effective barrier height of 4 eV, the exponential factor is about 10^{-5}. A 1 Å change in the barrier width then leads to a change in Γ by an order of magnitude. The extreme sensitivity to the barrier width is the reason why an STM can "see" features at the Å level.

For small Γ, perturbation method can be applied to calculate the tunneling current. Bardeen [16] considered two wavefunctions ψ_l and ψ_r to the left and right of the barrier respectively, with the following conditions :

ψ_l is the exact solution of the Schrödinger equation for $z \leq 0$ but decays in the region $z \geq 0$ and ψ_r is the exact solution of the Schrödinger equation for $z \geq s$ but decays in the region $z \leq s$.

$$\begin{aligned}
\psi_l(z) &= ae^{-\kappa z}; z \geq 0 \\
\psi_r(z) &= be^{\kappa z}; z \leq s
\end{aligned} \tag{2.6}$$

Assuming that the electron is initially in state ψ_l, one then calculates the transition rate from ψ_l to ψ_r using the time-dependent Schrödinger equation:

$$H\psi = i\hbar\frac{d\psi(t)}{dt} \tag{2.7}$$

with

$$H = (H_l + H_r) + H_T = H_0 + H_T$$
$$H_0\psi_l = E_l\psi_l$$

where H_l and H_r are the Hamiltonians for the left and right of the barrier respectively and H_T is the Hamiltonian representing the barrier. Considering tunneling from ψ_l with energy E_l to ψ_r with energy E_r we can write the complete wavefunction as

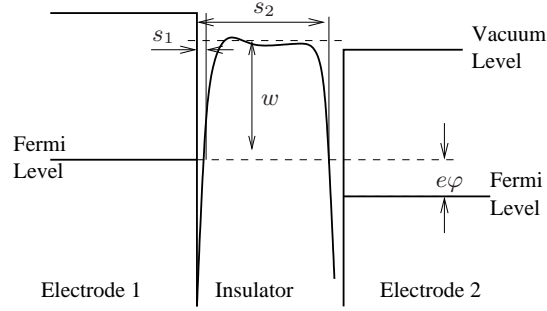$$\psi(t) = c(t)\psi_le^{-iE_lt/\hbar} + d(t)\psi_re^{-iE_rt/\hbar} \tag{2.8}$$

Figure 2.2: General tunnel barrier between two metal electrodes. From reference [17].

Then using Eq. (2.7) one gets

$$M_{rl} = \int \psi_r^*(H - E_l)\psi_l dz = \int \psi_r^* H_T \psi_l dz \qquad (2.9)$$

as the effective tunneling matrix element. For strongly attenuating potential barriers, Fermi's 'golden rule' gives the following expression for the transmitted current:

$$j_t = \frac{2\pi}{\hbar}|M_{rl}|^2 \frac{dN}{dE_r} \qquad (2.10)$$

where $\frac{dN}{dE_r}$ is the density of states on the right side of the barrier. From this one can loosely say that the tunneling current is proportional to the electronic density of states $\frac{dN}{dE_r}$.

For the metal-insulator-metal junction, Simmons [17] calculated the tunneling current density. In the low bias voltage range ($\varphi \sim 0$ i.e. $e\varphi \ll w$)

$$J_T = \frac{e^2}{4\pi^2\hbar^2} \cdot \frac{(2mw)^{1/2}}{s} \cdot \varphi \exp(-Aw^{1/2}\Delta s) \qquad (2.11)$$

where φ is the bias voltage applied, $A = 2 \cdot (2m)^{1/2}/\hbar$, w is the mean potential barrier above the Fermi level E_{F_1} of the negatively biased electrode and $\Delta s = s_2 - s_1$ is the effective gap between the electrodes (Fig. 2.2). In reality the tunneling current between two conducting electrodes will also depend on the band structure of the electrodes and the gap.

2.2 SPM for nano structuring

The STM and in general SPMs have allowed the visualization of surfaces with unprecedented resolution. They have been successfully applied to solve surface structures for all kinds of substrates. Starting from metals and semiconductors, SPMs have also been applied to organic material, from small molecules to supramolecular assemblies on surfaces. SPMs are also used to study thin film growth, surface diffusion and other phenomona that occur on the surface. Normally SPM characterization of a surface is done ensuring that the interaction is small enough to avoid irreversible changes to tip or sample. By increasing the tip-sample interaction
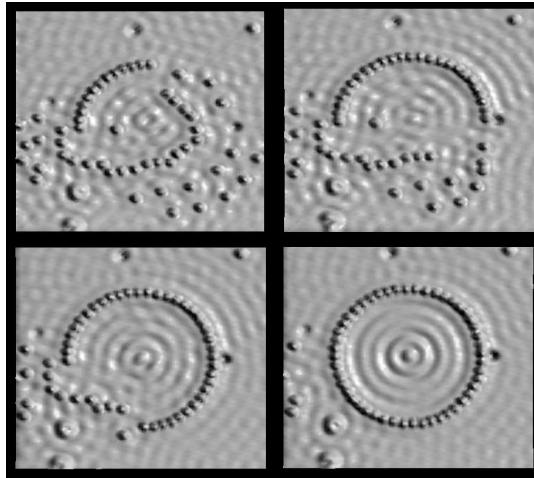
Figure 2.3: Various stages during the construction of the circular corral – Iron on Copper (111). From reference [21].

above a critical value, the sample can be modified locally. These local modifications can be controlled to nanometric sizes leading to nanostructuring by SPMs. While SPM based nanostructuring is a serial process and therefore slow, it can nevertheless be used to create test structures and moreover they offer the opportunity to manipulate the surface at the smallest scale i.e. atom by atom. A key advantage of SPM based structuring is that one can visaulize and characterize the structure *insitu*. With the microfabrication of large arrays of SPM probes, parallel processing becomes possible which could reduce the problem of speed. Wiesendanger [18] provides a summary of several SPM based nanostructuring methods and this section is partly based on that reference.

Scratching and indentation

If the tip of an STM or AFM is scanned while it is in contact with the substrate, i.e. a large interaction exists, sub-micrometric features can be drawn on the surface by scratching. For an STM this way of structuring was first shown by using a tungsten tip penetrating into a thin insulating film of polycrystalline calcium fluoride deposited on a silicon substrate [19]. Similar method for an AFM was first shown by the local removal of a monomolecular film of octadecyl phosphate deposited on mica by increasing the applied force above 10^{-6} N while scanning the surface [20]. Indentations can be performed by STM or AFM at predecided spots by increasing tip-sample interaction. Infact nano indentation is now commonly applied to test the mechanical properties of materials.

Manipulating single atoms

Manipulation of single atoms by STM tip was first demonstrated by Eigler and Schweizer [22] using a low temperature UHV STM. They studied the system Xe adsorbed on Ni(110). Under tunneling current of ~1 nA and bias voltage of 10 mV, imaging is possible without
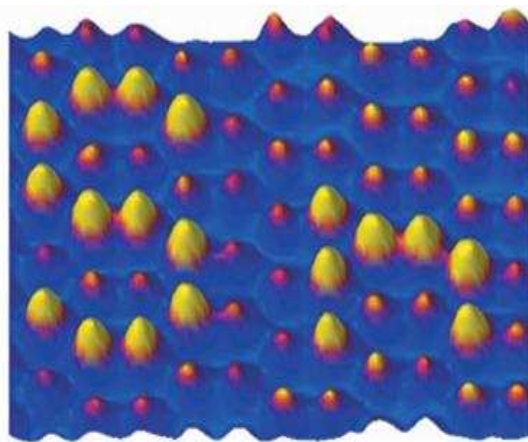
Figure 2.4: Topographic NC-AFM image showing rearranged Sn atoms on Ge(111). Image size is 7.7×7.7 nm^2. From reference [23].

disturbing the surface. To move the Xe atom on the surface the tip is first positioned on the selected Xe atom; the interaction force is then increased by increasing the tunneling current to $\sim$16 nA; the tip is moved laterally maintaining the current; and finally the Xe atom is released by retracting the tip. The force between the tip and the atom being moved is critical. It has to be large enough to overcome the energy barrier to the neighbouring substrate lattice position but small enough to prevent transfer of atom to tip. Fig. 2.3 shows the result of atom by atom manipulation [21].

Sugimoto et al. [23] have reported the use of AFM in the *non-contact* mode to perform well-controlled lateral manipulations of single atoms at room temperature. They could move substitutional Sn adatoms in the Ge(111) surface. They could induce directional diffusion of Sn atoms to the neighbouring position by scanning at a stronger attractive interaction force. These induced diffusion processes are produced by the "concerted interchange between the Sn and Ge atoms in the surface plane". Fig. 2.4 shows figure *Sn* written by Sn atoms on Ge(111) by their method.

Chemical modification

The STM tip can be thought to provide a local 'beam' of low energy electrons. This can be used to create chemical reactions on a surface providing another method to create nanostructures. One of the first investigation of controlled fabrication of nanometer-scale structures by STM was performed on glassy $Pd_{81}Si_{19}$ alloy [24]. The substrate surface is believed to consist of hydrocarbons and carbon-oxygen species with a thickness of about 2 monolayers. The authors could draw conducting carbon lines on the surface by operating the STM with a tunneling current of about 10 nA and a bias voltage of 100 mV. The result was attributed to polymerization of the hydrocarbon film which apparently acts as an electron beam resist (Fig. 2.5).

Another example of chemical modification by STM is the formation of holes on a graphite
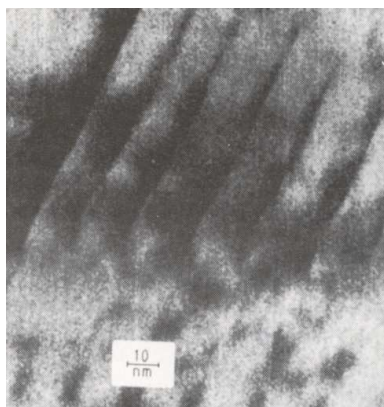
Figure 2.5: SEM image of lines written by STM on a glassy $Pd_{81}Si_{19}$ substrate [24].

surface [25, 26]. In ambient atmosphere, by applying voltage pulses (3-8 V, 10-100 μs) between tip and graphite surface during tunneling conditions, one or more layers of graphite can be removed in a small region of nanometer size just below the tip. This and similar work are discussed in a later section.

Thermal writing

Mamin [27] has reported the use of resistive heating of an AFM tip to write structures on polycarbonate. In their method an electrically conducting silicon cantilever is used and heated by passing current through it. Input power of about 40 mW can raise the temperature of the tip to 170℃. Heated tip in proximity with polycarbonate melts the substrate locally. This method can be used to 'write' structures in the sub 100 nm range. In conjunction with an array of microfabricated cantilevers this idea is potentially applicable for high density data storage system [1].

2.3 STM in electrolyte

[Based largely on the review article by Kolb [28].]

The first STM images were taken in UHV and soon after in ambient conditions. Shortly after the invention of the STM, it was realized that the STM should also work in solution [29, 30, 31]. Electrochemists saw the large possibilities that an STM working in an electrolyte could provide. To make an STM work in an electrolyte, there are some problems that have to be overcome. The STM tip in an electrolyte is another electrode where electrochemical reactions can occur leading to a faradaic current. This current could overshadow the tunneling current. The most important point therefore is to ensure that the tip area exposed to the electrolyte is so small that faradaic currents are lower than tunneling current. This is achieved by coating most of the tip with an isolating skin, e.g. made of glass, an electrophoretic paint [32], or Apeizon wax, a chemically inert thermoplast [33, 34]. Ofcourse the tip apex has to
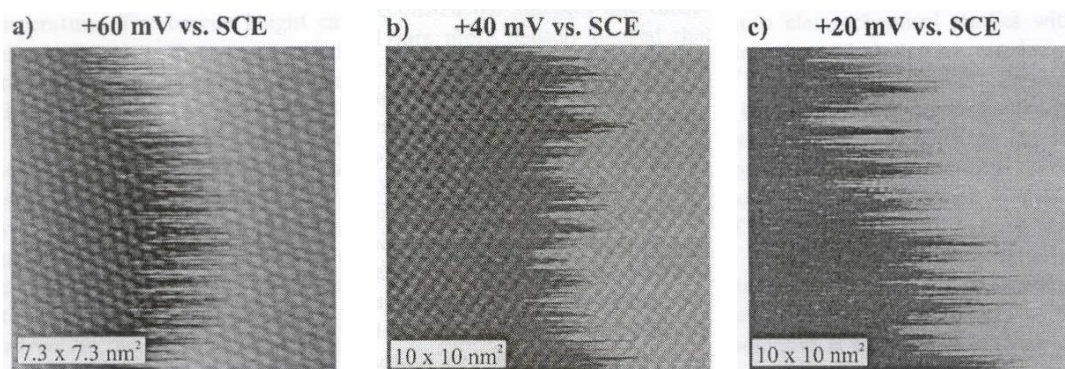
Figure 2.6: STM images of frizzy steps on (a) Ag(111), (b) Ag(100) and (c) Ag(110). Electrolyte : 0.05 M H_2SO_4 + 0.1 mM (a) or 1mM (b,c) $CuSO_4$. From reference [35].

be free of insulation. The methods usually adopted to insulate the tip leave an area of about $10^{-8}-10^{-7}cm^2$ which gives faradaic currents of normally less than 50 pA. This is considerably smaller than the tunneling currents normally used for imaging (1-10 nA). Another important point is to be able to control the tip potential with respect to the electrolyte or a reference electrode. This allows to maintain the tip potential in the double-layer charging region where there are no electrochemical reactions and hence zero faraidic current. This requires the use of a bipotentiostat. With potentiostatic control one can also control the state of the tip surface with respect to surface adsorbtion of ionic species. This can also have an impact on STM results. Following are some examples of studies done with the electrolytical STM (ESTM).

Surface dynamics

Fig. 2.6 shows atomic resolution images of Ag(111), Ag(100) and Ag(110) in sulfuric acid solutions. Interestingly monoatomic steps appear *frizzy*. Such frizzy steps in Ag(111) and Cu(100) have been studied in UHV and it has been attributed to the rapid movement of kink sites [36]. The kink diffusion is rapid on the time scale of STM imaging. Similar effects have been observed for Cu(100) in sulfuric acid [37] where two regimes were identified. At low electrode voltages atomic motion is restricted alongside the step edges while at higher potentials atoms are exchanged with terrace atoms and neighbouring steps. In the case of Au(111) in sulphuric acid it was found that steps are non-frizzy but become frizzy upon addition of chloride ions at potentials where concentration of adsorbed Cl^- is high [38].

Surface reconstruction

It is well known that surface atoms often deviate from the lattice arrangement of the bulk crystal. Two possiblities exist : *surface relaxation* - only the interatomic distance at the surface is different from bulk and *surface reconstruction* - when the surface atoms rearrange to form a different structure compared to the bulk. These happen in order to minimize the surface energy. Surface reconstruction is considered as a phase transition between two surface
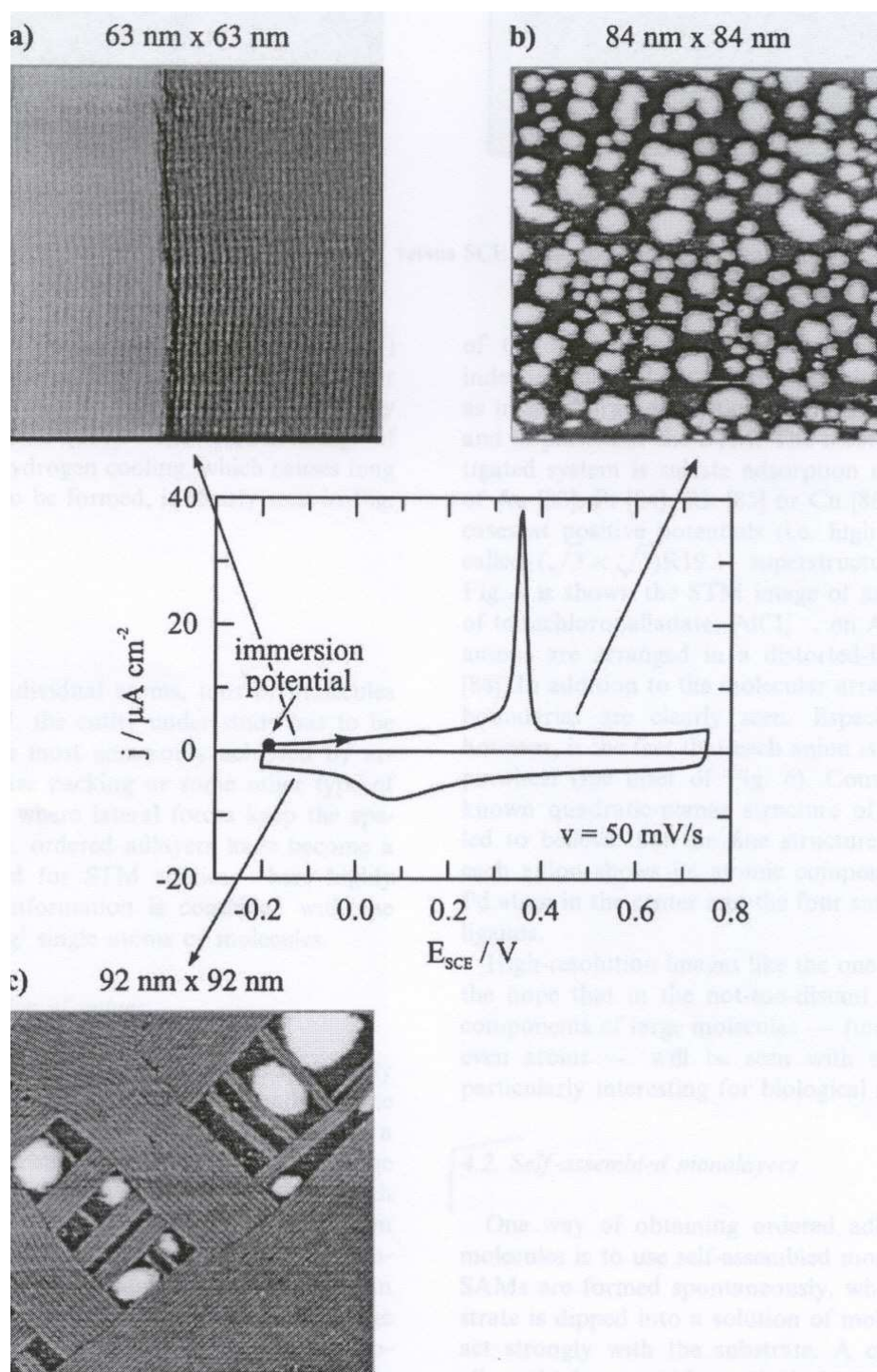
Figure 2.7: Sequence of STM images for Au(100) in 0.1M H_2SO_4 showing potential induced surface reconstruction. From reference [39, 28].
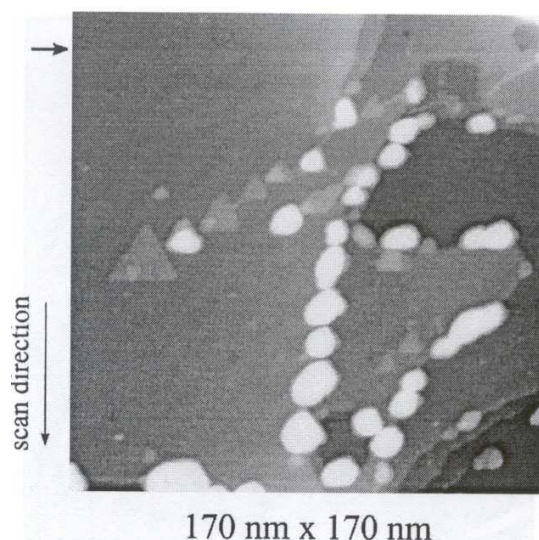
Figure 2.8: STM imag of Au(111) in 0.05 M H_2SO_4 + 0.2 mM $CuSO_4$ after stepping the potential from +0.01 to -0.31 V versus Cu/Cu^{2+} (marked by arrow). From reference [28].

states and can be induced thermally or by electrode potential in the case of electrochemical systems. Fig. 2.7 shows a sequence of STM images for Au(100) in 0.1 M H_2SO_4: (a) freshly prepared reconstructed surface, (b) the unreconstructed surface immediately after lifting of the (hex) structure and (c) potential induced reconstruction [39]. In the case of Au(100), normally the surface is reconstructed with top layer exhibiting a quasi hexagonal Au(100)-(5×20) 2-d structure. It contains about 24% more atoms than the unreconstructed Au(100)-(1×1). Owing to the misfit between the top layer and the underlying layers there is also a larger periodicity visible in the form of reconstruction rows with corrugation length of 1.45 nm. When the surface reconstruction is lifted, the excess atoms form monoatomic high islands.

Metal deposition and oxide formation

For metal deposition on a substrate, defects act as the preferred sites for nucleation and growth. With the STM it becomes possible to view the initial stages of metal deposition in real time and sometimes even with atomic resolution. This can offer important insights into the process of metal deposition - allow to validate the growth mode, understand the role of defects etc. There are several reports of *insitu* STM imaging during electrodeposition of metal - Pb on Ag , Ag on HOPG, Ag on Au, Cu on Au, Pd on Au, Pt on Au etc [40, 41, 42]. Fig. 2.8 shows an STM image of Au(111) in 0.05 M H_2SO_4 + 0.2 mM $CuSO_4$ during Cu deposition, where the preferential growth at monoatomic high steps is visible. Relatively large quantity of Cu can grow on defects before there is growth on the terraces. It is remarked that the STM tip acts as a diffusional barrier for ions in the electrolyte and therefore metal deposition just below the tip may be slowed down compared to deposition away from the tip.
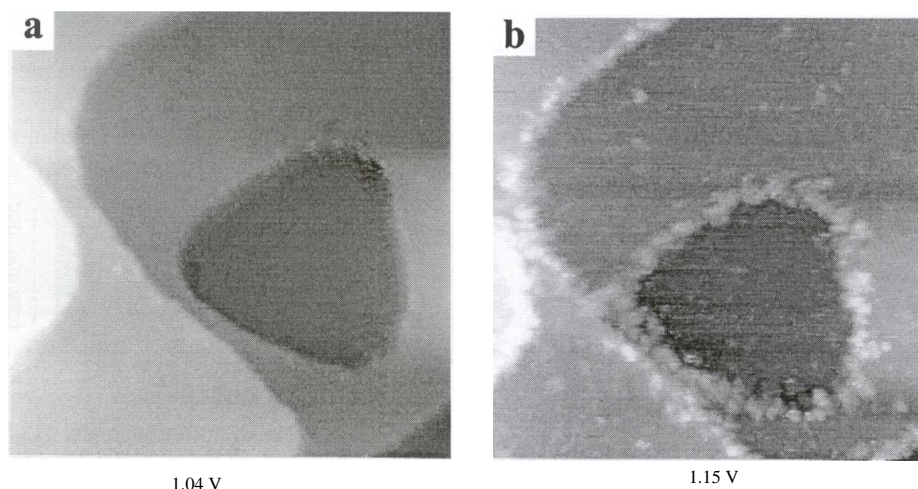
Figure 2.9: 100 nm × 100 nm STM images of Au(111) showing the onset of oxidation at the steps. From reference [43].

Another process studied by electrolytical STM and similar to metal deposition is the early stages of oxide formation on metal. Similar to metal deposition, oxide formation also starts via nucleation and growth at defect sites. STM studies of oxidation is hampered by the obvious problem that the surface becomes non-conducting and therefore such studies have to be restricted to only the very early stages. Fig. 2.9 shows two STM images for Au(111) in 0.1 M H_2SO_4 at 1.0 and 1.15 V, which is just before and after the first oxidation peak [43]. At 1.15 V oxide formation is visible on the step edges. The authors concluded that two oxidation peaks at 1.10 and 1.28 V versus SCE for Au(111) in 0.1 M H_2SO_4 do not correspond to two different valence states of oxygen on the surface, but rather to oxide formation at steps and at terraces.

Ordered adlayers

One area where the electrolytical STM has been put to use is in characterizing ordered adlayers. In Fig. 2.10 is shown the STM image of an ordered adlayer of tetrachloropalladate, $PdCl_4^{2-}$, on Au(100) where the anions are arranged in a distorted-hexagon structure [42]. In addition to the molecular arrangement, domain boundaries are clearly seen. Further each anion is imaged as a little pinwheel (see inset of Fig. 2.10) indicating that Pd atom is in the center surrounded by chloro-ligands. Several organic compounds form self assembled monolayers (SAM) on metals. Due to their potential applications in chemical sensing and biology, alkanethiols have been widely studied by STMs because of its ability to characterize surface with molecular or atomic resolution [45]. Fig. 2.11 shows STM image of ethanethiol on Au(111) in 0.1 M H_2SO_4 at 0.2 V versus SCE [44].
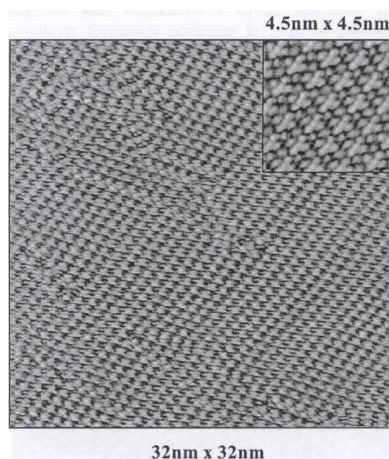
Figure 2.10: STM image of Au(100) in 0.1 M H_2SO_4 + 0.1 mM $PdCl_4^{2-}$ + 0.4 mM HCl at 0.61 V versus SCE. The surface is covered by tetrachloropalladate ions. From reference [42].
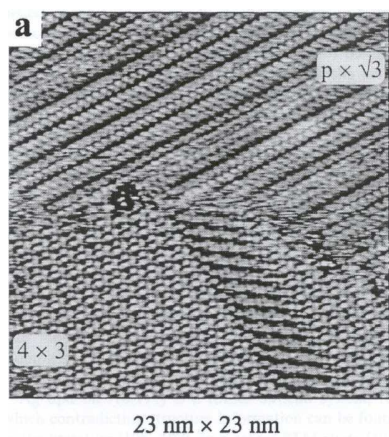

Figure 2.11: STM image of Au(111) electrode covered with a momolayer of ethanethiol in 0.1 M H_2SO_4 at +0.2 V versus SCE. Two different structures, $(p \times \sqrt{3})$ and (4×3) are visible. From reference [44].

Tunneling spectroscopy

Electrolytical STMs are also being used for tunneling spectroscopy studies. Distance tunneling spectroscopy (current vs tunnel distance) gives potential barrier information in the tunnel gap. This has been used to determine the electrolyte structure - water layer and the adsorbate layer - to a distance of about 1 nm at the metal/solution interface [46, 47]. As an example, Hugelmann and Schindler [48] have shown that for reconstructed Au(111) surface in perchloric acid, the tunnel potential barrier has an oscillating nature which they attributed to layering of water molecules. Voltage tunneling spectroscopy (current vs bias voltage) provides information about the local density of electronic states. In an electrolyte it is more difficult due to additional currents from double-layer charging and electrochemical reactions. However with careful tip preparation and deoxygenation of the solution, spectroscopy data has been obtained in some systems for a reasonable potential window [49]. In voltage contact spectroscopy the tip is used to form an electrical contact with e.g. a nanostructure. It enables *insitu* electrical characterization of the structures [49].

2.4 Nanostructuring with ESTM

Over the last decade electrochemists have made increasing use of the ESTM for nanostructuring electrode surfaces. Various approaches have been developed. Budevski et al. [3] [50] have classified the methods into three groups (Fig. 2.12):

- Probe induced techniques – This is characterized by an initial Me deposition on the SPM probe from the electrolyte and a subsequent transfer of a relatively small number of Me atoms from the probe to the substrate surface below the probe forming zero-d Me cluster.

- Field induced techniques – An inhomogeneous electric field distribution between the SPM probe and substrate can locally change the structure of (1) the STM tunneling gap, (2) structure of the electrochemical double layers at the ESTM-tip/electrolyte and substrate/electrolyte interfaces, (3) the Me^{z+} concentration within the gap and/or (4) the charge carrier density and distribution of the underlying substrate domain. The last effect is especially noteworthy in the case of semiconductor substrates. For this technique, relatively high electric voltages are necessary which may also cause surface defects.

- Defect induced techniques – This is characterized by a mechanical production of small surface defects of different dimensionality which can act as nucleation centres in the subsequent local Me deposition.

In a more recent review, Kolb and Simeone [2] discuss seven different ways of SPM based nanostructuring currently being employed by electrochemists. These methods are summarised in Fig. 2.13.

A survey of nanostructuring methods based roughly on the classification presented in [3] and [2] is presented below. Sometimes one or more of these methods are combined to create nanostructures.
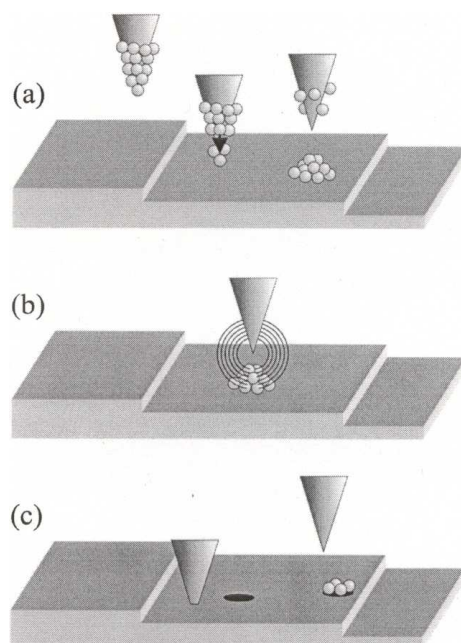
Figure 2.12: Different *in situ* SPM techniques for local nanostructuring. (a) probe induced, (b) field induced and (c) defect induced. From reference [3].
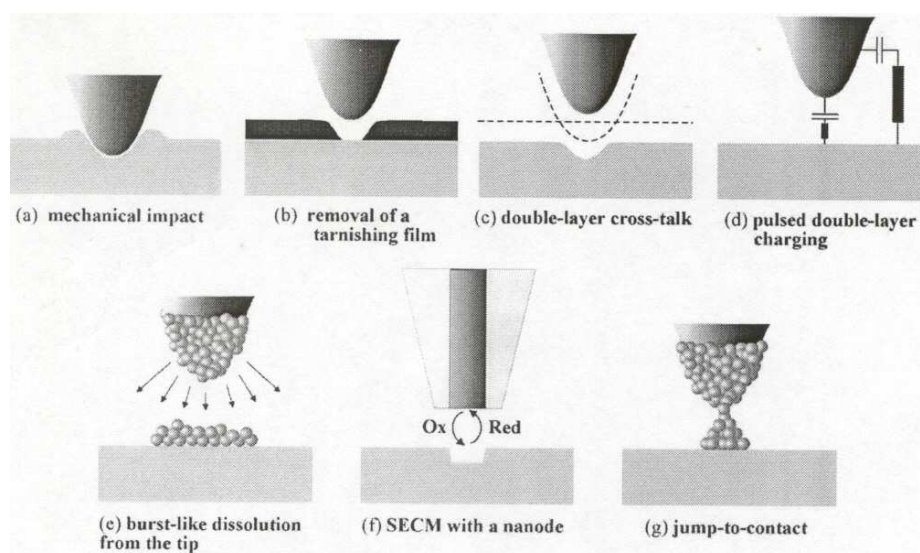

Figure 2.13: Schematic representation of the various approaches to nanostructuring electrode surfaces via an STM. From reference [2].
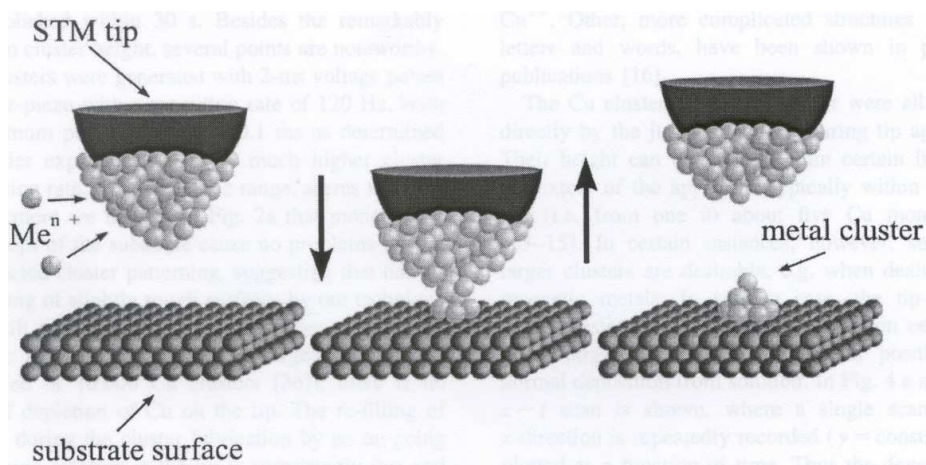
Figure 2.14: Schematic diagram of the suggested mechanism for cluster generation by a jump-to-contact. From reference [51]

Tip based methods

Jump to Contact

This method was developed by Kolb et al. [52] [53, 54, 55, 56, 51] and is based on the "jump-to-contact" between tip and substrate (Fig. 2.14). The STM tip is maintained at a potential slightly negative of the equilibrium potential $E_{Me/Me^{n+}}$. Hence there is metal deposition on the tip from the solution. This 'loaded' tip is brought close to the substrate surface. A connective neck is formed between tip and substrate which breaks when the tip is retreated, leaving behind on the substare surface a small metal cluster. The tip is automatically 'reloaded' because of the ongoing metal deposition. Some of the salient features of this method are

- It has been demonstrated that cluster deposition can be done at kHz rates. e.g. an array of 10,000 Cu clusters on Au(111) has been deposited in a few minutes [55].

- Inspite if metal loading on the STM tip, the imaging quality of the STM remains good. *Insitu* visualization is possible.

- The cluster size can be varied to an extent by changing the tip approach distance.

- Deposited clusters are highly stable. This means that they do not dissolve at potentials slightly positive of the Nernst potential. So the substrate can be kept at potentials slightly positive of the Nernst equilibrium, typically at +10 mV for Cu/Cu^{++} in the case of copper. This prevents normal electrodeposition of metal on substrate.

- Two kinds of jump-to-contact are possible depending on the cohesive energies metal-substrate and metal-metal. Jump-to-contact occurs from tip to sample (e.g. for Cu and a gold electrode) or from the substrate to the tip (e.g. for Ni on tip and gold electrode).
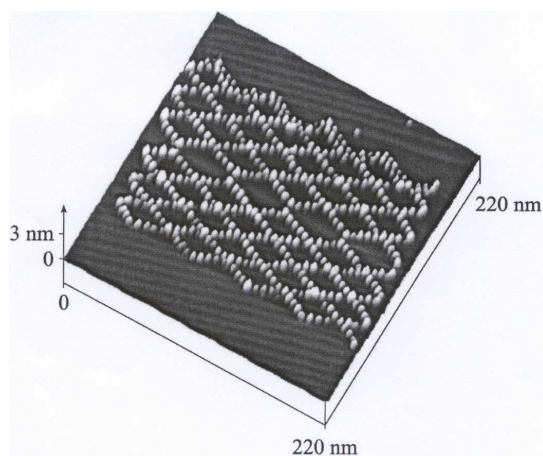
Figure 2.15: STM image of about 400 Cu clusters on Au(111) created by the "jump-to-contact" method. From reference [51].

- Several systems have been investigated for deposition by this method – Cu/Au(111), Cu/thiol covered Au(111), Ag/Au(111) and Ni/Au(111) [51], Pd/Au(111), Cu/Ag(111), Pb/Au(111), Pb/Ag(111) [54].

Dissolution from tip

In another method using the idea of transfer from tip, Schindler et al. [57] [58] have shown that Co clusters could be grown on Au. In a two-step electrochemical process, Co is first deposited onto a Au STM tip, then completely dissolved and locally deposited onto the substrate underneath the STM tip. The method is shown schematically in Fig. 2.16. When Co is dissolved from the tip, there is local Co^{2+} oversaturation, which results in a laterally varying increase of the Co/Co^{2+} Nernst potential at the substrate surface. This method could be used to produce clusters with lateral diameters even below 20 nm and has also been used to grow Pb on $n-$Si(111):H [59]. Schindler et al. [57] have shown that there are basically five parameters which can be adjusted independently to control the cluster size - (1) tip to substrate gap, (2) cathodic charge predeposited onto the tip during "loading", (3) maximum metal ion current density during dissolution of metal from tip, (4) substrate potential and (5) diameter of the STM tip apex.

Widmer and Siegenthaler [60] have used an ESTM tip to deposit Pb on Ag(111) electrodes covered with a Pb UPD layer. In their method an anodic voltage pulse of $20-200\mu s$ is applied to the tip leading to a deposition on the surface. In difference to the method of Schindler et al. [57] mentioned above, their method does not involve a previous bulk metal deposition step at the tip followed by a localized dissolution. Therefore they supposed that the tip is covered with a Pb UPD layer that is most likely desorbed and redeposited locally on the substrate during anodic pulse modulation. The observation that nanoclusters formed by pulses of $+1$ V disappeared in the underpotential range, where 3d Pb deposits are dissolved and where the Pb adsorbate is thermodynamically stable, strongly indicates that clusters were Pb. In
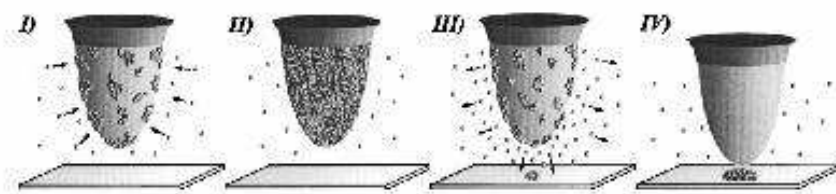
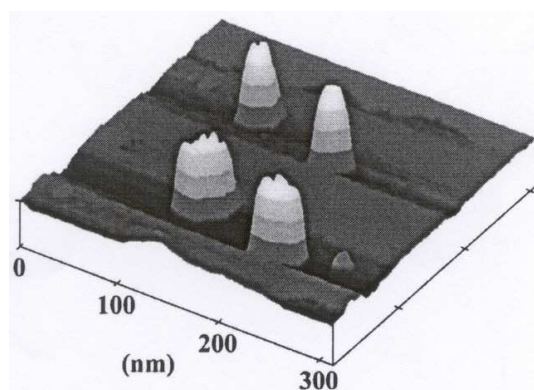Figure 2.16: Schematic diagram for cluster formation by dissolution from tip. From reference [57]

Figure 2.17: STM images of Co grown on Au(111) by the method of "dissolution from tip". Structures are about 3 nm high. The difference in size is due to different tip-substrate gap during dissolution process : upper row - 15 nm, lower row - 10 nm. From reference Schindler et al. [57].

Figure 2.18: Nearly 500 individual holes written by using voltage pulses applied to an STM tip to record this on HOPG. The letters are about 300Åtall. From reference [25].

contrast most clusters deposited with +2 V remained stable even in the underpotential range, suggesting that they are at least partially composed of Pt and/or Ir from the PtIr tips.

Defect based methods

The earliest nanostructuring methods by electrochemistry involved involved the generation of surface defects by the tip mechanically, i.e. by tip crash, or by high voltage pulses between tip and substrate. The defects thus created then acted as nucleation centres for metal deposition.

Creation of holes on HOPG with an STM tip in different environments was first studied by Albrecht et al. [25] [26]. Application of a voltage pulse of $1-100\mu$s with $3-8$ V amplitudes while tip is in tunneling range leads to formation of holes in HOPG. The presence of water was found to be essential to the process. Structuring occurs over a threshold value of ±4 V, it is polarity independant. At the threshold voltage domes are formed which are considered intermediaries in the hole formation. Due to the polarity independance, an electrochemical mechanism was considered unlikely. In contrast McCarley et al. [61] reported that hole formation in HOPG with an STM tip in air occured only when the substrate is biased positive (bias voltages $1.5-3.0$ V, $I_T = 2$ nA, pulse duration ~ 0.5 s). They found that negative pulses tended to deposit material onto HOPG, presumably from oxidation and removal of material from tip.

Another example of hole formation was demonstrated by Lebreton and Wang [62]. They created holes on Au(111) surface by applying voltage pulses (< 3 V, 100 ms, sample positive) across the tunneling gap in the presence of water or ethanol vapor. From the presence of water (or more precisely -OH group) and the polarity of the pulse the authors concluded that surface modification may be electrochemical in origin [63]. Upon application of pulse, water molecules form a hydroxide layer, followed with the formation of an oxide layer. From this point on place exchange mechanism can occur: there is insertion of oxygen atoms under the gold atoms. Then the gold atoms are removed from the surface.
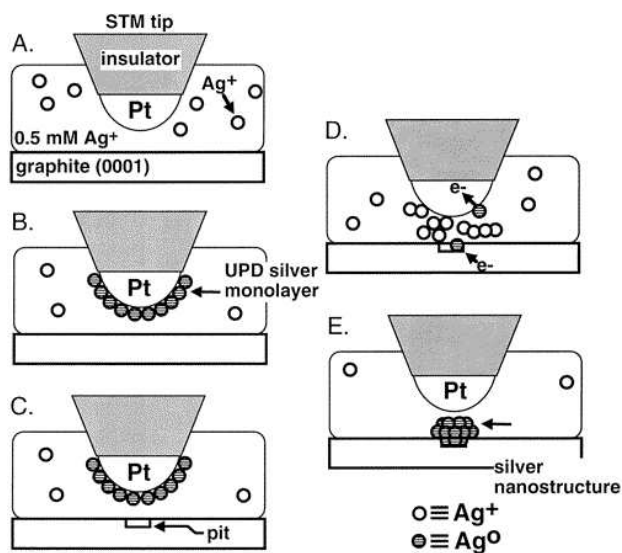
Figure 2.19: Schematic diagram illustrating the prominent features of the proposed mechanism for STM tip-directed silver nanostructure deposition on graphite. From reference [8]
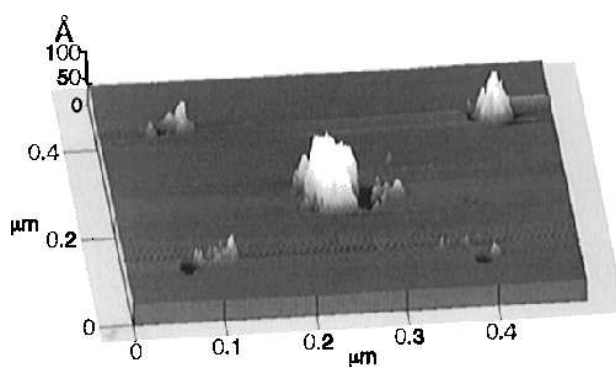

Figure 2.20: In situ STM image of five silver nanostructures deposited in rapid succession using the method described in the text. The structure in the center was the first deposited, and subsequent depositions proceeded in a counterclockwise direction starting from the upper right. From reference [8]

Li et al. [7] [8] used STM to create Ag nanoscopic structures from aqueous silver solution onto graphite basal plane. They proposed that metal deposition occurs via a two-step mechanism following the application of a negative voltage pulse to the graphite surface. In the first 5μs after application of the bias pulse having an amplitude greater than +4 V (tip positive), shallow, circular pit is formed in the graphite surface. Deposition of metal begins to occur at ~ 10 μs and the volume of the silver nanostructure saturates at $30 - 50\mu$s. The resulting nanostructures are disks with 20-40 nm diameter and 2-5 nm height. From their data and computer simulations, they concluded that the metal for the deposition is initially present as a UPD monolayer on the surface of Pt STM tip. After application of a bias pulse this adsorbed silver is oxidatively desorbed and silver ions migrate across the tip-sample gap and are deposited in the shallow nucleation site in the graphite surface.

Solomun and Kautek [64] also used defects to grow nanometer sized clusters. They used short voltage pulses (80 ns, -2.8 V) on an STM tip to create zero dimensional cavities, 5-10 nm diameter and 3-4 atomic layers deep, in Au(111) in a nitrate electrolyte. In the system Au(111)/BiO$^+$, NO$_3^-$, they obtained localized electrochemical underpotential deposition of 0-d bismuth dots. In contrast they also found that in the system Au(111)/Ag$^+$, NO$_3^-$, the nano holes are filled only at equilibrium potential and at overpotentials when the filling is flat to the surface parallel to a layer by layer growth of Ag on Au(111) terraces. This difference was explained by the difference in atomic radii of Bi and Ag, with Bi having a radius larger than Au while Ag has a radius close to Au.

Another approach similar to defect based methods involves the local removal of an overlayer exposing a small region where metal deposition can take place. The electrode potential can be maintained slightly negative of the Nernst potential so that no deposition takes place on the overlayer. Removing the overlayer by STM or AFM tip will then cause a deposition locally immediately. This was shown in an AFM study for Cu deposition onto Cu(100) and Cu(111) surfaces by LaGraff and Gewirth [65]. They suggest that at the pH potential region used in their study, bulk oxide formation on Cu is thermodynamically stable but there exist some oxide or hydroxide adlayers on the surface inhibiting the normal growth of Cu.

Ultra-short voltage pulses

Another interesting method to localize an electrochemical reaction near an STM tip or any tool electrode is by using ultra-short voltage pulses. Schuster et al. [9] showed that by applying pulses of width ≤ 100 ns and amplitude ± 4 V to a STM tip while imaging a Au(111) surface in concentrated electrolyte nanometer sized structures could be formed – holes by anodic dissolution or deposition of Cu islands (in Cu^{2+} containing electrolyte). They ruled out a chemically assisted field desorbtion process to explain this phenomenon and instead suggested an electrochemical basis. To explain ~ 10 nm sized structures by relatively blunt tips (tip radius ~ 500 nm), they proposed that at tip to sample gaps of a few nanometers, the buildup of the double layer instantaneously depletes the electrolyte from ions, increasing electrolyte resistance and suppressing electrochemical current. Only after ~ 100 ns, the ions from the bulk diffuse into the gap. However at the tip apex, with a gap of ~ 1 nm, the concept of two double layers breaks down and electrolyte resistance is meaningless. Ions created electrochemically at the tip apex are instantaneously transported by the electric field
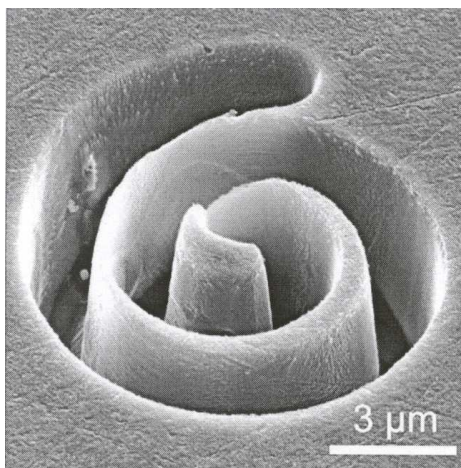
Figure 2.21: Spiral trough with a depth of 5 μm, machined into Ni with W tool using 3 ns, 2V pulses in 0.2 M HCl. From reference [66].

to the sample surface and vice versa.

This idea has been utilised for machining complex patterns including three-dimensional structures, lines, curved features, high aspect ratio features and arrays with nanometric or sub-μmetric precision [67, 68, 69, 66, 70]. For larger structures, a train of nanosecond pulses are applied to the tip while keeping it in vicinity of the substrate. The relationship between feature resolution and pulse width was found to be linear and although resolution increased at lower electrolyte concentrations there is a lower limit to the concentration that can be used [69]. Fig. 2.21 shows some examples of the kind of structures that have been machined with this method. A computational model has also been developed to simulate machining by ultra-short voltage pulses [71]. The model integrates (a) circuit model to describe charging discharging of double layers and electric field variation in electrolyte using a resistor capacitor network and (b) level set method to simulate feature profile evolution during machining.

Double layer cross-talk

For an STM operating at $I_T = 2$ nA and $U_T = 50$ mV, and assuming a tunnel barrier at the metal solution interface of $\phi_T = 1.5$ eV, the tip-sample gap is around 0.6 nm [55]. For a highly concentrated electrolyte (1 M) the double layer extends to about 0.3 nm from the substrate surface. This means that the double layers of the tip and substrate start to interfere. One important consequence is that the potential drop across the 'outer Helmholtz plane' of the substrate, just below the tip apex is different from that further away. That is to say there can be loss of potentiostatic control for the sample area below the tip. From the point of view of nanostructuring, this offers the opportunity to create reactions locally. Xie and Kolb [4] demonstrated that copper can be dissolved locally by applying a tip potential positive of the Cu/Cu^{2+} reversible potential E_0, despite the fact that the sample potential is held clearly negative of E_0. To explain this phenomenon, Xie and Kolb [4] considered the possibility of a change in Cu^{2+} concentration in the gap below tip and sample which could

lead to a shift in the Nernst potential. But they finally proposed that there is direct electron transfer (tunneling) from Cu/Cu^{2+} redox system to the tip which provides empty electron states. Depending on the potentials of tip and sample, they also showed that there are three regimes – (a) tip-enhanced copper deposition, (b) mere surface imaging and (c) tip-induced copper dissolution.

In similar vein Garcia et al. [5] showed that at STM-tip potentials more positive than the Ag/Ag^+ equilibrium potential, a local dissolution of the Ag(111) substrate in $HClO_4$ or H_2SO_4 is possible even at cathodic substrate overpotentials. They explain it by a reduced Ag^+ concentration under the STM tip promoted by both an electrostatic repulsion of Ag^+ and a reduction of mass transport due to the shielding effect of the tip.

Other methods

Pötzschke et al. [72] investigated localized deposition of Pb on n-Si(111) with an ESTM. According to their work, a local change of the band structure and the charge carrier density at the semiconductor surface can be obtained by local electrostatic interactions, for example, by a polarized STM tip. For n-doped Si, there are two stable regimes for tunneling – (1) when Fermi level of tip is adjusted within the semiconductor band gap and electrons from the conduction band tunnel to the unoccupied levels of the tip and (2) for a small potential window when the tip is more positive than the *flatband potential* although tunneling is reduced in this regime. The STM tip can be used to shift the band structure of the semiconductor locally towards a *depletion zone* - when the concentration of positive ions on the surface is enhanced - and the Nernst potential M/M^+ shifts towards more positive values leading to the deposition of M. In their work Pötzschke et al. [72] used different polarization regimes to deposit Pb under the STM tip - (a) a long pulse to fill the tunelling gap with Pb^{2+} ions and then a short pulse to modify the Si band gap leading to a deposition; (b) a long pulse to fill the gap, followed by a cathodic pulse on the tip to predeposit Pb on tip followed by an anodic pulse to deposit Pb on sample.

Berenz et al. [73] have induced nanostructuring on clean and ethene covered Pt(111) in a solution containing Cu^{2+} ions. Their method is to scan a small area with the tip very close to the surface while keeping both tip and substrate potentials in the UPD regime. In the case of ethene adsorbed surface, they observed the displacement of the adsorbate followed by Cu-UPD. Scanning under similar conditions over the surface free of organic adsorbate, but covered by UPD-Cu also leads to nanostructuring. They interpreted their results by a local tip-induced alloy formation. This approach was extended to other systems - Pt(100)/Cu, Pt(111)/As, Au(111)/Cu and Au(111)/Pd [74]. Since their method does not work with W tips as opposed to PtIr, UPD adlayer on the tip seems to play a role in nanostructuring.
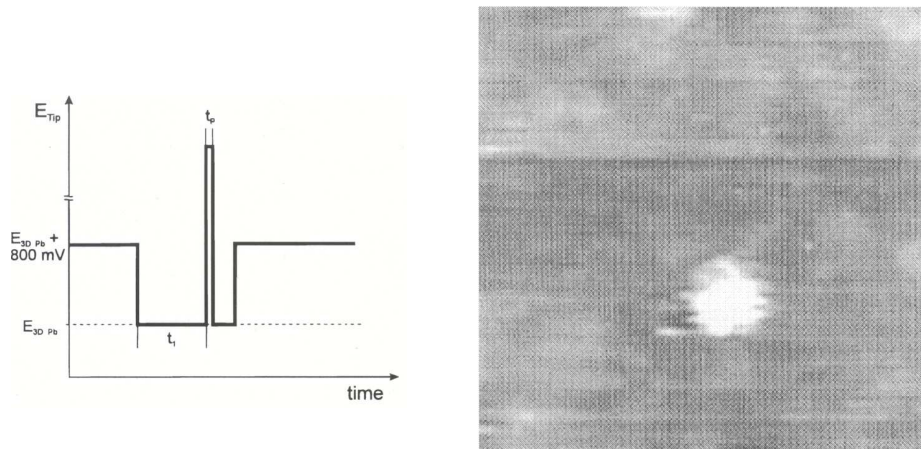
Figure 2.22: (left) The pulse polarization routine used to create cluster of Pb on n-Si(111) shown at right. (right) STM image 30 nm × 30 nm. Pulse parameters :5 V, 100 μs. From reference [72]

2.5 Nanoparticles – General characteristics

Nanoparticles are characterized by zero dimensionality and a size intermediate between atoms and macroscopic particles exhibiting bulk material properties. Due to their size nanoparticles exhibit properties different from the bulk material. The sources of this difference are (a) large fraction of surface atoms, (b) high surface energy, (c) spatial confinement and (d) reduced imperfections. Properties like melting point, mechanical strength, optical, magnetic properties or electrical conductivity can be very different for nanoparticles compared to the bulk material. Following are some examples which show the properties of nanoparticles.

Melting point of a metal or semiconductor reduces with decrease in particle size below 100nm. This can be seen for the case of gold nanoparticles in Fig. 2.23.The melting point decreases rapidly for particles below 5nm [75]. Similar observations have been made in the case of lead [76] and other metals. The lowering of melting point is due to increased influence of surface atoms as the ratio of surface to bulk atoms increases.

The electronic structure of a material is also modified with the size of the particle. When the size of the particle is smaller than a critical value, the electron's de Broglie wavelength, "quantum size effect" becomes important. This effect leads to spatial confinement of electrons and holes, formation of electric dipoles and formation of discrete energy levels in the material. Consequently electric properties of nanosized objects can be very different from their bulk counterpart. As an interesting example, it was shown that bismuth nanowires of 50 nm width have semiconductor properties rather than being metallic [77]. Quantum size effect influences both electric and optical properties [78].

Another property that is modified quite dramatically with decrease in particle size is the catalytic property of several metals. For instance in bulk form gold is known to be chemically inert to chemisorbtion and consequently a weak catalyst, but gold nanoparticles exhibit surprisingly high catalytic activity for a large range of chemical reactions [79, 80]. Similar to
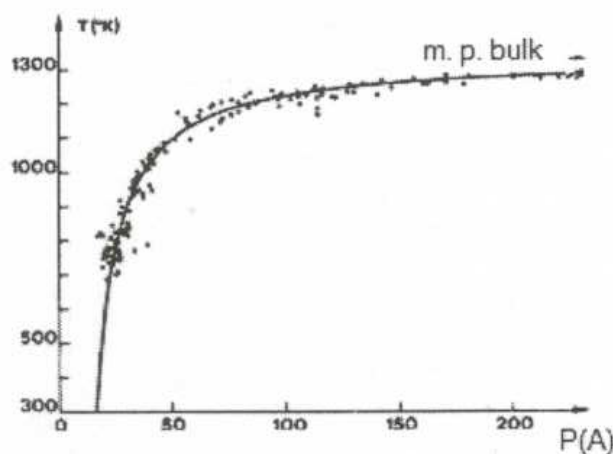
Figure 2.23: Melting point of gold as a function of their diameter. The plots include experimental data (individual points) and the results of a least-squares fit (solid line) [75].

gold, Pt nanoparticles also show extraordinary catalytic properties. Pt nanoparticles have for instance been used in the catalysis of oxygen electroreduction [81, 82] or in the oxidative dehydrogenation of ethanol [83]. In several cases a correlation between catalytic activity and particle size has been established; e.g. in the case of electrooxidation of methanol, the specific activity of particles was found to decrease with decreasing particle size in the range from 4.5 to 1.2 nm [84]. In the area of catalysis, now a days, nanoscience has become quite important.

In addition to the properties discussed above, other properties such as ferromagnetism and mechanical properties will also be affected. Recent years have seen enormous interests in the study, both fundamental and applied, of nanoparticles. For more details the reader may consult some reviews or books [85, 86].

2.6   Synthesis of Nanoparticles

Many methods have been developed to synthesize nanoparticles. Top-down methods include milling, lithography and repeated quenching. These methods suffer from the problem that there is not good control on the particle size and structure. Bottom-up approach is considered far more reliable. It includes homogeneous nucleation from liquid or gas phase, heterogeneous nucleation on a substrate, phase separation through annealing of certain solids or micelle synthesis. The bottom-up approach is classified broadly into two categories: thermodynamic equilibrium approach and kinetic approach [85]. The thermodynamic approach consists of the following steps:(i) generation of supersaturation, (ii) nucleation and (iii) subsequent growth. In the kinetic approach, the nanoparticles are grown by either limiting the amount of precursors available or by limiting the space available for growth. For practical use apart from the small size of particles other characteristics are also important: (i) identical size, (ii) identical shape or morphology, (iii) identical chemical composition and (iv) individually dispersed i.e. no agglomeration. This section gives, very briefly, an overview of
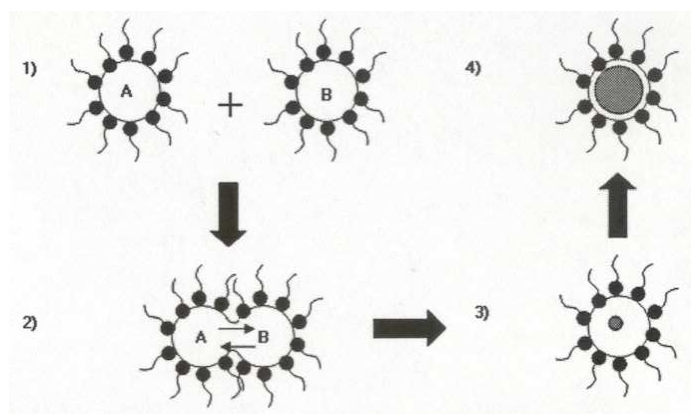
Figure 2.24: General scheme of synthesis of nanoparticles by mixing of two microemeulsions. Steps of the process: 1) micing of microemulsions, 2) collision, exchange and reaction, 3) nucleation and 4) growth of particles. A=metal precursor, B=reducing agent.

the two basic methods mentioned above.

Nanoparticles through homogeneous nucleation

The fundamentals of nucleation and growth are given in Appendix A. Synthesis of nanoparticles by homogeneous nucleation in liquid or gas or even by heterogeneous nucleation on a substrate follow the same principles. The key points are (i) the generation of supersaturation of growth species by changing a parameter e.g. temperature, (ii) the existence of a critical nucleus size r^* which is a function of the *supersaturation* and (iii) subsequent growth controlled by one of several growth modes.

One common method to generate supersaturation is through *in situ* chemical reactions by converting highly soluble chemicals into less soluble chemicals. In fact reduction of metal complexes in solutions is the most widely used method in the synthesis of metal colloidal dispersions. An example is the formation of colloidal gold by sodium citrate reduction of chloroauric acid at 100℃ reported by Turkevich et al. [87]. In their "standard" experiment, 95 ml of chlorauric acid solution (containing 5 mg Au) is boiled and 5 ml 1% sodium citrate is added with good mechanical stirring. The mixture is kept at 100℃ till colour changes. This method is highly reproducible and gives uniform particle size of ∼ 20 nm in diameter. Henglein et al. [88] studied three different methods for the preparation of Pt nanoparticles: radiolytic reduction (in presence of radiation), hydrogen reduction and citrate reduction.

Synthesis inside micelles or using microemulsions

In this method chemical reaction is limited to inside nanosized containers or micelles and particle growth stops when the reactants are consumed. Most commonly microemulsions are used for synthesis of nanoparticles. A microemulsion is a stable dispersion of two immiscible liquids e.g. an organic solvent in an aqueous solution. The dispersed droplets are less than

100 nanometers in diameter. Such a microemulsion system can be used for the synthesis of nanoparticles of metals, metaloxides, metal alloys or polymers and is specially suitable for producing particles with very narrow size distributions [89]. The common scheme for synthesis using microemulsions is shown in Fig. 2.24. The nanodroplets in the aqueous solution exhibit brownian motion, thus colliding continuously with each other. Dimers and higher aggregates are continuously formed and disintegrated. As a result of this the contents of the droplets are distributed over the entire droplet population and synthesis of nanoparticles occurs via reaction, nucleation and growth inside the droplets. The droplet size also controls the size of the particle. An example is the formation of CdSe nanoparticles using organometallic reagents by Steigerwald et al. [90].

2.7   Conclusions

Since its invention in 1981, the STM has made many important contributions not only in the area of surface science but also in diverse fields as electrochemistry, life sciences, materials, nanotechnology etc and its limits are continuously being expanded. In the area of nanostructuring, STMs offer the opportunity to manipulate the surface at the smallest scale i.e. atom by atom – Eigler's quantum corral is probably the best known example.

STMs were applied to electrochemistry shortly after their invention by coating STM tips with an insulating layer nearly to the end and by adding potentiostatic control. In electrochemistry, STMs have made large contributions in understanding surface dynamics, surface reconstruction, adlayer structures, oxide growth, metal deposition etc.

A variety of methods have been developed in the last decade to use an STM in electrolyte for nanostructuring. The tip offers a way to control the fields, double layers or charge distributions in the tunneling gap, making it possible to use it as a tool for creating local structures. To summarize the methods being used for nanostructuring with an ESTM – (a) tip-induced : transfer of material to tip and redeposition on surface, (b) defect-induced : preferential growth on defects created by the tip, (c) ultra-short voltage pulses : localize electrochemical reaction near tip end, (d) double-layer crosstalk : modification of the double layer structure in the tunneling gap and (e) others and combinations of the methods listed. It would not be incorrect to say that many more methods and systems will be investigated in future. It may however be noted that while for some of the methods, the phenomena is fairly well understood, but for many, further investigations - experimental and modelling - are needed to elucidate the subject.

A brief overview was provided on nanoparticles and methods to synthesize them. New properties exhibited by nanoparticles are now being increasingly used for a broad range of applications. Nanoparticles have or are envisaged to have applications in catalysis, photo-electronic materials, biochemicals, drug delivery etc.

In the domain of nanostructuring and nanoparticles, this thesis aims to develop novel methods to create nanosized particles by using Electrolytical STM or similar techniques. For the ESTM, since little has been done on the modelling front, the thesis will try to develop comprehensive models to explain important nanostructuring methods.

Chapter 3

Structuring by ESTM tip – Mathematical modelling

The local surface modifications by an ESTM tip result from the electrical field and charge distribution near the tip end. This chapter describes the models developed during the course of this work to estimate field and charge distributions in the tip sample gap region. In the first section the field is calculated in absence of ions i.e. in dielectric medium. The second section looks at the equilibrium field and charge distribution in an electrolyte. Here Poisson Boltzmann equation is used which combines the Poisson equation for electrostatic field with Boltzmann distribution. The third section looks at the dynamics – time evolution of fields and charge densities. Since this is difficult to model, only the very initial phase, corresponding to ultra-short voltage pulses, is calculated. Local deposition of metal under the ESTM tip can occur following different physical processes. This is elaborated in the next section for two types of systems – deposition from diffusing species and deposition from surface adsorbed species. Estimates are made of the total number of metal atoms formed on the surface and how this affects the formation of stable deposits.

3.1 Electrostatic field in dielectric
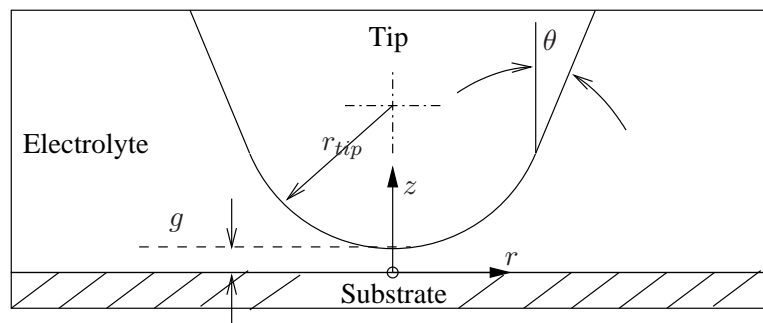
Figure 3.1: Tip sample geometry in the STM

For the geometry shown in Fig. 3.1, the electrostatic potential φ is calculated with the Laplace equation

$$\nabla^2 \varphi = 0 \tag{3.1}$$

with the boundary conditions $\varphi = \varphi_{tip}$ on the tip, $\varphi = \varphi_{sample}$ on the sample ($V = \varphi_{tip} - \varphi_{sample}$) and appropriate boundary conditions on the outside boundary. Two kinds of outer boundaries were considered – cylindrical or spherical. For the case when the tip to sample gap is small, and the boundary is far away, the results near the tip apex are unaffected by the type of boundary chosen. Choosing the outside boundary sufficiently far away and assuming Neumann boundary condition, $\frac{\partial \varphi}{\partial \hat{n}} = 0$, gives consistent solution at the tip apex. The equation is solved in cylindrical coordinate system in Matlab pdetool toolbox. Assuming radial symmetry, the Laplace equation becomes

$$\frac{\partial^2 \varphi}{\partial r^2} + \frac{1}{r} \frac{\partial \varphi}{\partial r} + \frac{\partial^2 \varphi}{\partial z^2} = 0 \tag{3.2}$$
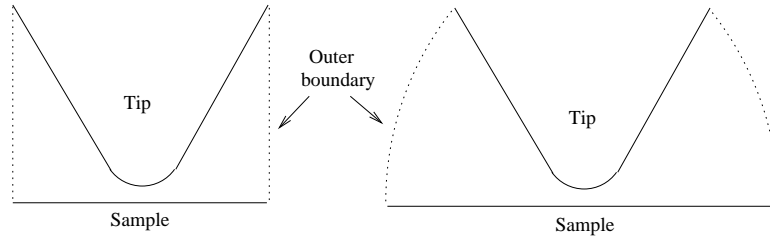
Figure 3.2: Outer boundaries considered for field calculation

Electric field can also be calculated by the method of image charges [91]. The tip is modelled as a sphere of radius r_tip. An infinite series of point charges are present as shown.

$$
\begin{aligned}
q_1 &= 4\pi\epsilon_0\epsilon_r\varphi_{tip} \times r_{tip} \\
z_1 &= r_{tip} + g \\
q_i &= q_{i-1} \times \frac{r_{tip}}{r_{tip} + g + z_{i-1}} \\
z_i &= r_{tip} + g - \frac{r_{tip}^2}{r_{tip} + g + z_{i-1}}
\end{aligned}
\tag{3.3}
$$

The sets $\{q_i, -q_i\}$ ensure that the potential on the sample surface is fixed and the sets $\{-q_i, q_{i+1}\}$ ensure that potential on the tip surface is fixed. Infinte series ensures both. It can be shown that z_i converges to $\sqrt{(r_{tip} + g)^2 - r_{tip}^2}$ and that q_i converges to zero.

If the tip to sample gap is much smaller than the tip diameter, $g \ll d_{tip}$, as is usually the case in an STM, and the tip angle, $\theta \to 0$ then on the sample surface, the field (only the component normal to the surface is non-zero) can be approximated well by the following :

$$E_\perp(r) = \frac{V/g}{1 + (\frac{r}{\sqrt{d_{tip}g}})^2} \tag{3.4}$$
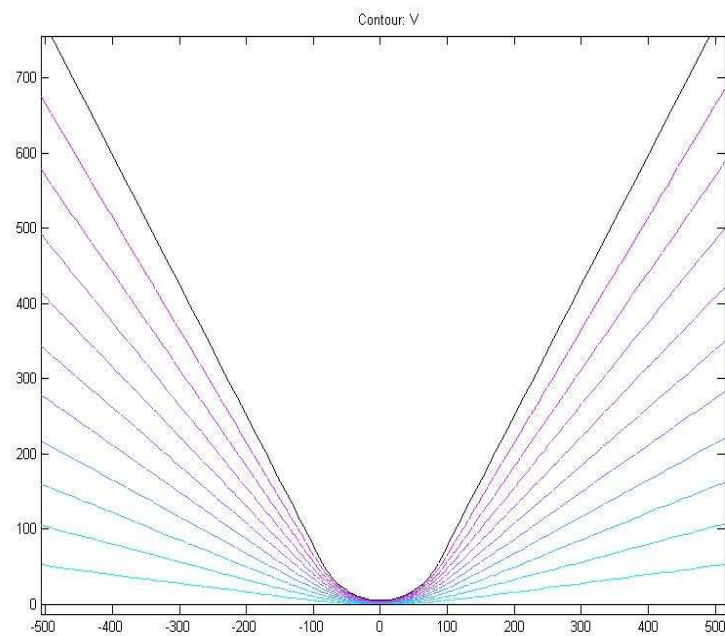
Figure 3.3: Equipotential lines for the tip sample geometry shown, calculated in Matlab pdetoolbox. (The scale is in nanometer.)
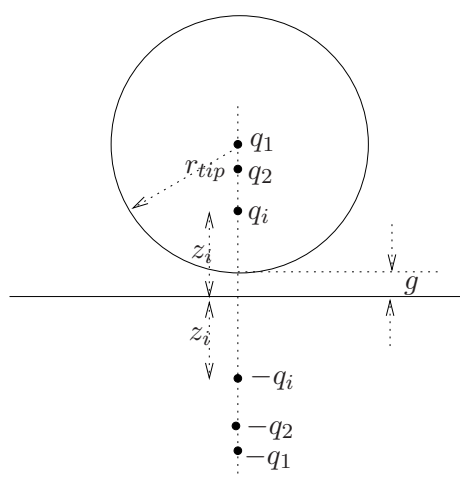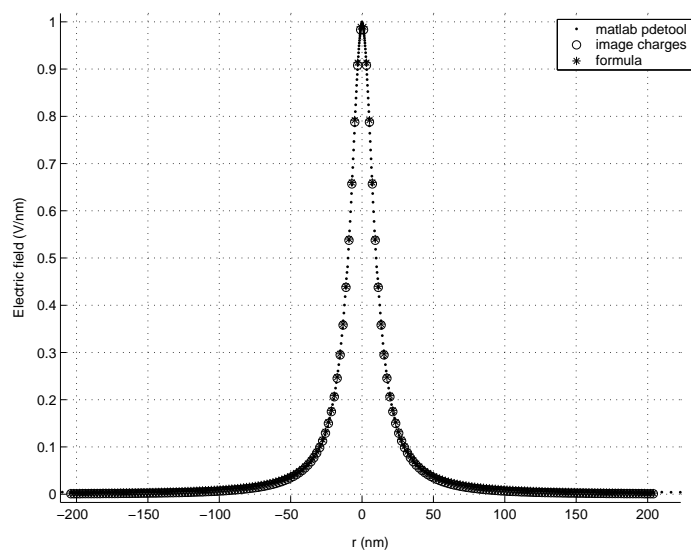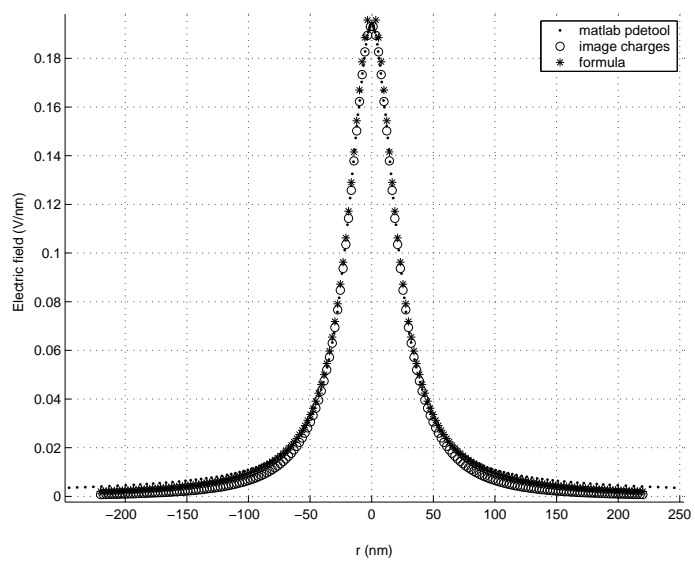

Figure 3.4: Method of image charges for estimating the field at the sample surface.

(a) $r_{tip} = 50$ nm, $g = 1$ nm and tip angle $\theta = 30°$

(b) $r_{tip} = 50$ nm, $g = 5$ nm and tip angle $\theta = 30°$

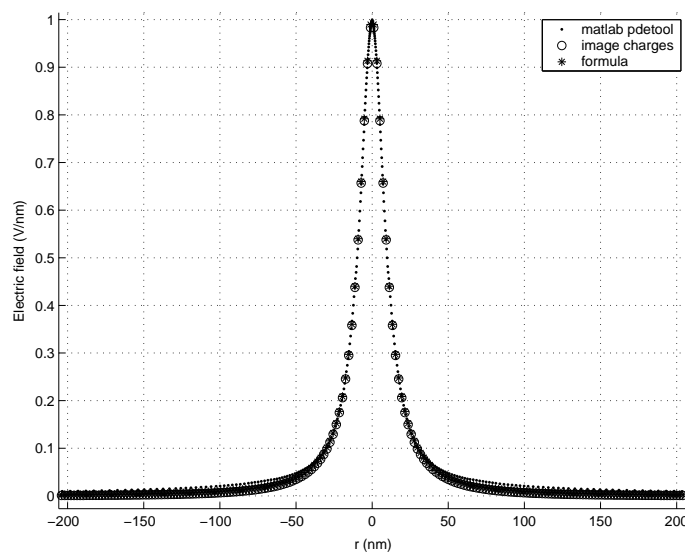(c) $r_{tip} = 50$ nm, $g = 1$ nm and tip angle $\theta = 60°$

Figure 3.5: Electrical field calculated by different methods.

For the tip-electrolyte-sample system, electrostatic field as calculated in this section, gives the *primary current distribution*. Primary current distribution depends only on the geometry of the system and neglects surface overpotentials. On the sample side, any process that depends on the field, is going to be restricted to a zone around $r = 0$. Based on Eq. (3.4), this zone can be considered to have a diameter $2\sqrt{d_{tip}g}$ (*full width at half maximum*). As an example, for a tip of diameter 100 nm and tip-sample gap of 1 nm, the zone of influence is $2\sqrt{100 \times 1} = 20$ nm.

3.2 Field in electrolyte – thermodynamic limit

When the electrolyte resistance is much smaller than the electrode charge-transfer resistance, (that is, a slow reaction), the current (now called *secondary current distribution*) is mostly influenced by the activation overpotential.

Helmholtz model

At an electrode-electrolyte interface, mobile ions from the solution collect to form the *double layer*. The simplest model of the structure of the metal-solution interphase is the Helmholtz compact double layer model [92]. According to this model, all the excess charges on the solution side are lined up in the same plane at a fixed distance away from the electrode. This plane is called the Helmholtz plane and the fixed distance, x_H is determined by the hydration sphere of the ions. It is defined as the plane of centers of the hydrated ions. All excess charge on the metal is located at the metal surface. Thus, this model is equivalent to

a parallel plate capacitor with

$$c = \frac{\epsilon_o \epsilon_r}{4\pi x_H} \tag{3.5}$$

where c is the capacitance per unit area, ϵ_r is the relative dielectric constant of the solution (water).

Gouy-Chapman model and improvements

Gouy [93] and Chapman [94] independantly proposed a new model that allowed for a statistical, potential dependant distribution of ions in the solution side. They assumed that this distribution obeys Boltzmann distribution law and ions can be modelled as point charges. The result is the presence of a diffuse layer extending into the solution. Stern [95] improved on this model by stating that the charges on the solution side can only come as close to the interphase as x_H, or the plane of closest approach.

For the Gouy-Chapman model: if there are several ionic species in the solution, i^{th} species has electronic charge $q_i e$ (e being the charge of an electron), and bulk number concentration n_i^b, then the concentration at a position $\vec{r}$ is given by

$$n_i(\vec{r}) = n_i^b exp(\frac{-q_i e \varphi(\vec{r})}{k_B T}) \tag{3.6}$$

where $\varphi(\vec{r})$ is the potential at $\vec{r}$. Net charge, $\rho(\vec{r})$ and the electric potential $\varphi(\vec{r})$ are given by:

$$\rho = \sum_i q_i e n_i^b exp(\frac{-q_i e \varphi}{k_B T})$$
$$\nabla^2 \varphi = -\frac{\rho}{\epsilon_0 \epsilon_r} \tag{3.7}$$

For a solution containing two types of ions of equal and opposite charge $+q$ and $-q$, and if the metal is considered to be at φ_0 while bulk electrolyte at $\varphi = 0$, the solution to the equations (3.7) in 1d, yields:

$$\frac{\tanh{(qe\varphi(x)/4k_B T)}}{\tanh{(qe\varphi_0/4k_B T)}} = \exp{(-\kappa x)} \tag{3.8}$$

where κ is given by

$$\kappa = \left(\frac{2n^b q^2 e^2}{\epsilon_0 \epsilon_r k_B T}\right)^{1/2} \tag{3.9}$$

In the limit of small φ_0, $(qe\varphi_0/4k_B T < 0.5$ or $\varphi_0 < 50/q$ mV at 25℃$)$, $\tanh{(qe\varphi(x)/4k_B T)} \approx qe\varphi(x)/4k_B T$ everywhere and

$$\varphi = \varphi_0 \exp{(-\kappa x)} \tag{3.10}$$

The characteristic thickness of the diffuse layer d_{dl} can be taken as $1/\kappa$. For example, a concentration of 1 M gives $d_{dl} = 3$ Åwhich is close to the radius of the hydration sphere of an ion. On the other hand 0.01 M gives $d_{dl} = 30$ Å, extending considerably into the solution.

(a) Double layer model after Gouy, Chapman and Stern (b) Triple layer model including specifically adsorbed species
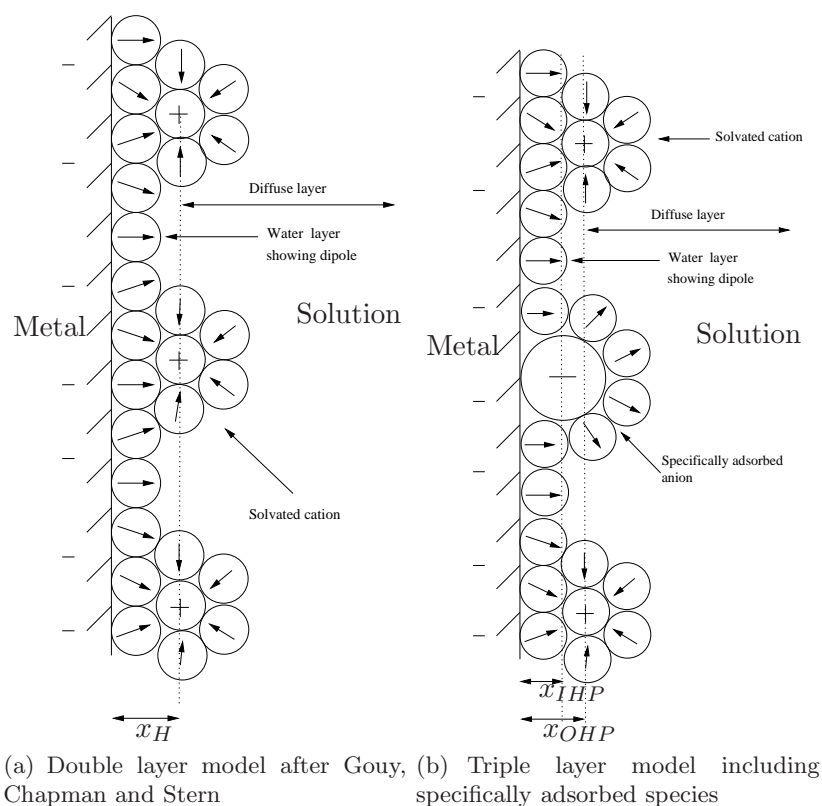
Figure 3.6: Double layer models. Adapted from reference [97].

The modification given by Stern [95], leads to a region just next to the metal surface upto x_H where the potential drop is linear and the Poisson Boltzmann equation is valid for distances greater than x_H. Grahame [96] further improved on this model by introducing the inner plane of closest approach, which is located at a distance x_{IHP} from the electrode. This is the plane of centers of partially or fully dehydrated, specifically adsorbed ions. The closest approach of the fully hydrated ions is at the distance x_{OHP}. The double layer pictures are shown in Fig. 3.6 and the potential profiles in the two models is schematically shown in Fig. 3.7.

Double layer effects on electrode reaction rates

The double layer structure and specific adsorbtion of ions can affect the kinetics of electrode reactions. This was first recognized and studied by Frumkin [99] and is sometimes called the *Frumkin effect*. For a species undergoing reaction without specific adsorbtion, the position of closest approach is x_{OHP}. The potential at x_{OHP} is not the same as that in the bulk electrolyte because of drop through the diffuse layer and possibly because some ions are specifically adsorbed. These potential differences in the double layer can affect the reaction kinetics in two ways.

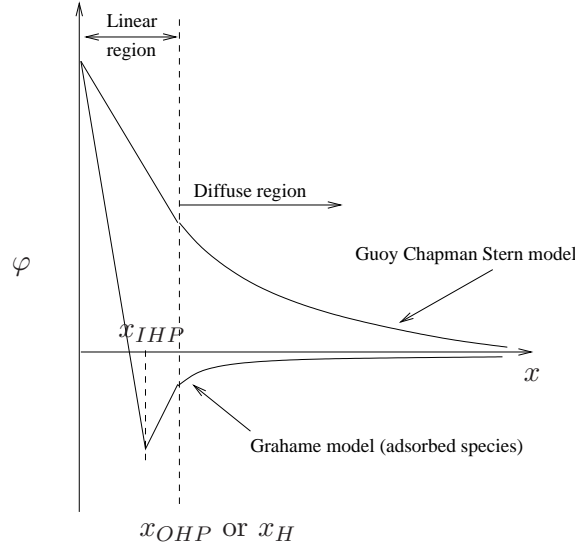(a) Concentration – The concentration of the reacting species at x_{OHP} is not the same

Figure 3.7: Schematic representation of the potential profile. The curve shown for the Grahame model is an extreme case. Adapted from reference [98].

as that in bulk.

$$n(x_{OHP}) = n^b exp(\frac{-qe\varphi(x_{OHP})}{k_B T}) \tag{3.11}$$

This means that when the electrode has a positive charge, anions will be attracted to the electrode surface while cations will be repelled. At *potential of zero charge* (PZC), $n(x_{OHP}) = n^b$.

(b) Driving potential – The potential difference driving the electrode reaction is not $\varphi^M - \varphi^S$, (φ^M is the potential at the metal electrode and φ^S is the potential in the solution), but $\varphi^M - \varphi(x_{OHP})$.

For a totally irreversible one-step, one-electron reaction, the rate equation is normally written as

$$\frac{j}{e} = k^0 n(0,t) \exp\left(\frac{-\alpha e(E - E^{0'})}{k_B T}\right) \tag{3.12}$$

where $E^{0'}$ is the formal electrode potential and E is the electrode potential and j is the current density. Applying the corrections in concentration and driving potential gives

$$\frac{j}{e} = k^0_t n^b \exp\left(-q\varphi(x_{OHP})\right) \exp\left(\frac{-\alpha e(E - \varphi(x_{OHP}) - E^{0'})}{k_B T}\right) \tag{3.13}$$

If $n^b \approx n(0,t)$, one obtains

$$k^0_t = k^0 \exp\left(\frac{-(\alpha - q)\varphi(x_{OHP})}{k_B T}\right) \tag{3.14}$$

This relationship allows the calculation of true rate constant k^0_t from the apparent one k^0. The above analysis shows that reaction kinetics is affected by the double layer. We shall

see later that for an ESTM, the geometry can introduce changes in the double layer locally, thereby changing reaction rate locally.

Application to ESTM

In an ESTM, the tip to sample distance may be so small that the double layers of the tip side and the substrate side interfere. Secondly the geometry no longer renders a 1d simplification. Therefore an exact calculation is possible only from the basic Poisson Boltzmann equation. Assuming the geometry shown in Fig. 3.1, rewriting the equation (3.7) in cylindrical coordinate system with radial symmetry gives

$$\rho = \sum_i q_i e n_i^b exp(\frac{-q_i e\varphi}{k_B T})$$
$$\frac{\partial^2 \varphi}{\partial r^2} + \frac{1}{r}\frac{\partial \varphi}{\partial r} + \frac{\partial^2 \varphi}{\partial z^2} = -\frac{\rho}{\epsilon_0 \epsilon_r} \tag{3.15}$$

Approximate solution near tip end

These equations do not yield analytical solutions. Nevertheless, in certain regimes it may be possible to find analytical solutions. Of particular interest is the solution between the tip apex and the sample surface. From the 1d solution of the Poisson Boltzmann equation, we know that the characteristic length scale is given by d_{dl}. At the tip apex, solution of the Eq. (3.15) will also show characteristic length scales: in $z - d_{dl}$ and in $r - r_{tip}$. If $d_{dl} \ll r_{tip}$, then

$$\frac{\partial^2 \varphi}{\partial r^2} + \frac{1}{r}\frac{\partial \varphi}{\partial r} \ll \frac{\partial^2 \varphi}{\partial z^2} \tag{3.16}$$

This can be understood in the following way. When $r_{tip} \gg d_{dl}$, it means that the tip end is rather flat. Hence the equipotential surfaces between tip apex and sample are parallel to the tip end and the sample surface. Then at $r = 0 \Rightarrow x = y = 0$

$$\frac{\partial^2 \varphi}{\partial r^2} + \frac{1}{r}\frac{\partial \varphi}{\partial r} = \frac{\partial^2 \varphi}{\partial x^2} + \frac{\partial^2 \varphi}{\partial y^2} = 0 \tag{3.17}$$

With these approximations, at $r = 0$, Eq. (3.15), simplifies to

$$\rho = \sum_i q_i e n_i^b exp(\frac{-q_i e\varphi}{k_B T})$$
$$\frac{d^2 \varphi}{dz^2} = -\frac{\rho}{\epsilon_0 \epsilon_r} \tag{3.18}$$

which is just the 1d equation with only one difference that now the two electrodes can be close to each other. The equation can be solved in a similar way as the 1d case. For a symmetrical electrolyte and with the approximation $(qe\varphi/k_B T)^2 \ll 1$ one gets

$$\rho = qen^b \left\{ \exp\left(\frac{-qe\varphi}{k_B T}\right) - \exp\left(\frac{+qe\varphi}{k_B T}\right) \right\} \approx \frac{2q^2 e^2 n^b}{k_B T}\varphi$$
$$\frac{d^2 \varphi}{dz^2} = -\frac{q^2 e^2 n^b}{k_B T}\frac{\varphi}{\epsilon_0 \epsilon_r} \tag{3.19}$$
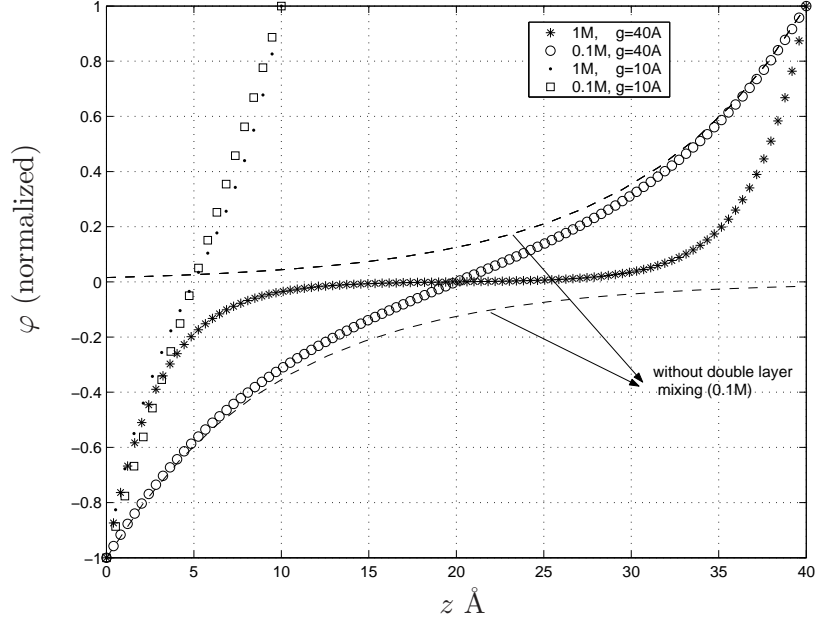
Figure 3.8: Potential profile between tip and sample at $r = 0$ from Eq. (3.22)

The solution is

$$\varphi(z) = A \exp(-\kappa z) + B \exp(+\kappa z) \qquad (3.20)$$

where κ is given by Eq. (3.9), A and B are determined by the boundary conditions

$$\varphi_{sample} = A + B$$
$$\varphi_{tip} = A \exp(-\kappa g) + B \exp(+\kappa g) \qquad (3.21)$$

which gives finally

$$\varphi(z) = \frac{\{-\varphi_{sample} \exp(-\kappa g) + \varphi_{tip}\} \exp(\kappa z) + \{\varphi_{sample} \exp(\kappa g) - \varphi_{tip}\} \exp(-\kappa z)}{\exp(\kappa g) - \exp(-\kappa g)} \qquad (3.22)$$

The solution is plotted for different cases in Fig. 3.8. The plot shows the difference due to concentration as well the tip sample gap. Not surprisingly the fields at tip and sample at $r = 0$ can be very different from those at $r \gg 0$. This can strongly influence the reaction rates.

General solution

More generally the solution is given by Eq. (3.15). An iterative method is used to solve this over a grid of equidistant points using the following equation

$$\frac{\partial \varphi}{\partial t} = \frac{\partial^2 \varphi}{\partial r^2} + \frac{1}{r} \frac{\partial \varphi}{\partial r} + \frac{\partial^2 \varphi}{\partial z^2} - \left(-\frac{\rho}{\epsilon_0 \epsilon_r}\right) \qquad (3.23)$$

(a) Nodes generated to solve Poisson Boltzmann equation (b) Pseudo point at boundary for our tip sample geometry
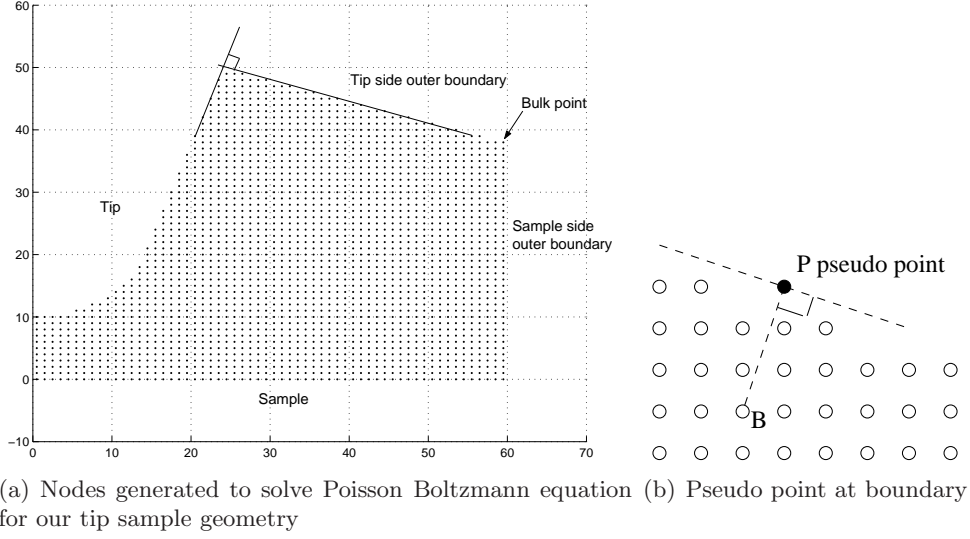
Figure 3.9: Rendering of the geometry for numerical simulation

An example of the grid generated is shown in Fig. 3.9(a). The boundary on the far side is built in two parts – (a) perpendicular to the sample surface and (b) perpendicular to the tip surface. Since the double layers far away from the tip apex ensure that equipotential lines are parallel to the electrode surfaces, these boundaries are a natural choice. The boundary condition used on these boundaries as well as on the inner boundary is the Neumann boundary condition $\frac{\partial \varphi}{\partial \hat{n}} = 0$. The intersection of the outer boundaries is considered to be a bulk point and the potential there is zero. Points that represent the tip and sample surfaces are at φ_{tip} and φ_{sample} respectively. Space derivatives are calculated using the approximation –

$$\frac{\partial f(x)}{\partial x} = \frac{f(x + \Delta x) - f(x - \Delta x)}{2\Delta x}$$
$$\frac{\partial^2 f(x)}{\partial x^2} = \frac{f(x + \Delta x) + f(x - \Delta x) - 2f(x)}{\Delta x^2} \tag{3.24}$$

Initial condition used is $\varphi = 0$ everywhere except at the tip and sample surfaces where it is given. φ is evolved in time (this is just a notional time) according to the Eq. (3.23). Under the given conditions, φ converges to a steady state, when it is the solution to the Eq. (3.15). For the outer boundary, pseudo points are used to calculate space derivatives. The way φ is found on a pseudo point is shown in Fig. 3.9(b). Since $\frac{\partial}{\partial \hat{n}} = 0$ the value of φ on a pseudo point, P, is taken to be the same as that of a point B, as shown. Since all the points fall on square grid, this enforces restrictions on the angles that can be used for the tip (see Fig. 3.1). More precisely $\tan \theta = \frac{n}{m}$ where n and m are integers. As can be seen practically any desired angle is possible.

A typical solution of φ is shown in Fig. 3.10(a). Simulation conditions – $r_{tip} = 45$ Å, $g = 30$ Å, $\theta = 18.4°$ ($\tan \theta = 1/3$), 1:1 electrolyte with $q = 1$ and concentration 0.1 M, $\varphi_{tip} = 0.1$ V and $\varphi_{sample} = -0.1$ V . A typical plot showing how the potential converges to a steady state value is seen in Fig. 3.10(b).
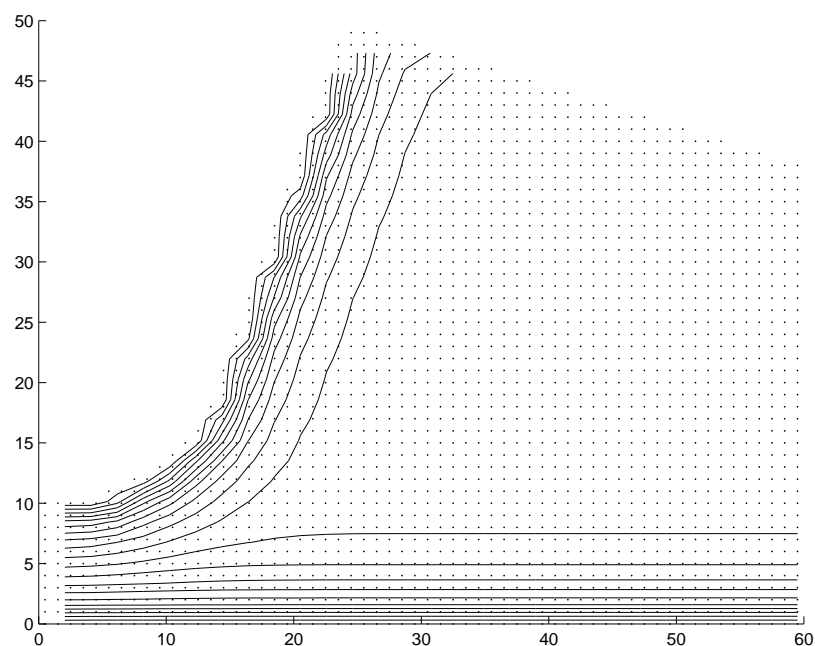
(a) Equipotential lines showing the steady state solution of Eq. (3.23). Simulation conditions – $r_{tip} = 45$ Å, $g = 30$ Å, $\theta = 18.4°$, 1:1 electrolyte with $q = 1$ and concentration 0.1 M, $\varphi_{tip} = 0.1$ V, $\varphi_{sample} = -0.1$ V
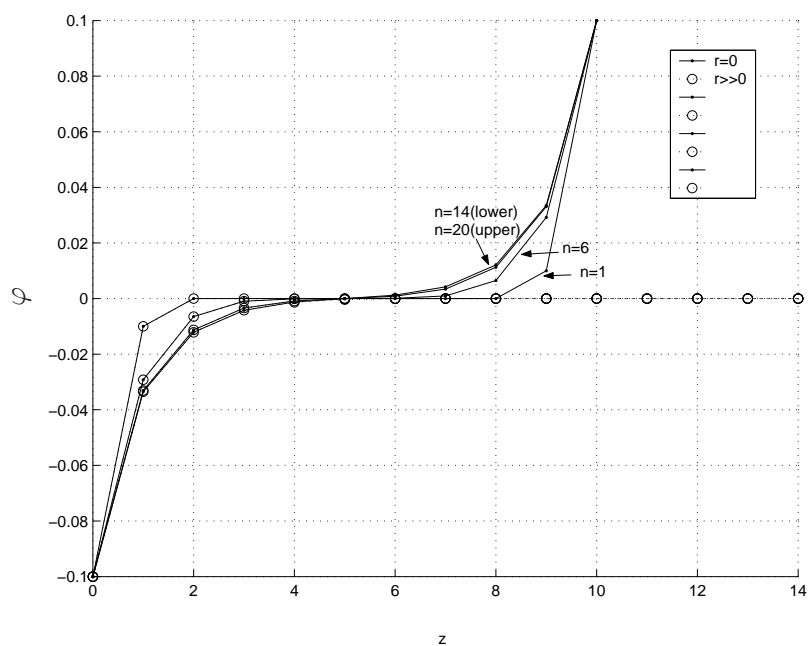
(b) Time evolution of the potential based on Eq. (3.23). For reasonalbly small Δt and for $e\varphi/k_B T$ not too large, the solutions converge.

Figure 3.10:

In the way it is simulated, the unit of length can be chosen arbitrarily while forcing the unit of concentration (or vice versa). This has an interesting consequence. Choosing an arbitrarily small length scale gives the Gouy-Chapman model. However we can also choose to work in units of x_{OHP}. Then the solution would represent the Gouy-Chapman-Stern model with the understanding that from the electrode surface to x_{OHP} the potential drop is linear. Elsewhere interpolation from multiple neighbouring points can be used to get a more precise solution.

Influence of different parameters

From the *Frumkin effect* we know that reaction kinetics is influenced by the double layer by modification in concentration and driving potial. Further in the case of ESTM, double layers may mix, resulting in a further change of the double layer structure. To understand, it is instructive to look at the plots of $\varphi_{reaction} = \varphi^M - \varphi(x_{OHP})$ at the sample surface under different conditions. It is also remarked that the concentration at x_{OHP} follows the potential in a straight forward manner : $n(x_{OHP}) = n^b exp(\frac{-qe\varphi(x_{OHP})}{k_BT})$ or $n(x_{OHP}) = n^b exp(\frac{-qe(\varphi^M - \varphi_{reaction})}{k_BT})$.

Influence of concentration – At high concentrations e.g. 1M, the diffuse part of the double layer is very small. Consequently the double layers are very compact. For an ESTM, this means that the zone of double layer interference is very small and exists only when the tip to sample gap is very small. When there is larger interference, at e.g. 0.01 M, the potential drop in x_{OHP} on the sample surface at $r = 0$ is very different from $r \gg 0$. This difference could allow the localization of reactions to the zone just below the tip.

Influence of tip to sample gap – The gap between tip and sample naturally affects the interference of the double layers. The influence is shown for high concentration in Fig. 3.12 and for moderate concentration in Fig. 3.13.

Influence of tip radius – The zone of interference of the double layers is also determined by the tip radius. From the geometry of Fig. 3.1 and assuming $r_{tip} \gg g$ & $r_{tip} \gg d_{dl}$ one obtains $r_{int} = \sqrt{2r_{tip}(2d_{dl} - g)}$. This suggests a square root dependence on r_{tip}. However from the plots Fig. 3.14(a) and Fig. 3.14(b) one observes a more or less linear dependence of r_{int} on r_{tip} implying that double layers can not be considered just geometrically.

Influence of applied potential – The solution of the Poisson Boltzmann equation for high potentials gives more compact double layers as compared to the d_{dl} calculated from Eq. (3.9). For the ESTM this means that at higher potentials the double layer interference zone will be further restricted as seen in Fig. 3.15(a).

The results of Xie and Kolb [4] showing spatially confined copper dissolution by applying a tip potential positive of the Cu/Cu^{2+} reversible potential E_0, despite the fact that the sample potential is held clearly negative of E_0 and similar reults of Garcia et al. [5] for Ag/Ag^+ system have been explained by the double layer interference. For such systems
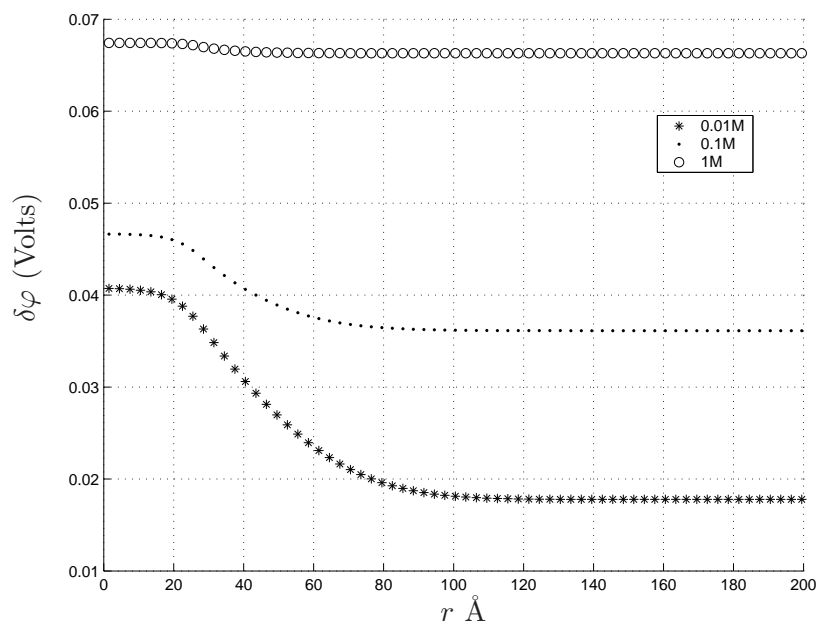
Figure 3.11: Influence of electrolyte concentration. Potential drop across x_{OHP} (taken as 3 Å) on the sample surface. Simulation conditions – $r_{tip} = 100$ Å, $g = 15$ Å, $\theta = 45°$, 1:1 electrolyte with $q = 1$, $\varphi_{tip} = 0.1$ V and $\varphi_{sample} = -0.1$ V

the shift in the Nernst potential at $r = 0$ is given by $\varphi(0, x_{OHP}) - \varphi(\infty, x_{OHP})$, towards negative side. Consequently the concentration of metal ions should increase just below the tip leading to dissolution from the substrate below the tip. In the the two cases mentioned, the tip was extremely close to the substrate ($I_T = 2\text{to}15$ nA), leading to more complications. The calculations in this section, suggest that by observing the effects of concentration and tip-sample gap, it should be possible to verify the exact mechanism.
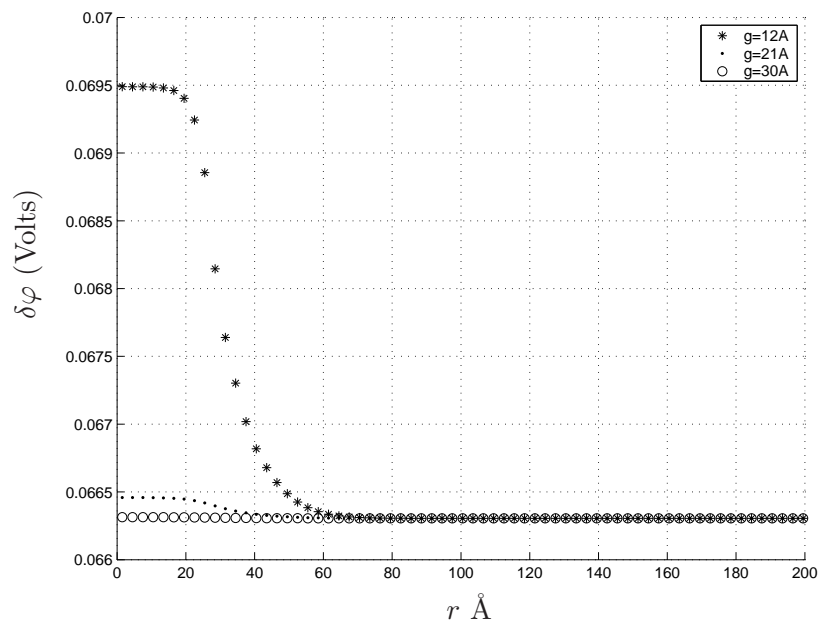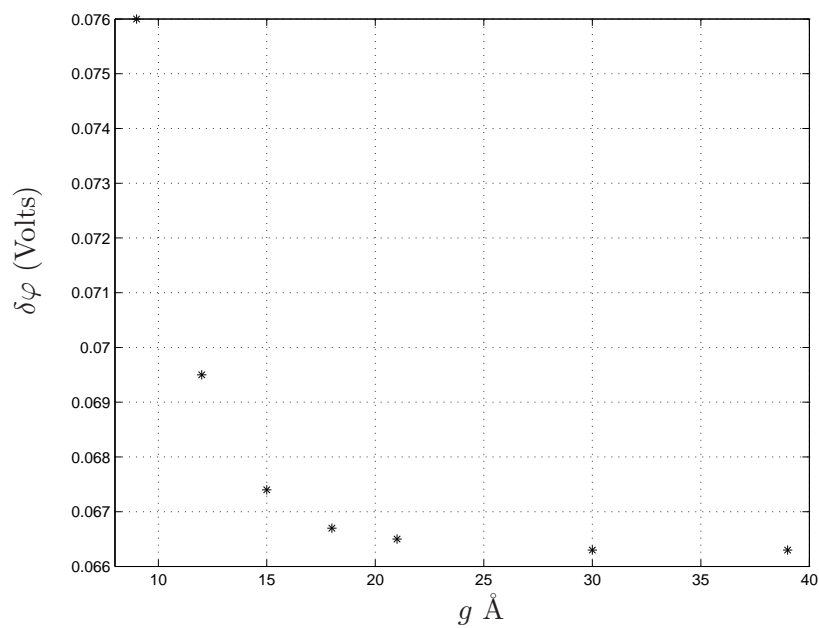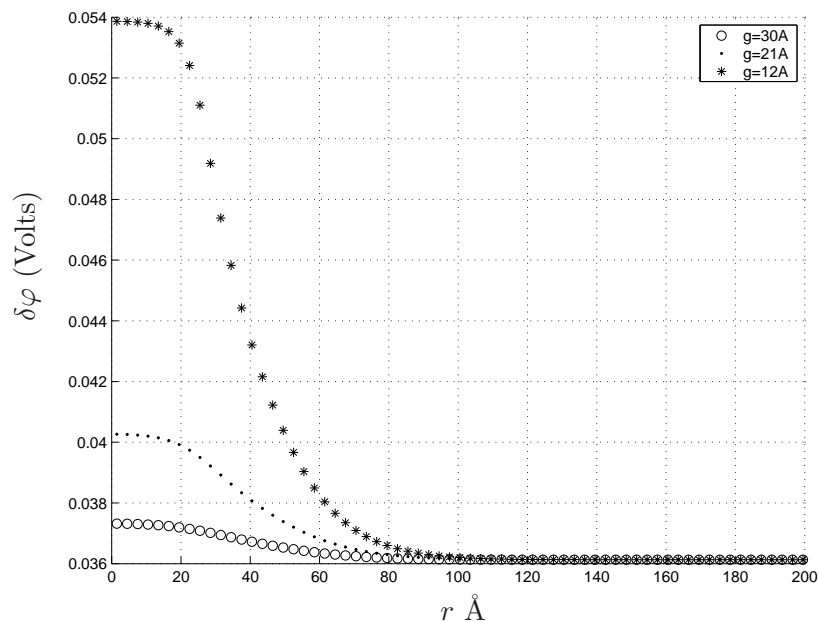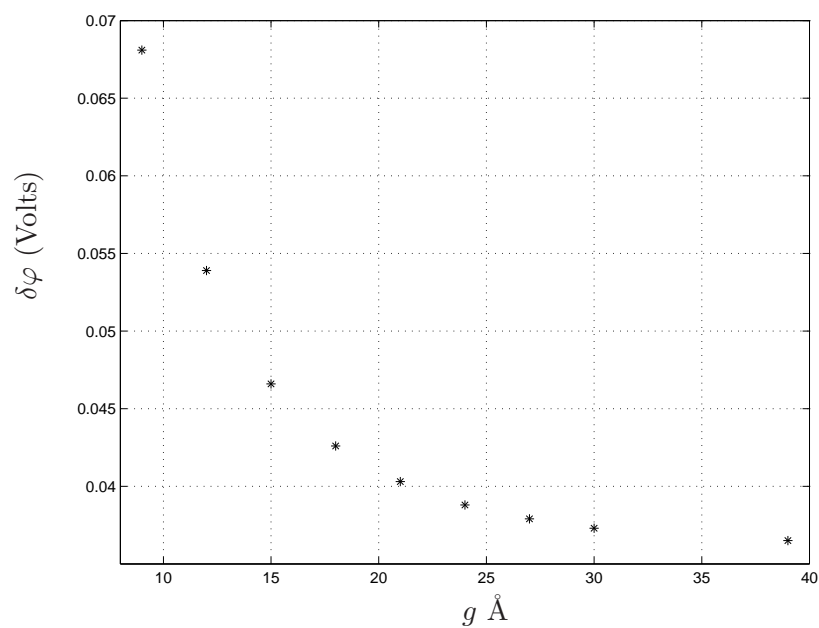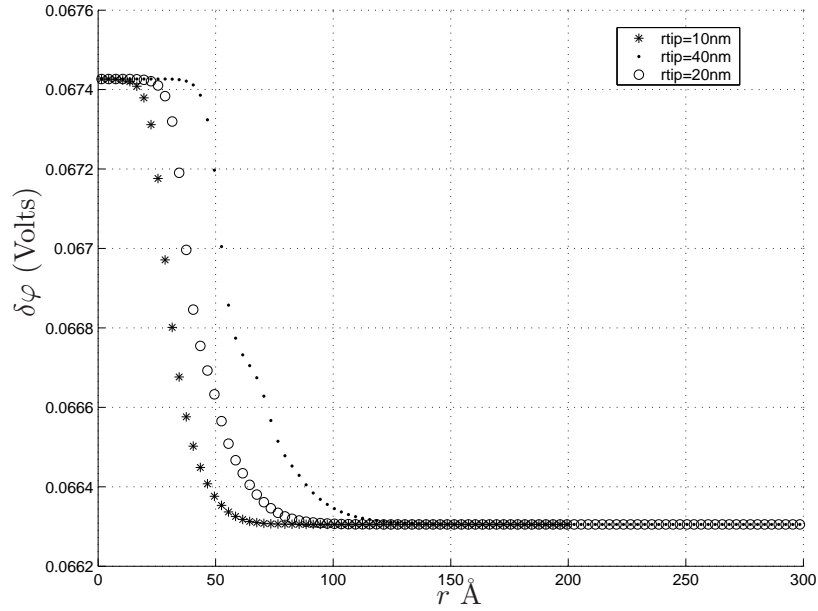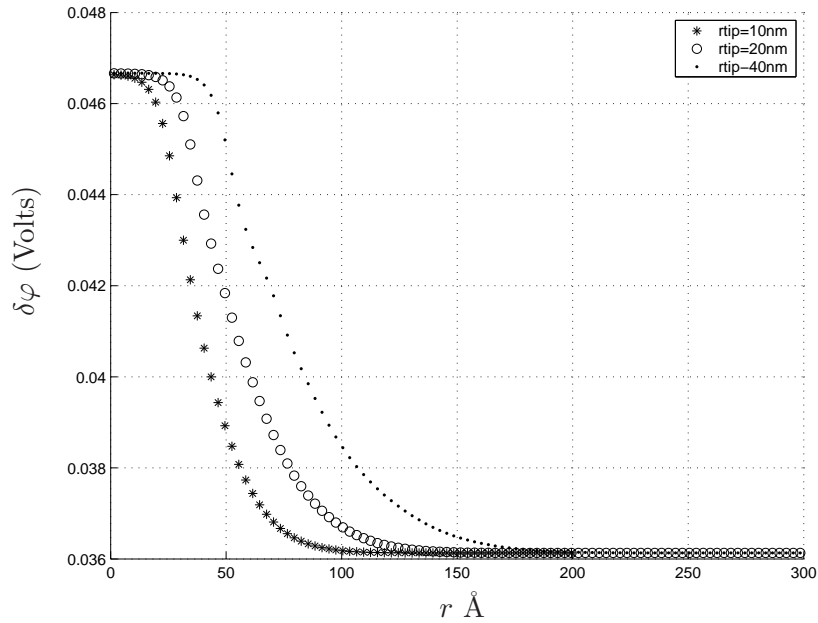
(a) Potential drop across x_{OHP} (taken as 3 Å) on the sample surface

(b) Effect of gap. Potential drop across x_{OHP} at $r = 0$

Figure 3.12: Influence of gap at high concentration. Simulation conditions – $r_{tip} = 100$ Å, $\theta = 45°$, 1:1 electrolyte with $q = 1$ and conc. 1 M, $\varphi_{tip} = 0.1$ V and $\varphi_{sample} = -0.1$ V

(a) Potential drop across x_{OHP} (taken as 3 Å) on the sample surface.

(b) Effect of gap. Potential drop across x_{OHP} at $r = 0$

Figure 3.13: Influence of gap at moderate concentration. Simulation conditions – $r_{tip} = 100$ Å, $\theta = 45°$, 1:1 electrolyte with $q = 1$ and conc. 0.1 M, $\varphi_{tip} = 0.1$ V and $\varphi_{sample} = -0.1$ V
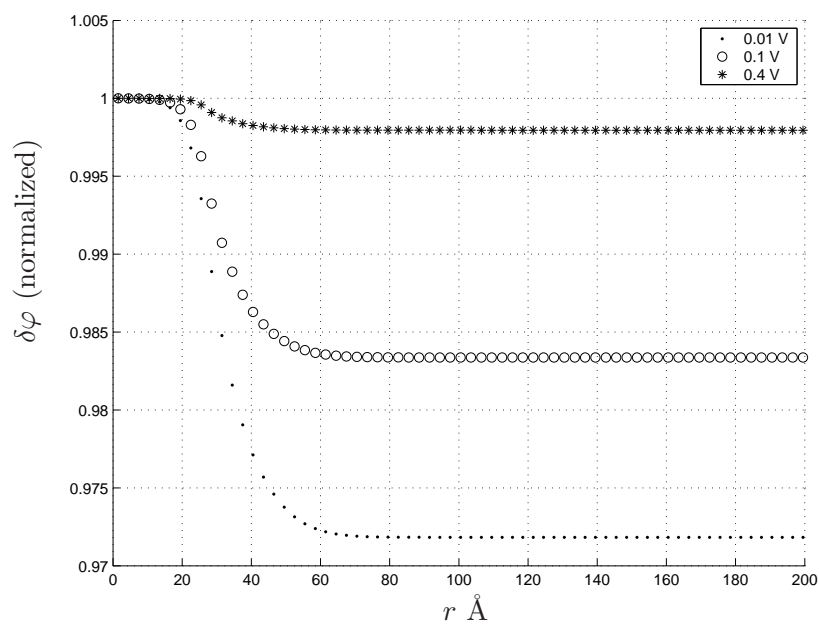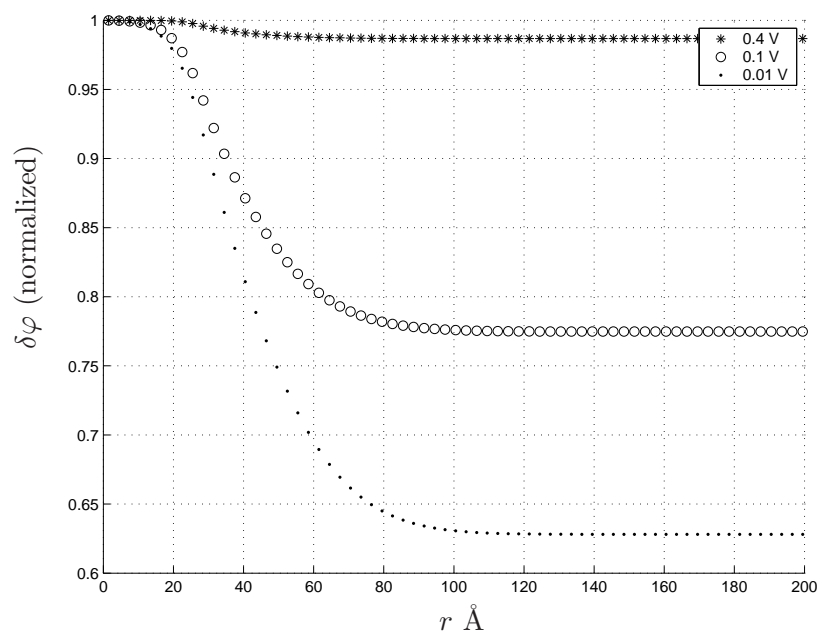
(a) High concentration - 1 M

(b) Moderate concentration - 0.1 M

Figure 3.14: Influence of tip radius. Potential drop across x_{OHP} (taken as 3 Å) on the sample surface. Simulation conditions – $g = 15$ Å, $\theta = 45°$, 1:1 electrolyte with $q = 1$, $\varphi_{tip} = 0.1$ V and $\varphi_{sample} = -0.1$ V

(a) High concentration - 1 M

(b) Moderate concentration - 0.1 M

Figure 3.15: Influence of applied potential. Potential drop across x_{OHP} (taken as 3 Å) on the sample surface. Simulation conditions – $r_{tip} = 100$ Å, $g = 15$ Å, $\theta = 45°$, 1:1 electrolyte with $q = 1$, $\varphi_{tip} = -\varphi_{sample}$

3.3 Dynamics – transport of ions

So far we looked at the equilibrium fields and charge distributions. In this section, we look at the time evolution of charge distribution and fields under the tip (or the *tertiary current distribution* which takes into account concentration overpotential on top of activation overpotential and solution resistance). When a potential is applied between tip and sample, ions move under the influence of fields. Mobile ions charge the double layer capacitance. Once the double layer capacitance is charged, reactions can occur. If the electrodes are far away, one can model the system with a network of resistors and capacitors as shown in Fig. 3.16. Time evolution then gives which capacitors are charged and to which extent, thereby giving where the reaction takes place. This kind of analysis has been done for electrochemical micromachining with ultrashort voltage pulses [71].
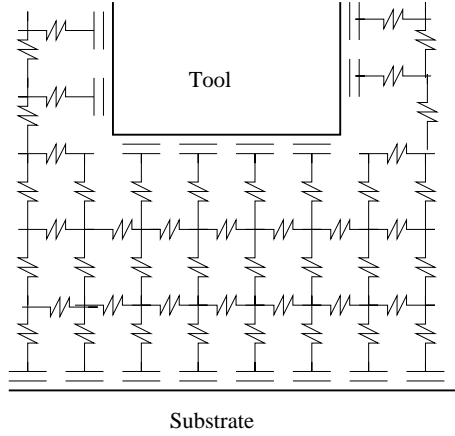

Figure 3.16: Network of resistors and capacitors to model electrochemical system

For an electrolyte with 1M concentration, resistivity $\sim 3\Omega cm$ and double layer capacitance is $\sim 30\mu F/cm^2$. Assuming a gap between tool and substrate of $1\mu m$, the charging time $\tau = RC \sim 20 nanosec$. At this time scale parts of the substrate much further away than $1\mu m$ will be uncharged. Application of ultrashort voltage pulses can in this way localize electrochemical reactions.

For an ESTM geometry, where tip and sample double layers may be interfering, such a resistor capacitor network can not be used. The system must be modelled by considering diffusion and electromigration of ions. For an electrolyte containing several ionic species, i^{th} species has electronic charge $q_i e$, species current density due to diffusion is given by

$$\vec{j^i}_{diff}(\vec{r}) = -D^i \vec{\nabla} n^i(\vec{r}) \tag{3.25}$$

where D^i is the diffusion coefficient of the ith species. Species current density due to electro-

migration is given by

$$\vec{j^i}_{em}(\vec{r}) = \frac{q^i}{|q^i|}\mu^i \vec{E}(\vec{r})n^i(\vec{r})$$

$$\vec{j^i}_{em}(\vec{r}) = \frac{q^i}{|q^i|}\mu^i(-\vec{\nabla}\varphi(\vec{r}))n^i(\vec{r})$$

$$(3.26)$$

where μ^i is the mobility of the ith species, $\vec{E}(\vec{r}) = -\vec{\nabla}\varphi(\vec{r})$ is the electric field at $(\vec{r})$. D^i is related to μ^i by the Einstein-Smoluchowski relation $D = \frac{\mu k_B T}{qe}$ where T is the temperature and k_B is the Boltzmann constant.
Total current density is just the sum of the two :

$$\vec{j^i}(\vec{r}) = \vec{j^i}_{diff}(\vec{r}) + \vec{j^i}_{em}(\vec{r}) \tag{3.27}$$

Continuity equation gives

$$\frac{\partial n^i(\vec{r})}{\partial t} = -\vec{\nabla} \cdot \vec{j^i}(\vec{r}) \tag{3.28}$$

Total charge density is given by

$$\rho(\vec{r}) = \sum q^i n^i(\vec{r}) \tag{3.29}$$

and the electric field is given by the Poisson equation

$$\nabla^2\varphi = -\frac{\rho}{\epsilon_0\epsilon_r} \tag{3.30}$$

To summarize the equations given above

$$\frac{\partial n^i(\vec{r},t)}{\partial t} = D^i\nabla^2 n^i + \frac{q^i}{|q^i|}\mu^i n^i \nabla^2\varphi + \frac{q^i}{|q^i|}\mu^i\vec{\nabla}\varphi \cdot \vec{\nabla}n^i$$

$$\rho = \sum q^i n^i$$

$$\nabla^2\varphi = -\frac{\rho}{\epsilon_0\epsilon_r}$$

$$(3.31)$$

These equations are valid when one can define the densities. Normally density is defined by *coarse graining* in space, i.e. one considers relatively large cells and density is defined by the number of particles in a cell divided by cell volume. For the geometry of an ESTM, the cell size will be so small that we will not be able to define density as a continuous differentiable variable. In order to overcome this problem, we consider a very large number of copies of the system. We then define

$$\langle n^i(\vec{r})\rangle = \frac{1}{N}\sum_{k=1}^{N} n^{i,k}(\vec{r}) \tag{3.32}$$

where $n^{i,k}(\vec{r})$ is the density of the i_{th} species in the kth system, defined in the usual sense. While $n^{i,k}(\vec{r})$ may not be continuous and differentiable, for $N \to \infty$, $\langle n^i(\vec{r})\rangle$ becomes con-

tinuous and differentiable. It can be shown that Eq. (3.31) can be rewritten as

$$\frac{\partial \langle n^i(\vec{r},t) \rangle}{\partial t} = D^i \nabla^2 \langle n^i \rangle + \frac{q^i}{|q^i|} \mu^i \langle n^i \nabla^2 \varphi \rangle + \frac{q^i}{|q^i|} \mu^i \left\langle \vec{\nabla}\varphi \cdot \vec{\nabla} n^i \right\rangle$$

$$\langle \rho \rangle = \sum q^i \langle n^i \rangle \tag{3.33}$$

$$\nabla^2 \langle \varphi \rangle = -\frac{\langle \rho \rangle}{\epsilon_0 \epsilon_r}$$

where $\langle \dots \rangle$ means ensemble average. Under the mean field approximation, $\varphi^k(\vec{r},t) \approx \langle \varphi(\vec{r},t) \rangle$ for an overwhelmingly large number of k, one reverts back to Eq. (3.31) with φ and n^i considered as ensemble averages.

For the ESTM geometry, Eq. (3.31) is solved under cylindrical co-ordinate system using finite difference method. The grid used is the same as that for the equilibrium case, Fig. 3.9(a). The boundary condition used on outer and inner boundaries is the Neumann boundary condition $\frac{\partial \varphi}{\partial \hat{n}} = 0$ and $\frac{\partial n^i}{\partial \hat{n}} = 0$. The intersection of the outer boundaries is considered to be a bulk point with potential zero and bulk concentrations. Such boundary condition on the outer boundary is not absolutely correct but there are reasons to believe that it is a good approximation –(a) electric fields are perpendicular to the tip and sample surfaces, (b) for $t \to 0$, at $r \gg 0$ $\vec{E} \to 0$, (c) for $r \gg 0$ and far from the surfaces, $n^i \to n^i_{bulk}$, (d) at steady state this boundary condition is valid and (e) exact shape of the outer boundary has small influence on the solution near $r = 0$. Points that represent the tip and sample surfaces are at φ_{tip} and φ_{sample} respectively. Densities at tip and sample boundaries are meaningless. Space derivatives are calculated using the approximation given in Eq. (3.24).

For the nodes in the solution just outside tip or sample, $\frac{\partial n^i}{\partial t}$ is calculated using current densities as explained below. Consider Fig. 3.17, where T represents a node on tip surface, S is in the solution and P is just next to tip. A and B are surfaces perpendicular to z direction. Assuming only z current,

$$\frac{\partial n^i(P)}{\partial t} = \frac{j^i(A) - j^i(B)}{\Delta z}$$

$$j^i(A) = 0 \tag{3.34}$$

$$j^i(B) = -D^i \left(\frac{n^i(P) - n^i(S)}{\Delta z} \right) - \frac{q^i}{|q^i|} \mu^i \left(\frac{n^i(P) + n^i(S)}{2} \right) \left(\frac{\varphi(P) - \varphi(S)}{\Delta z} \right)$$

Similar treatment is done in r direction where required.

A typical solution of Eq. (3.31) is shown in Fig. 3.18. Simulation conditions – $r_{tip} = 60$ Å, $g = 30$ Å, $\theta = 45°$, 1:1 electrolyte with $q = 1$, concentration 0.1 M, $D = 10^{-5} cm^2/sec$ $\varphi_{tip} = 0.1$ V and $\varphi_{sample} = -0.1$ V. Fig. 3.18(a) shows how the potential develops on the sample surface in time while the rest show the extent of double layer charging in time. In the simulation, the units of length and diffusion coefficient can be chosen arbitrarily while forcing the unit of concentration and time.
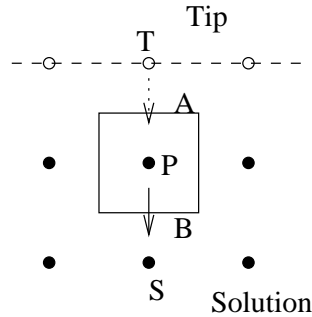
Figure 3.17: Nodes in electrolyte just outside tip or sample.

Influence of different parameters

Influence of concentration – Concentration directly affects the resistivity of the solution. So it is natural that a highly concentrated solution should allow rapid build-up of potential on the sample surface compared to low concentration solution. Figs. 3.19(a) and 3.19(b) show that for a 1 M concentration, double layer is charged upto ~ 50 nm in 2 ns, while for a 0.1 M solution, it takes ~ 20 ns (see figures for simulation conditions).

Influence of geometry – For very small tip to sample gap, as is the case in an ESTM, the effect of gap is visible in the field strength and since the field peaks sharply at $r = 0$ (at $t = 0$), double layer is charged faster near $r = 0$. The time of double layer charging far away is unaffected by the gap. This is visible in Fig. 3.20(a). Similarly tip radius has effect on charging time only near $r = 0$ (Fig. 3.20(b)). Only the tip angle influences charging time far away appreciably. This is seen in Fig. 3.20(c) and readily understood. Large angle or flat tip implies that for $r \neq 0$, distance between tip and sample is small and hence the electrical resistance is small.
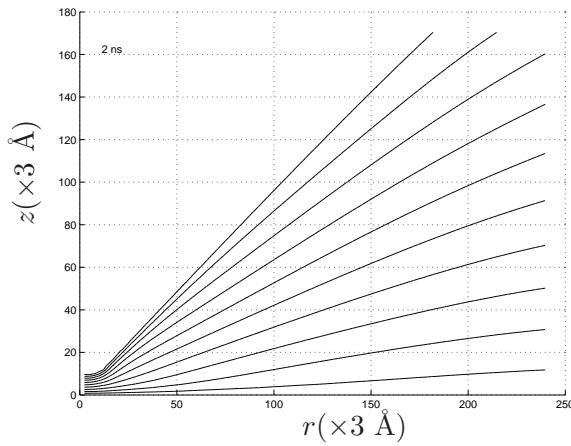
An example with a tip geometry closer to what is usually used in experiments and a much higher time scale, is shown in Fig. 3.21. Simulation conditions – $r_{tip} = 33$ nm, $g = 4$ nm, $\theta = 45°$, 1:1 electrolyte with $q = 1$, concentration 0.1 M, $D = 10^{-5} cm^2/sec$ $\varphi_{tip} = 0.01$ V and $\varphi_{sample} = -0.01$ V.
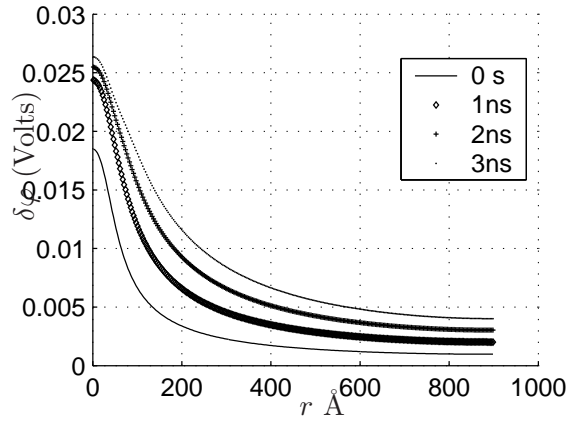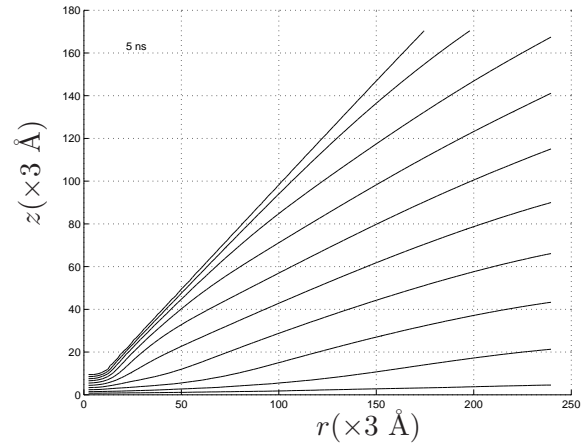
(a) Potential drop across x_{OHP} (taken as 3 Å) on the sample surface at different time.
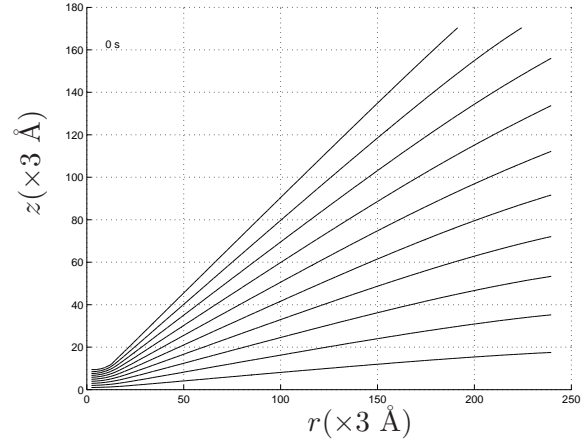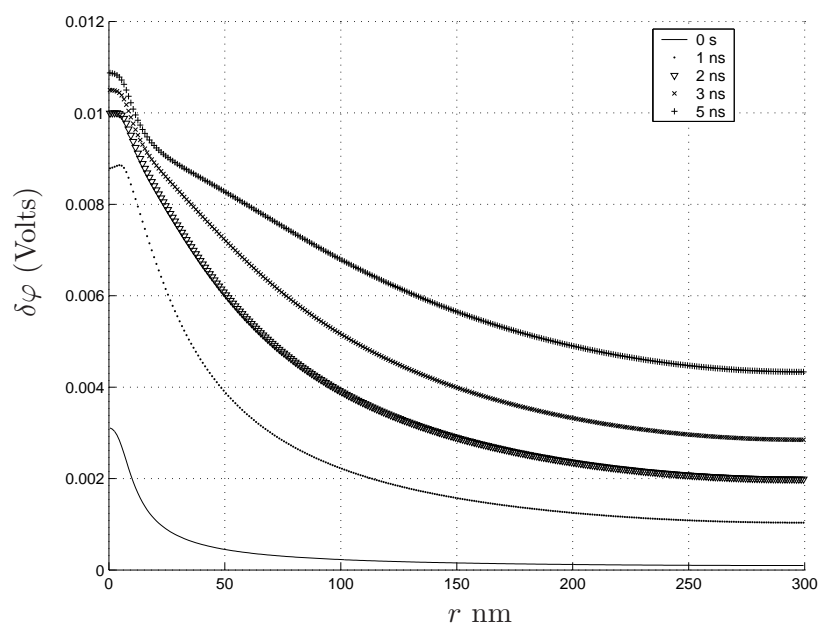

(b) 0 sec

(c) 2 ns

(d) 5 ns

Figure 3.18: Equipotential lines showing charging of double layer capacitance. Simulation conditions – $r_{tip} = 60$ Å, $g = 30$ Å, $\theta = 45°$, 1:1 electrolyte with $q = 1$, concentration 0.1 M, $D = 10^{-5} cm^2/sec$, $\varphi_{tip} = 0.1$ V and $\varphi_{sample} = -0.1$ V.

(a) Concentration 1 M
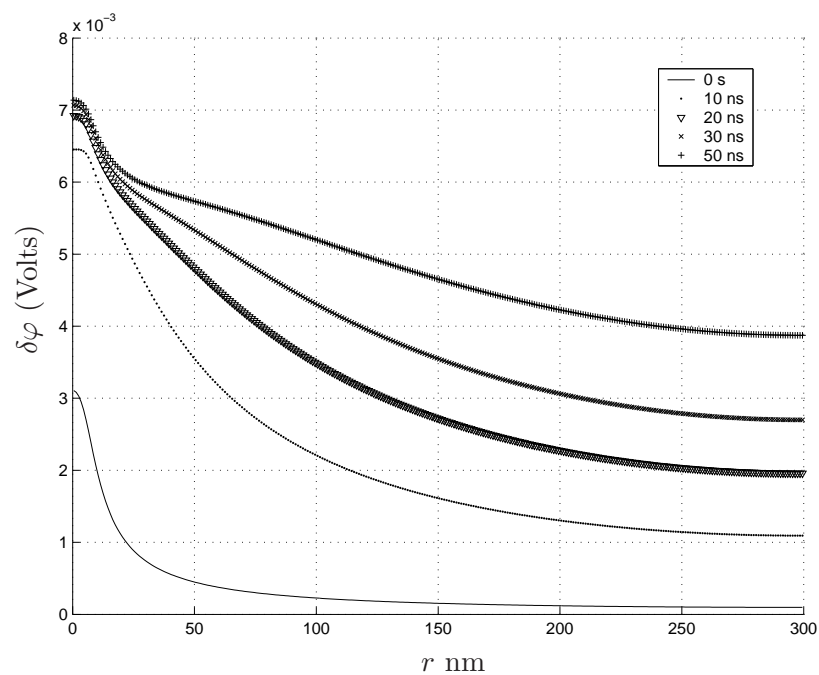
(b) Concentration 0.1 M

Figure 3.19: Potential drop ($\Delta z = 1$ nm, smallest length unit in simulation) on the sample surface at different time. Simulation conditions – $r_{tip} = 100$ Å, $g = 60$ Å, $\theta = 45°$, 1:1 electrolyte with $q = 1$, $D = 10^{-5} cm^2/sec$, $\varphi_{tip} = 0.01$ V and $\varphi_{sample} = -0.01$ V.
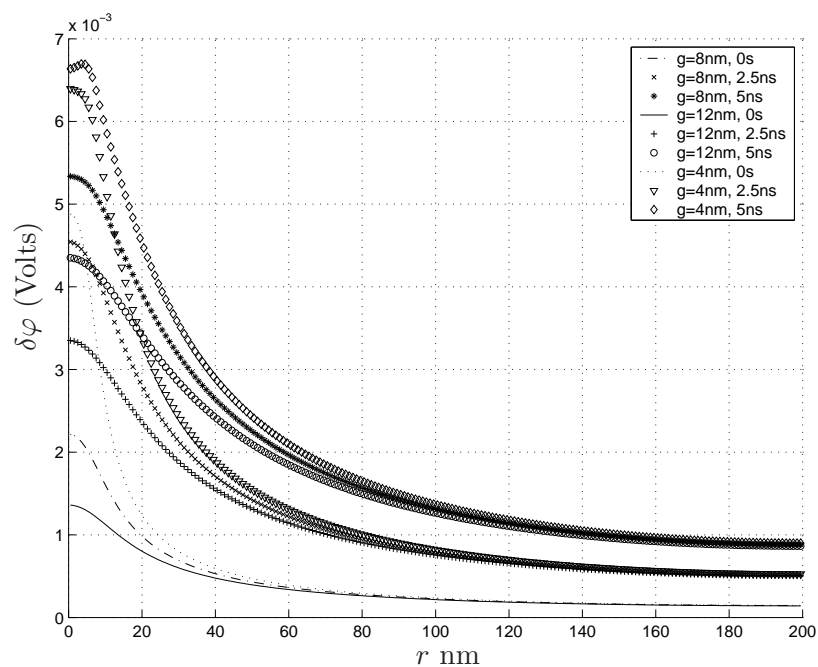
(a) Influence of g. $r_{tip} = 10$ nm, $\theta = 45°$
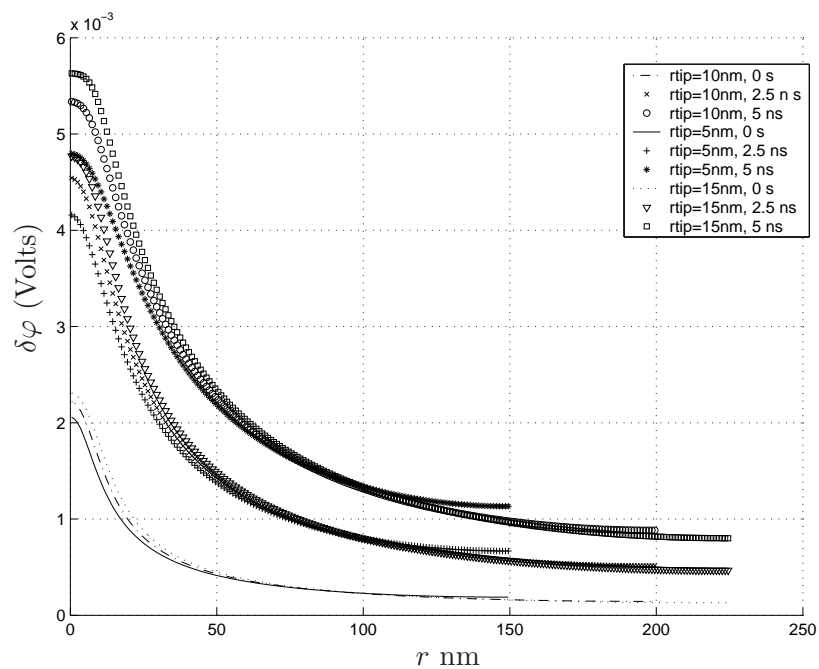
(b) Influence of r_{tip}. $g = 8$ nm, $\theta = 45°$
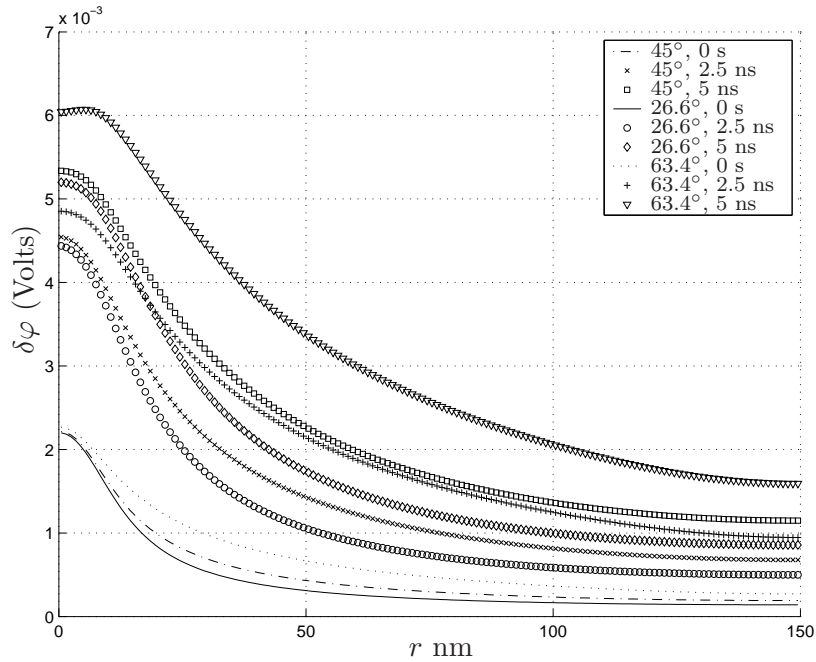
(c) Influence of θ. $r_{tip} = 10$ nm, $g = 8$ nm

Figure 3.20: Potential drop ($\Delta z = 1$ nm, smallest length unit in simulation) on the sample surface at different time. Simulation conditions – 1:1 electrolyte with $q = 1$ and concn. 0.1 M, $D = 10^{-5} cm^2/sec$, $\varphi_{tip} = 0.01$ V and $\varphi_{sample} = -0.01$ V.
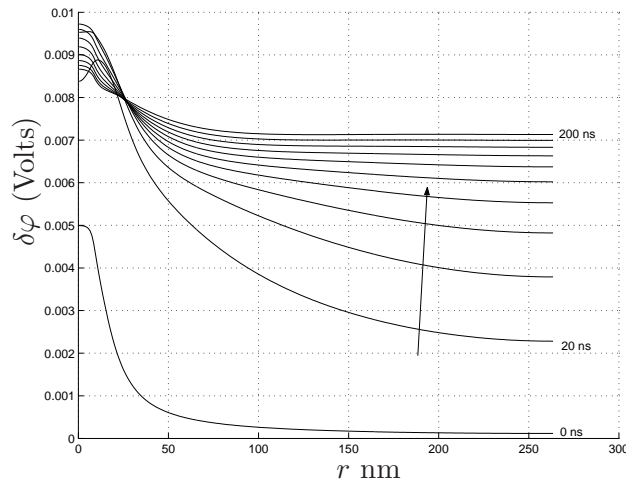
Figure 3.21: Double layer charging for a tip geometry closer to experiments. Potential drop ($\Delta z = 1$ nm) on the sample surface at different times. Simulation conditions – $r_{tip} = 33$ nm, $g = 4$ nm, $\theta = 45°$, 1:1 electrolyte with $q = 1$, concentration 0.1 M, $D = 10^{-5} cm^2/sec$, $\varphi_{tip} = 0.01$ V and $\varphi_{sample} = -0.01$ V. Arrow shows increasing time; time interval between consecutive curves = 20 ns.

Diffusion near tip end

Electrochemical reaction under the ESTM tip can occur following different physical processes. One common method is to use a high concentration supporting electrolyte with a small concentration of reacting species. In this situation the reaction on the sample depends on the potential developed at the sample surface, determined almost entirely by the supporting electrolyte, and the number of ions of the reacting species that diffuse to the reaction zone. Another possibility is that the reacting species is adsorbed on the surface and is depleted during the reaction. These could be replenished by switching off the reaction and allowing diffusion. It is therefore desirable to estimate the time it takes for ions to diffuse into the reaction zone or depleted zone. The equation governing diffusion is

$$\frac{\partial n^i(\vec{r}, t)}{\partial t} = D^i \nabla^2 n^i \tag{3.35}$$

As was mentioned in the last section, this equation is valid in the ensemble average sense. A first estimate of the diffusion time is simply the linear approximation, $\Delta t = \frac{\Delta l^2}{D}$ where Δl is the length scale to be covered. For $\Delta l = 100$ nm, and $D = 10^{-5} cm^2/sec$, $\Delta t = 10 \mu sec$. For an ESTM, if the tip is very sharp i.e. the tip radius is very small and the angle is small, then one can assume spherical diffusion to the region just below the tip. Spherical diffusion is faster than linear diffusion as it takes place through an increasing area as r increases. For blunt tips, i.e. tip radius is large, ions have to diffuse into the tip sample gap which can make diffusion slower. The general diffusion equation (3.35) was solved in the same way as Eq. (3.31).

For numerical modelling of diffusion, the ESTM geometry poses some problems. Tip-sample gap is very small compared to the interesting length scale for diffusion. This implies a very large number of nodes. Further, numerically the equation solved is

$$\frac{\partial n^i}{\partial t_{num}} = D^i_{num} \frac{\partial^2 n^i}{\partial l^2_{num}} \tag{3.36}$$

which is connected to Eq. (3.35) with the scales, $t = s_t \times t_{num}$, $l = s_x \times l_{num}$ and $D^i_{num} = s_D \times D^i$. This imposes the constraint $s_D \times s_t = s_x^2$. For a fixed s_D, s_t goes as s_x^2. So if we use small length scales, we need to use small time scales as well, which makes it computationally very time-taking. Therefore the diffusion equation has been solved with relatively large tip-sample gaps. This should still allow us to see the general trends and get some quantitative idea.

Replenishment

For the case of replenishment of ions in the depleted zone, as the initial condition, concentration in a region below the tip is set to zero. The boundary condition used on the outside boundary is constant density, $n^i = n^i_{bulk}$. Fig. 3.22 shows examples of the evolution of concentration near the sample surface. Notably for blunt tips and very low tip-sample gap, in a region near $r = 0$ determined by the radius, concentration becomes equal and approaches bulk value very slowly. Also worth noting is that the time of replenishment rises quickly with the volume of the depleted zone.
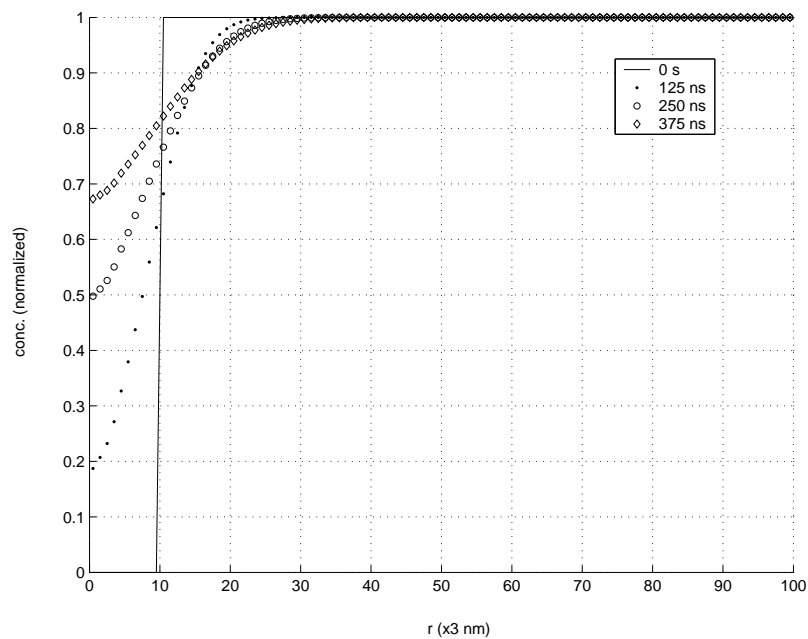
(a) $r_{tip} = 15$ nm, $g = 9$ nm. Initially $conc = 0$ for $r \leq 30$ nm.
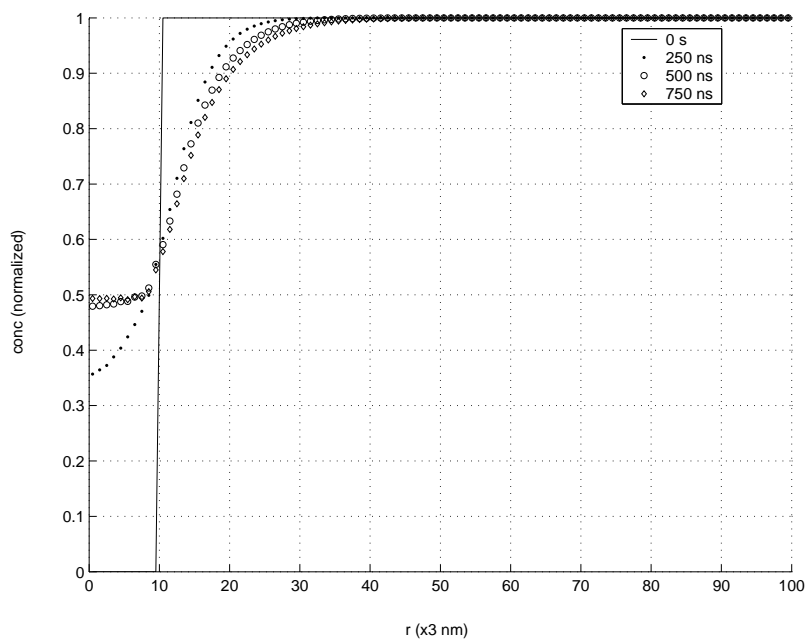
(b) $r_{tip} = 60$ nm, $g = 9$ nm. Initially $conc = 0$ for $r \leq 30$ nm.
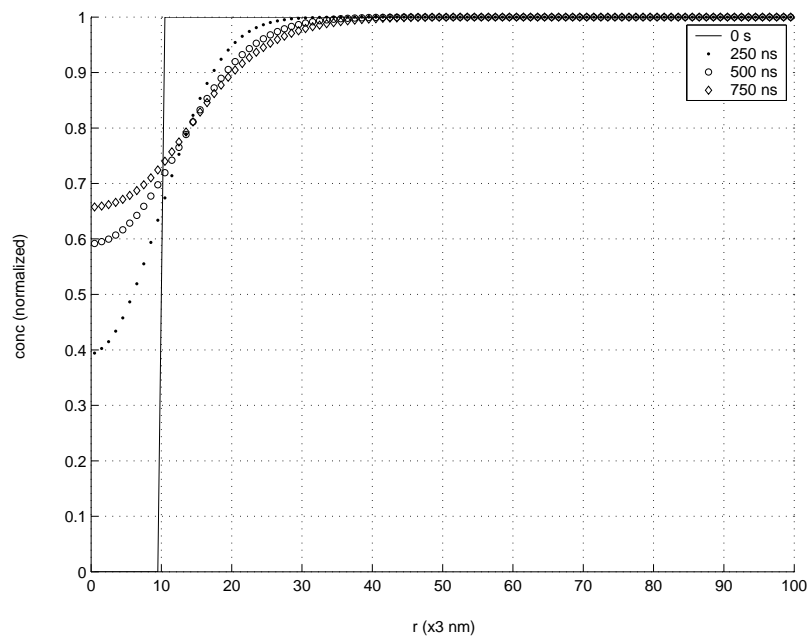
(c) $r_{tip} = 60$ nm, $g = 27$ nm. Initially $conc = 0$ for $r \leq 30$ nm.
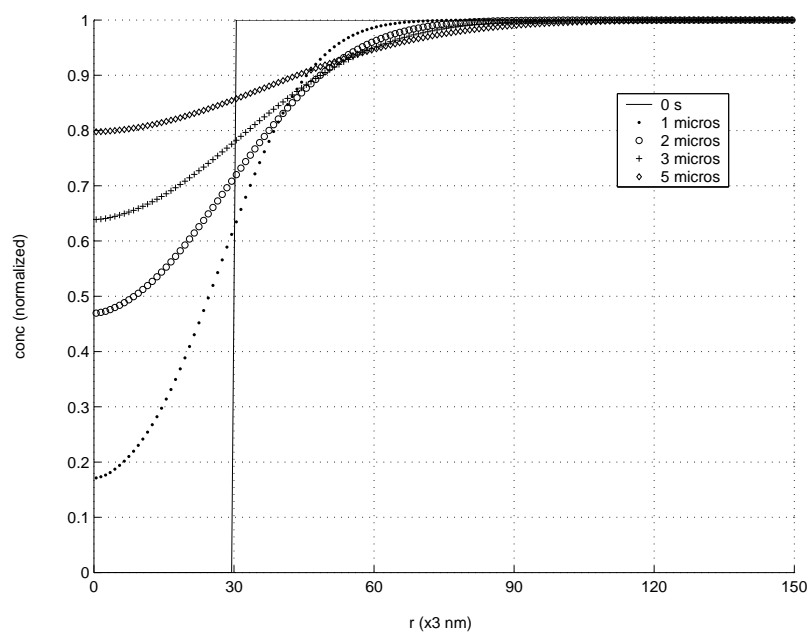
(d) $r_{tip} = 15$ nm, $g = 12$ nm. Initially $conc = 0$ for $r \leq 90$ nm.

Figure 3.22: Concentration next to the sample surface at different times. Simulation conditions – $\theta = 45°$, $D = 10^{-5} cm^2/sec$.

Diffusion from tip

In several ESTM based nanostructuring experiments, the tip is pre-loaded with the metal or has an adsorbed species which is released by changing the tip voltage. Under the situation that the double layers are charged much faster, the metal ions released from the tip will diffuse towards the substrate. To simulate this, the Eq. 3.35 is solved for the tip-sample geometry with the initial concentration on tip boundary as high and elsewhere equal zero. In the first step it is assumed that no reaction takes place on the substrate surface. But still it is useful, in that it gives an idea of the reaction zone. Fig. 3.23(a) shows how the reaction zone grows with time. In the next step, it is assumed that ions for reaction are supplied only from the tip and that all ions reaching the substrate react. The number of ions reacted as a function of r is shown in Fig. 3.23(b).
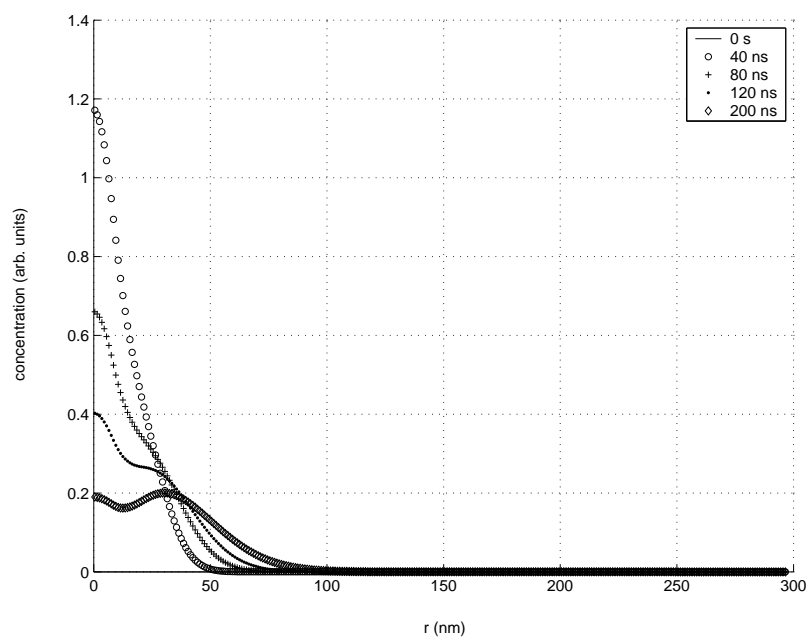
(a) Increase in size of reaction zone with time. Initially conc(tip) is high, elsewhere conc=0.
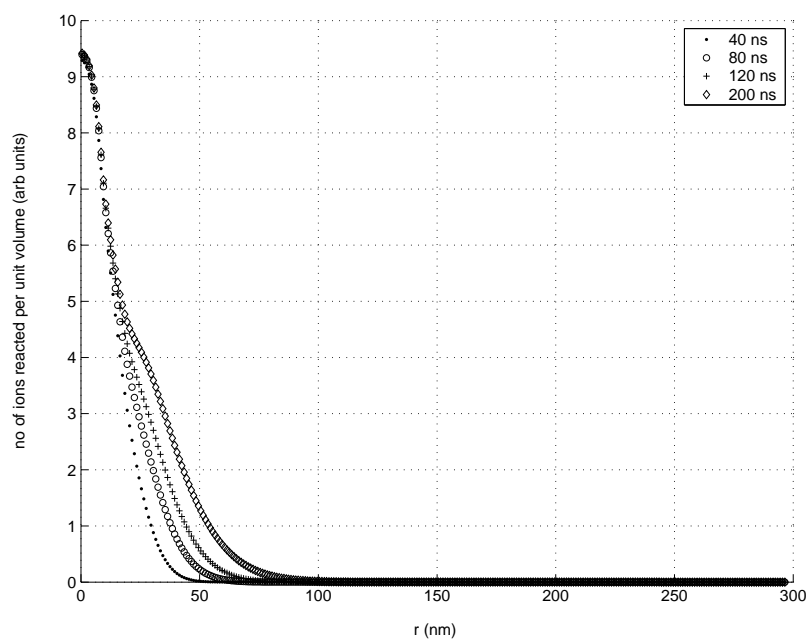
(b) Extent of reaction as a function of r.

Figure 3.23: Reaction zone as a function of time. Simulation conditions $- r_{tip} = 33$ nm, $g = 6$ nm, $\theta = 45°$, $D = 10^{-5} cm^2/sec$.

3.4   Cluster formation (2d)

When a number of metal ions react to form metal atoms on the sample surface in a zone near $r = 0$, depending upon the surface, these atoms can diffuse on the surface. Then the formation of stable clusters depends on the number of atoms, size of reaction zone, surface diffusion coefficient, binding energy between metal atoms, binding energy between metal/substrate and crystallographic misfit between metal and substrate.

For the case where deposition occurs by layer-by-layer growth (Frank-van der Merwe growth) or the first phase of island-on-layer growth (Stranski-Krastanov growth), and assuming that the metallic phase is thermodynamically stable (i.e. metal atoms do not reconvert to ions), one can model the formation of metal clusters by considering 2d diffusion on the underlying substrate lattice. This has been done with kinetic Monte Carlo (M.C.) simulations. Monte Carlo method solves the master equation

$$\frac{dP(S_j, t)}{dt} = -\sum_i W_{ji} P(S_j, t) + \sum_i W_{ij} P(S_i, t) \qquad (3.37)$$

where $P(S_j, t)$ is the probability of finding the system in the state S_j at time t and W_{ij} is the transition rate to move from state i to state j.

Consider the lattice shown in Fig. 3.24 with total number of points $\rightarrow N^2$. Small dots represent unoccupied sites and large dots are the metal atoms. In notations, the site (l, m) has a value of $s(l, m) = k$, $k \in \{0, 1\}$ where $k = 0$ represents empty sites and $k = 1$ represents a site occupied by a metal atom. Diffusion is equivalent to an exchange of s between neighbouring sites. Surface diffusion coefficient,

$$D^s = a^2 f \exp\left(-\frac{E_b}{k_B T}\right) \qquad (3.38)$$

where a is the length of a molecular jump (≈ 3 Å), f is the frequency factor ($\approx 10^{13} s^{-1}$) and E_b is the energy barrier to be overcome for an adatom. If D_0^s is the diffusion coefficient for an adatom without neighbours, then for an adatom with m neighbours,

$$D_m^s = D_0^s \exp\left(-\frac{U_m}{k_B T}\right) \qquad (3.39)$$

where U_m is the additional barrier and depends on m.

For a single exchange process, if the change in energy, $\Delta E \leq 0$, then transition rate is

$$W = \frac{2D^s}{a^2} \qquad (3.40)$$

and if $\Delta E > 0$

$$W = \frac{2D^s}{a^2} \times \exp\left(\frac{-\Delta E}{k_B T}\right) \qquad (3.41)$$

Simulation is straightforward. For a given state of the system, choose a lattice point randomly. Choose its neighbour randomly. Make an exchange based on the transition rate given above. Repeat this process a large number of times.
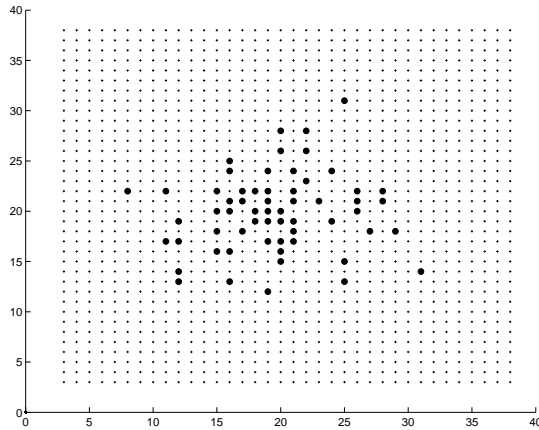
Figure 3.24: Lattice with metal atoms denoted by larger dots for Monte Carlo simulations.

On an average in N^2 M.C. steps, each lattice point is sampled once. Let real time $\Delta t = N^2$ M.C. steps. Then the probability of an exchange event (involving a given metal atom) in Δt, defined as p_{ex}, for which the transition rate is W, is given by

$$p_{ex} = W \times \Delta t \qquad (3.42)$$

Eq. (3.42) connects the M.C. time to real time and p_{ex} is set to 1. (Computationwise one would like to use large Δt (or large p_{ex}) to save time, but to be completely correct, Δt should be sufficiently small so that the probability of two events (involving a given metal atom) in Δt is negligible. For exchange event that implies $p_{ex}^2 \ll p_{ex}$ or $p_{ex} \ll 1$. However for diffusion, we could argue that long time effects will not be modified by setting $p_{ex} = 1$.)

Ultimately we are interested in calculating cluster size and distribution. Clusters are determined using Hoshen-Kopelman [100] (or union-find) algorithm. In the simulations square or hexagonal lattices can be used and different initializations (for metal atoms on substrate) - gaussian, uniform, regular - can be performed. For an exchange between a boundary point and its neighbour outside the boundary, it is assumed that the latter is an unoccupied site. This means that if a metal atom goes beyond the boundary it is considered lost.

Results and Discussion

In calculations here, it is assumed that $U_m = m \times U$, with U being the average metal/metal bond energy. Energy of the system is calculated directly from the number of metal/metal bonds, $E = \frac{1}{2}\sum_i m_i U$, where m_i is the number of nearest neighbours for the ith metal atom. A more precise calculation should take into account the dependence of energy on the co-ordination number, effect of substrate and also the effect of the electrolyte. For a system like Cu on Cu(111), even a single atom without neighbours on an otherwise smooth surface has a co-ordination number 3. And 2 neighbouring atoms on the surface with just one bond mean a coordination number of 4. The probability of a jump breaking that bond is $p_{ex} \exp\left(-\frac{U_4 - U_3}{k_B T}\right)$. Data from [101] and [102] gives $U_4 - U_3 = 0.30$ eV. At room temperature

that gives $p_{ex} \exp\left(-\frac{U_4 - U_3}{k_B T}\right) = p_{ex} \times 6.0 \times 10^{-6}$. That means the assumption of $U_m = m \times U$ with $U = 0.6$ eV (binding energy per bond for Cu) does not make a significant difference to the calculations. For a system like Pt on Au(111), since there is good lattice matching and high binding energy between Pt/Au, the same arguments hold. On the other hand for a system like Pt on HOPG, this argument is invalid. Calculation of U_m data for such a system is beyond the scope of this work.

The exact distribution of metal atoms, deposited on the surface, depends on the tip-sample geometry, the extent of double layer charging and the reaction kinetics. A simplification assumed in the following simulations is that the distribution is a gaussian i.e. the probability of finding an atom between r and $r + dr$ is given by $\frac{n}{\pi\sigma^2} 2\pi r e^{-r^2/\sigma^2} dr$ where n is the total number of metal atoms and σ is the spread in units of latice constant. A hexagonal lattice is considered with the distance between neighbouring lattice points taken to be one. $U = -0.98$ eV (binding energy per bond for Pt), however any value $\gg k_B T$ will give similar results. Each simulation is run for a time equivalent to 1000 possible jumps per metal atom. The distribution of clusters for $\sigma = 40$ with different n is shown in Fig. 3.25.

Fig. 3.26(a) shows the maximum cluster size plotted against the number of atoms n. The same data plotted against n/σ^2 in Fig. 3.26(b) shows that there is a critical value of surface density, $(n/\sigma^2)_{crit} \approx 1.5$, above which large clusters are formed and the cluster distribution changes radically. Smaller clusters which are stable on the time scale of the simulations, may actually be unstable on the observation time scale of several seconds or minutes.

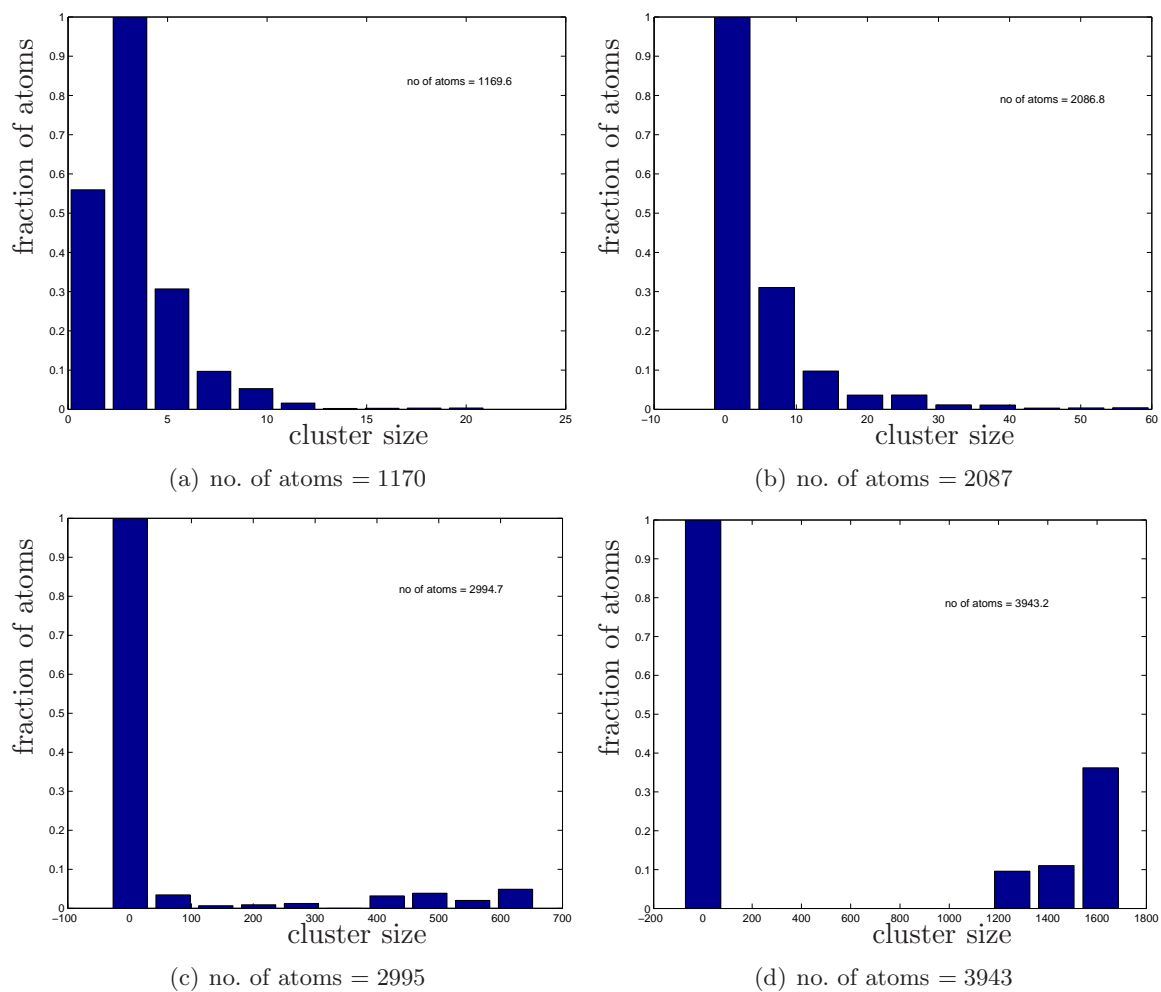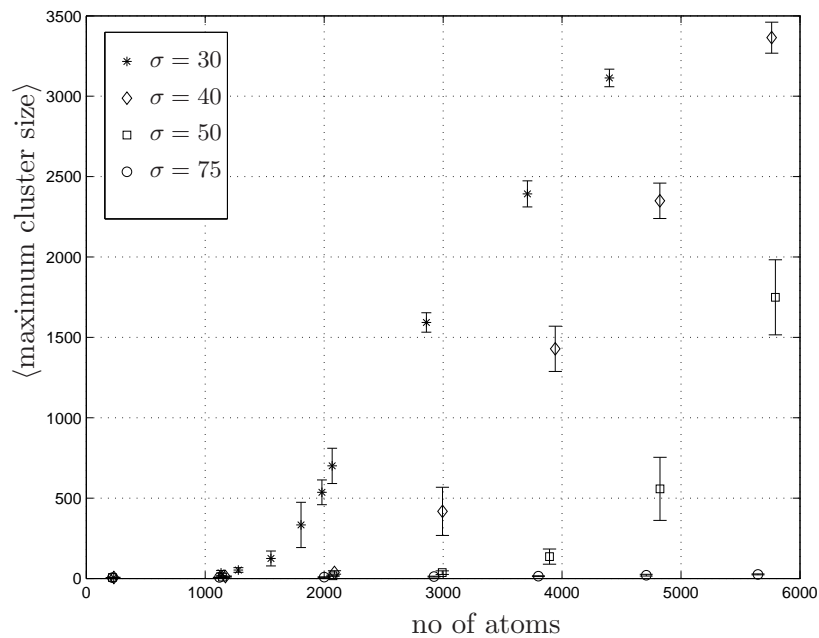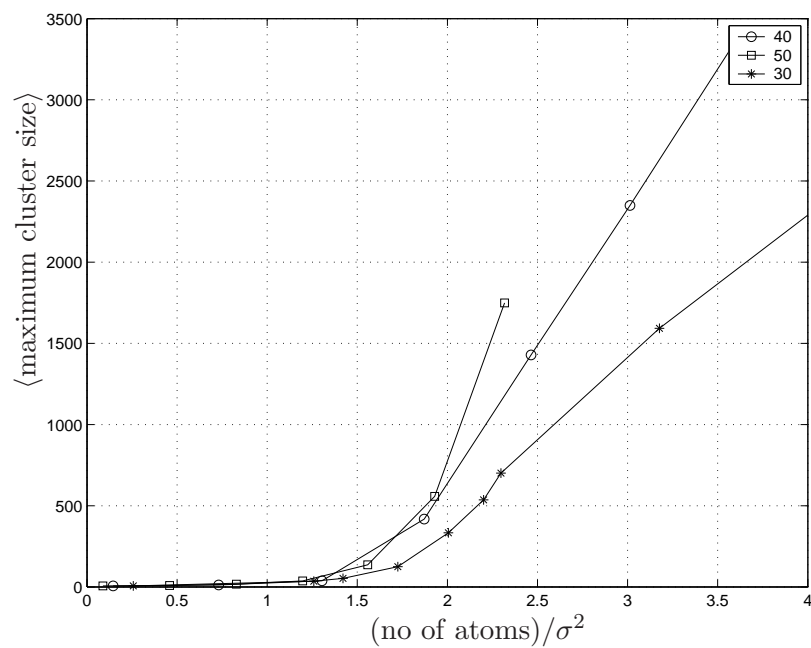Figure 3.25: Distribution of cluster size. Fraction of atoms in a cluster size = $\frac{\text{number of atoms in that cluster size}}{\text{total number of atoms}}$. Cluster size refers to the number of atoms in the cluster.

(a) Maximum cluster size vs initial number of atoms. The maximum cluster size is an average over 10 simulation runs.

(b) Maximum cluster size plotted against initial surface density of atoms.

Figure 3.26:

3.5 Summary

In this chapter fields and charge densities were calculated for an ESTM geometry in different conditions. These are directly related to different methods of nanostructuring with the ESTM tip. The first section showed that for a usual tip, field related processes will be limited to a diameter $2\sqrt{d_{tip}g}$. Then we looked at equilibrium charge distribution and double layer mixing. In order to optimally use the double layer mixing for structuring, two parameters are identified. One is to use moderate concentrations (~ 0.1 M) and second is to have tip-sample gap control. Next it was shown how the double layers charge in time for very short time scales. This is relevant for structuring with ultra-short voltage pulses. Here we observe that for $\sim 10-100$ ns pulses, concentrations ~ 0.1 M offer effective control on the size of reaction zone. For sharp tips, the geometry also affects the double layer charging mainly through the field strength. The part on diffusion, gives an idea of the time it takes for ions to diffuse to the region below the tip. It is shown that diffusion below blunt tips can be considerably slower compared to sharp tips. In the last section, Kinetic Monte Carlo simulations are used to predict the quality of deposits depending on the reaction zone (which depends on tip radius) and the number of atoms. It gives a critical value of surface density of atoms, $(n/\sigma^2)_{crit} \approx 1.5$, above which large clusters are formed. These calculations are, however, restricted to the case of 2d growth with high binding energy between metal/substrate.

Chapter 4

Electrolytical STM – Instrumentation

Experimental work with STM was done almost entirely with a home built STM designed specially for use in electrolyte. Some initial experiments were done with an old Park Scientific Autoprobe CP STM/AFM but it was soon realized that it imposed several limitations. Since there was no access to the internal control software, it was not possible to program complicated tasks e.g. to program the tip to move to desired location or to apply a pulse synchronized with a given signal. Secondly since it had a sample scanner, the electrochemical cell had to be kept small which led to rapid evaporation of the solution and consequently change in concentrations and large drifts. In view of these issues and keeping the cost considerations in mind, the new STM setup is designed on the Besocke setup and controlled using GXSM, an open source software developed for SPMs in general.

4.1   Mechanical Design

Optimum functioning of an STM requires tip-to-sample position control with picometer precision, a rough and and fine positioning capability in three dimensions and a scanning speed as high as possible. These requirements have to be satisfied in presence of building vibrations, temperature drifts and other perturbations. Pohl [103] has discussed general design guidelines for an STM.

Our setup is based on the classic Besocke beetle design [104]. Three piezo tubes resting on circular ramps as shown in Fig. 4.1 are used to drive the tip towards or away from the sample by slip-stick principle. These three tube piezos can also be operated in different configurations to achieve a coarse motion in the plane of the sample surface (x,y). A tube piezo in the centre is used as fine motion scanner for x,y and z directions. Our setup employs BM527 (lead zirconate titanate) tubes from SensorTech, Canada, with dimensions : length 19 mm, OD 6.35 mm, thickness 0.635 mm. That gives displacements of 22.0 nm/V in x,y and 6.5 nm/V in z.
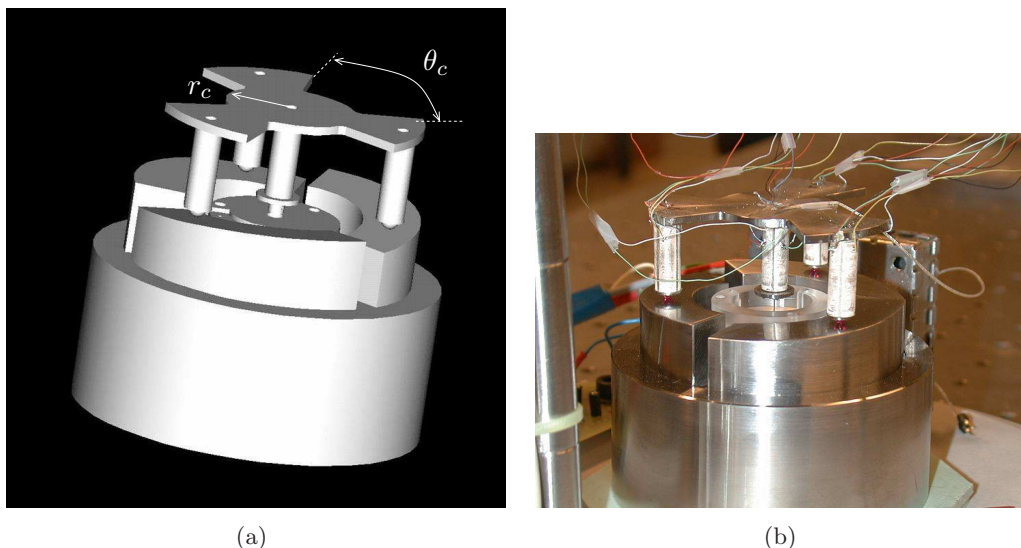
Figure 4.1: The STM in perspective view (left) and the real prototype (right).

The ramps have an average slope of about 2.4 °. On this slope only ± 15 volts are needed for the coarse motion. Typically for sawtooth voltage of 26 Volts peak-peak and 500 Hz, the unit can climb a distance of 1.8 mm in 10 minutes and go down the same distance in 5 minutes.

The Besocke design features circular symmetry and the outer tube piezos compensate for thermal expansion of the inner tube. This results in very low thermal drifts. In addition the whole setup is built of invar steel which has a very low coefficient of thermal expansion $(2 \times 10^{-6} \text{ K}^{-1})$.

For any STM, the mechanical resonance frequencies have to be kept high to eliminate any perturbations arising from environment vibrations. After fixing the dimensions of the electrochemical cell and the tube piezos, two parameters were identified to maximize the resonance frequency. They are the angle, θ_c, and radius of the cuts, r_c in the upper plate as shown in Fig. 4.1(a). The thickness of the plate also influences the resonance but has been fixed to readily available sizes. Finite element analysis is used to study and optimize the resonance. The curves for frequency versus r_c and θ_c are shown in Fig. 4.2. The resonance frequency drops to about 1.4 kHz after addition of the tip holder at the end of the central tube piezo. The first vibrational mode is shown in Fig. 4.3.

Vibration isolation is achieved by keeping the entire STM unit on a vibration isolation table (from TMC^{TM}, USA). Further two stages of heavy masses on soft rubber are added for additional damping. The table damps vibration above a few Hz and the additional stages provide further damping above ~ 10 Hz.

(a) First resonance frquency vs cut radius r_c.   (b) First resonance frquency vs cut angle θ_c.
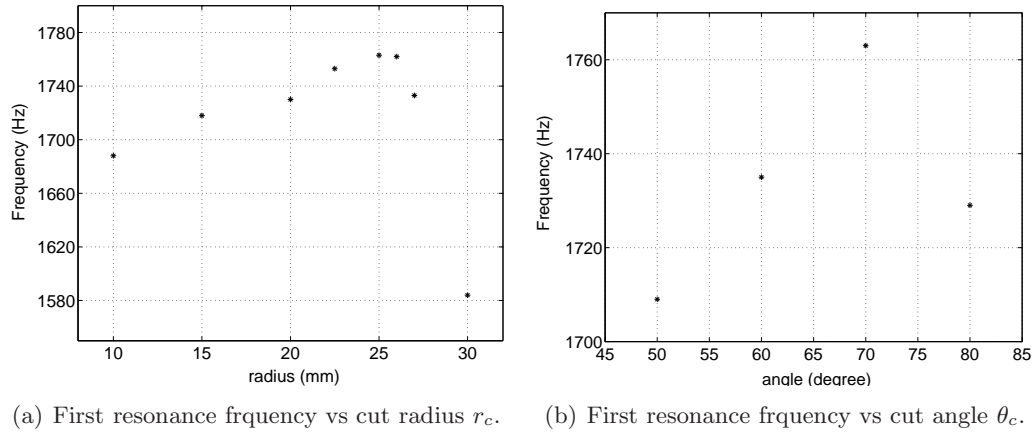
Figure 4.2: Curves for the resonance frequency. Tube piezo dimensions : length 20 mm, OD 6.35 mm, ID 5.0 mm. The upper plate is of invar steel and has 1 mm thickness.
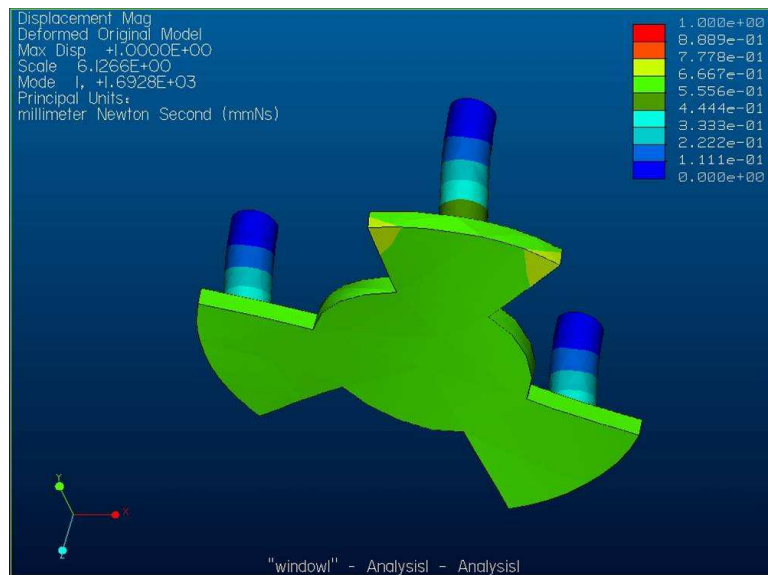

Figure 4.3: The first vibrational mode calculated from ProMechanica.

4.2 Control Software and Electronics

The STM is controlled by a linux based open source and freely available software called GXSM [105]. GXSM stands for Gnome X Scanning Microscopy, a software project for SPM control and image analysis. It also offers full hardware support for certain Digital Signal Processor (DSP) cards including open source DSP software and a growing set of SPM related electronics. Some of the salient features of GXSM particularly those that were useful for this thesis work are as described at their website [106]:

- "complete solution for all SPM needs: STM, AFM, SNOM, SARLS... and SPA-LEED

- complete SPM hardware: offering leading Digital Signal Processing (DSP) technology (realtime multitask statemachine) for feedback, scanning, vector probing and multi channel data acquisition

- GXSM core independent Plug-in hardware interface "HwI" allows to add support for any hardware without touching the GXSM core

- 2D..4D data acquisition and visualisation: Profile, Image and 3D rendered views

- event management: user triggered events like bias change, probe, etc. are attached by coordinate and time to the scan data

- im-/export plug-ins for many comercial SPM software (and some other) data formats

- python script language interface

   ..."

Two features that are worth emphasizing are the python script interface and vectorprobe. With the python script interface, simple programs can be written to set different parameters like scan range, tip position, PID control values and to execute tasks e.g. scan, save data etc. This allows automation of tasks that are repeated regularly. Vectorprobe is a tool within GXSM to provide well defined and synchronized signals to output channels. These features have been used for tip based nanostructuring tasks. Typically the python program commands the tip to move to a given point on the sample surface, followed by vectorprobe controlled output of a predefined voltage waveform on one of the output channels. This could be, for instance, a trigger to a function generator which in turn provides a voltage pulse to the tip.

GXSM interacts with a low cost DSP, Signal Ranger (Soft dB Inc., Canada) featuring Texas Instruments 16 bits fixed point DSP (TMS320VC5402 @100 MHz). The STM feedback control are run in the DSP and all analog input/output are provided by this board. Analog electronics for tunneling current amplification and piezo control are home built. Tunneling current amplifier is built from the electrometer grade opamp OPA 128 with a 100 MΩ feedback resistor giving an output of 100 mV/nA. Noise is measured at about 0.025 nA rms at 200 Hz bandwidth.

4.3 STM tips

Tungsten tips are quite commonly used in STMs. When used in an electrolyte the tip-sample capacitance is far more pronounced (relative permittivity of water is 78) and during a scan, a current comparable to the tunneling current may arise due to change in capacitance. To avoid this, tips must be very sharp. For nanostructuring with an STM tip, the structure dimensions also depend on the tip end diameter. Further for STM in electrolyte, the tip has to be insulated except the very end. For all these reasons, it is necessary to produce tips that have an end diameter as small as possible and a pronounced conical shape. Electrochemical etching of thin W wire to fabricate STM tips is a well studied method [107, 108].
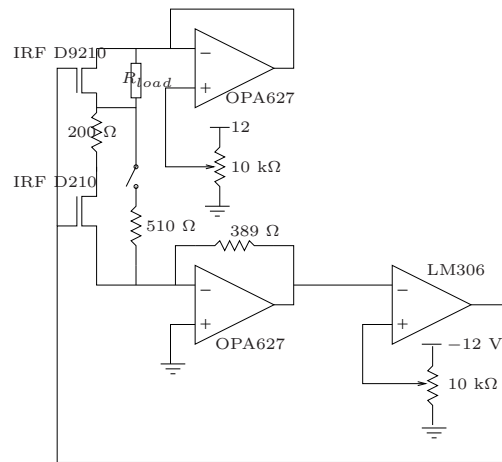

Figure 4.4: Circuit used for etching W tips. The circuit minimizes the electrochemical reaction cut-off time following "drop-off" of the lower part of the wire. R_{load} stands for the electrochemical cell impedance.

The electrochemical etching process involves the anodic dissolution of the metal electrode. Etching with direct-current (dc) provides sharp tips with a hyperboloid shape. In the present work the dc "drop-off" method is used in which etching occurs preferrentially near the air-electrolyte interface causing the portion of wire in solution to drop-off when its weight exceeds the tensile strength of the etched or necked down region of the wire. The upper part of the wire will continue to etch as long as it remains in the electrolyte under an applied voltage, also after the drop off of the lower part. This has a negative influence on the sharpness of the tip (upper part of the wire). It is therefore obvious that a very short cut off time of the etching current will produce sharper tips or smaller radius of curvature. This can be realised by using an electronic circuit with small cut-off time, which is triggered by the sudden voltage change when the lower part drops off. In literature one finds cut-off times from 100 ns to several μs to produce tips with radius from 10nm to 300nm [107, 108]. The etching circuit built in this work is shown in Fig. 4.4. The cut-off response measured is 50 to 100 ns. Fig. 4.5 shows SEM micrograph of a W tip prepared by this method.

Tips have been insulated by Apiezon wax, a chemically inert thermoplast [33, 34]. The apparatus to insulate the tip is shown in Fig. 4.6(a). A soldering iron is used to melt the
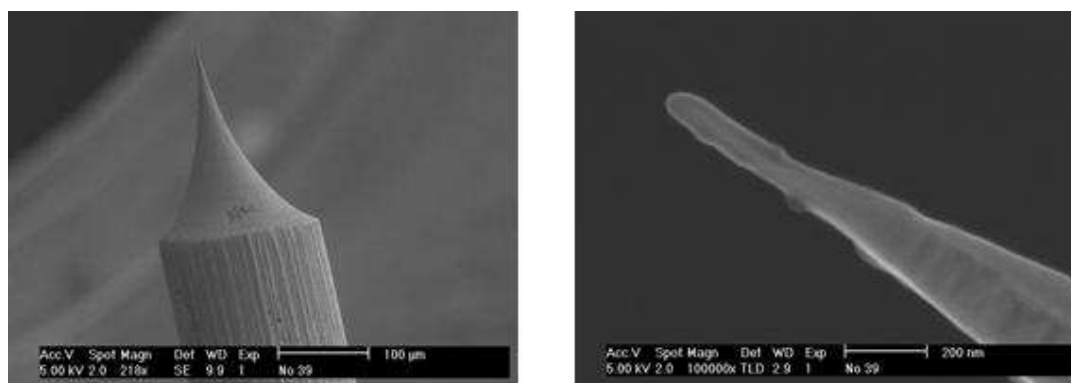
Figure 4.5: SEM micrographs of an etched W tip. Wires are etched in 10 %wt. NaOH with immersion depth of few mm at 3-6 V between tip and cathode. Etching time is about 5 minutes.

wax on a copper piece with a slit in the centre. The tip is brought into the molten wax from below, allowed to come in thermal equilibrium with the wax and raised through the wax. As the tip is raised, the molten wax flows down on its sides solidifying at the same time. The slit provides a temperature gradient - colder at the open end and hotter at the closed end. If the tip is raised at too hot a region, it is poorly insulated and if it is raised through too cold a region, it is completely covered. In between these two there exists an optimum position with an optimum temperature where the tip is nearly completely insulated. The insulated tip is moved sideways out of the groove.
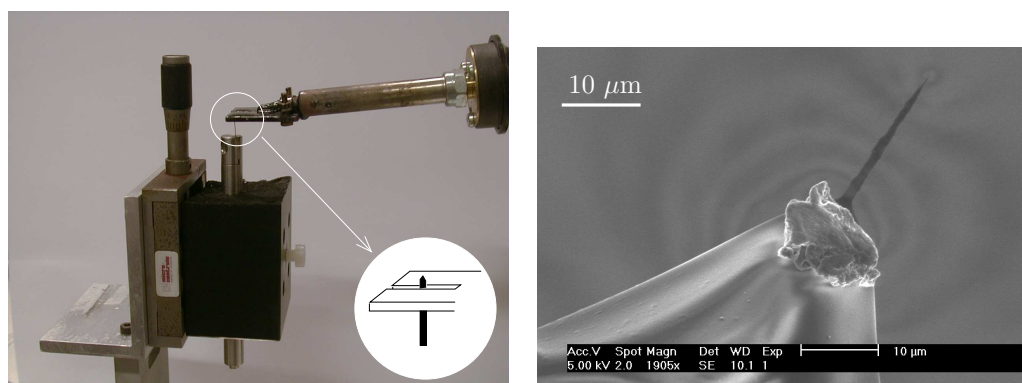
(a) Apparatus for tip insulation with Apiezon wax. Inset shows tip through the slit.

(b) SEM micrograph of a W tip insulated with Apiezon wax except the tip apex.

Figure 4.6: Tip insulation setup and a typical insulated tip.

Etching Pt or PtIr tips to make sharp tips is more complicated and has not been attempted. It is mentioned in passing that tips prepared from Pt by mechanical grinding and subsequent insulation by apiezon wax have also worked well for imaging. These tips are, however, not suitable for nanostructuring due to large tip radius.

4.4 Results

This section shows some imaging results from the home built STM. The performance in terms of vibration isolation and thermal drifts, specially when operating in electrolyte, is satisfactory. Drifts of few Å/second can be achieved. Some high resolution images taken in air are shown in Fig. 4.7.
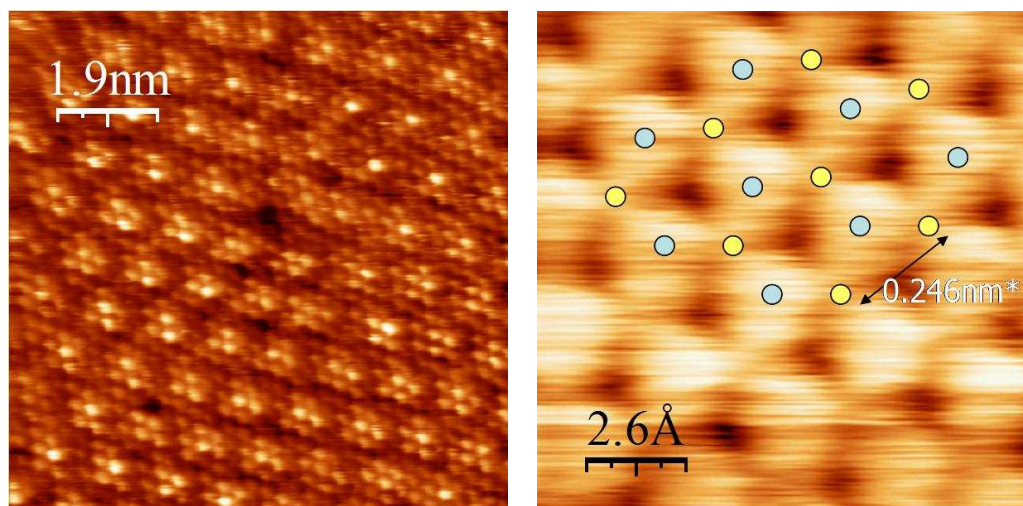
(a) Charge density waves on TaS_2. Image taken in constant height mode.

(b) Atomic resolution on HOPG. The known lattice constant (starred value) serves to calibrate the scanner.

Figure 4.7: STM images taken in air.

An electrochemical cell used for STM in electrolyte is shown in Fig. 4.8 with the section view shown in Fig. 4.9. The sample is placed on the sample support. Different supports of varying heights allow samples of different thicknesses. The base and support are built of invar. The cells are made of plexiglass and have a volume of about 1 ml. For potentiostatic control, wires (e.g. Pt) can be used as pseudo reference electrode and counter electrode. Fig. 4.4 shows atomic resolution image of HOPG taken inside an electrolyte.

Figure 4.8: A typical electrochemical cell used with the ESTM.

Figure 4.9: Section view of the electrochemical cell setup.
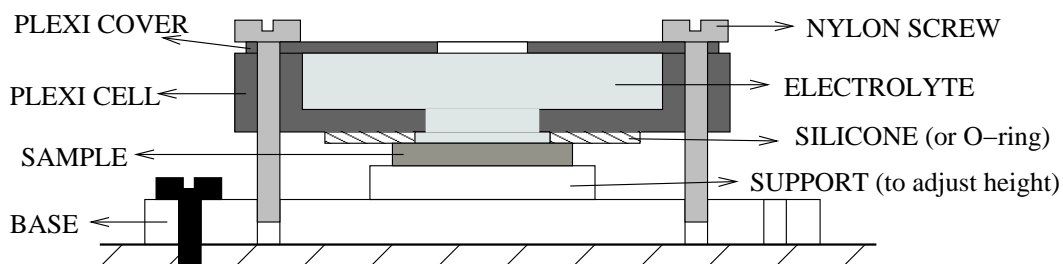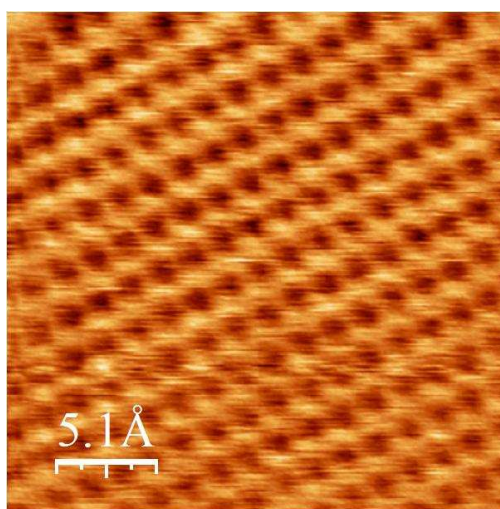

Figure 4.10: Atomic resolution image of HOPG in H_2PtCl_6 0.5 mM + $HClO_4$ 0.1 M. Potentiostatic control was applied with Pt wire pseudo reference electrode.

Chapter 5

Experimental Results – Pt on HOPG

Carbon-supported platinum nano particles are widely used as electrocatalysts, e.g. for fuel oxidation and oxygen reduction in low temperature fuel cells. There is considerable research in correlating the catalytic activity of Pt and other noble metal nano particles with their size and morphology. In this respect there is interest in studying Pt and similar metal particles deposited on well defined electrodes like HOPG. On the other hand there is large interest in novel techniques for fabrication of structures in the nanometer range. This chapter deals with the investigations of ESTM based deposition of Pt on HOPG basal plane. In a solution containing H_2PtCl_6, $\sim$5 Volts, μs voltage pulses between tip and sample are shown to create local deposits. The influence of the pulse width and amplitude, tip and concentration are explored. Depending upon the conditions, it is possible to create few $\leq$ 5 nm sized particles spread over a diameter of 50-100 nm or relatively large, 50-100 nm, growths on HOPG surface. The deposition is explained by transfer of adsorbed $[PtCl_6]^{2-}$ ions from the ESTM tip.

5.1 Background

Studies on electrochemical deposition of Pt on HOPG basal plane from $[PtCl_6]^{2-}$ containing solutions have been carried out by several groups [109, 110, 111]. Zoval et al. [109] used pulsed potentiostatic method to deposit Pt on HOPG with a narrow particle size distribution. In their method, they anodically protected the graphite surface by keeping it at 140-200 mV vs MSE (i.e. $\approx$ 200 mV positive of the onset for platinum deposition) and applied pulses of $\sim$-600 mV vs MSE for about 100 ms. The current-time transient was consistent with a simple Cottrelian decay indicative of planar diffusion control. They concluded that deposition occured via instantaneous nucleation and diffusion-limited growth. They also extracted the diffusion coefficient for $[PtCl_6]^{2-}$, $D = 5.89 \times 10^{-6}$ cm^{2}s^{-1}. They suggested a mechanism whereby growth should occur preferrentially on the steps and on the "delaminated" graphite islands. This is shown in Fig. 5.1. Since Pt particles are very difficult to observe with STM or with repulsive mode AFM, they concluded that Pt particles are weakly physisorbed on the graphite surface.
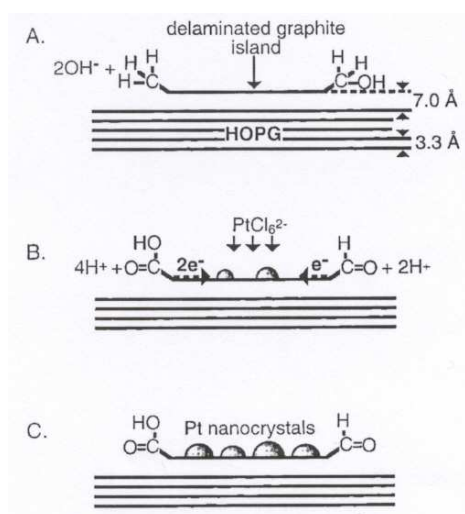
Figure 5.1: Scheme proposed by Zoval et al. [109] for preferential Pt deposition on delaminated graphite islands.

Gloaguen et al. [110] reported electrodeposition of Pt on thermally oxidized HOPG by chronoamperometry. In a solution of 0.1 M $HClO_4$ + 2 − 10 mM H_2PtCl_6, deposition by a potential step from 0.75 vs RHE (open circuit potential) to 0.1 V vs RHE shows that firstly, at $t < 0.3$ s, a large number of nanosized clusters are formed which maybe mobile and assemble in an accidental distribution of Pt agglomerates. At $t > 0.3$ s, more rapid growth of a small number of Pt particles gives a transient response adequately described by the model of Scharifker and Hills for a diffusion controlled growth. They found that for rather dilute solutions, 2 mM H_2PtCl_6, progressive nucleation occurs. They also estimated the diffusion coefficient of $[PtCl_6]^{2-}$, $D = 3.4 − 3.74 \times 10^{-6}$ cm^{2}s^{-1}.

Lu and Zangari [111] investigated Pt deposition on HOPG from H_2PtCl_6 by cyclic voltammetry and chronoamperometry. The effects of deposition overpotential, concentration, supporting electrolyte and anion additions were evaluated. By comparing potentiostatic current-time transients with the Scharifker-Hills model, a transition from progressive to instantaneous nucleation was found to occur when increasing deposition overpotential. Further they found that addition of chloride inhibits Pt deposition due to adsorbtion on the substrate and blocking of reduction sites, while SO_4^{2-} and ClO_4^- slightly promote Pt reduction.

Pt electrodeposition on HOPG has been studied by STM [112, 110] and AFM [113, 114, 109]. Zubimendi et al. [112] investigated the reaction mechanisms related to the early stages of Pt electrodeposition. Lee et al. [113] observed that Pt particles from 8 to 20 nm and heights from 0.5 to 2 nm are mobile and diffusion of these mobile particles plays an important role in the growth of platinum morphology. To summarize, deposition of Pt on HOPG from H_2PtCl_6 and $HClO_4$ occurs predominantly by nucleation and 3d growth and defects on HOPG are preferrential nucleation sites.
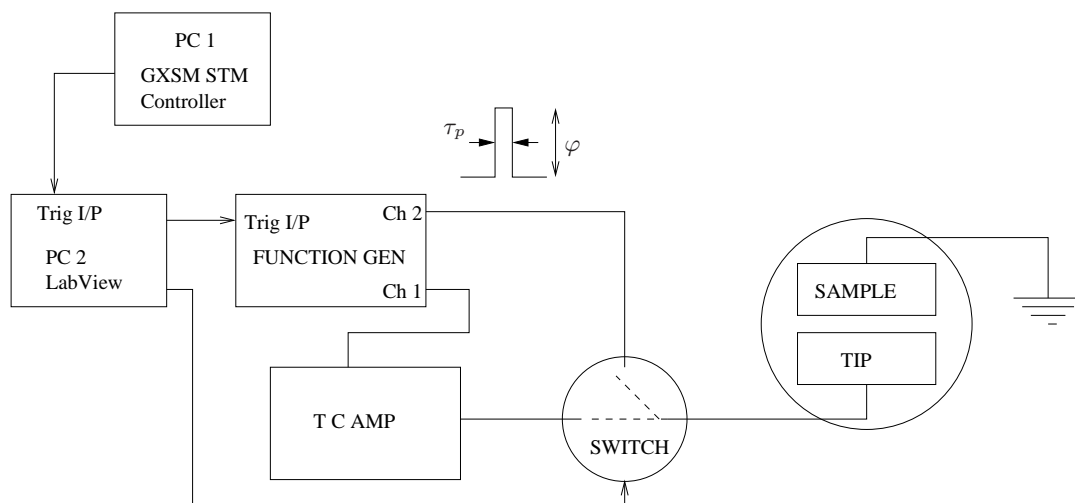
Figure 5.2: Setup of the experiment for deposition by μs pulses.

5.2 Experimental

HOPG samples from SPI Supplies® SPI-1 Grade, 10 mm × 10 mm × 1 mm, were used for the experiments. Before each experiment the samples were cleaved with a scotch tape to reveal fresh surface. Large atomically flat surfaces with few defects (usually steps) are easy to obtain. Electrolytes were prepared from $HClO_4$ (Merck, suprapur), Milli-Q water and H_2PtCl_6 (8 wt. % solution in water, Sigma-Aldrich). All measurements were done with home built electrolytical STM. Experiments were done in two electrode setup (no potentiostatic control). The experimental setup is shown in Fig. 5.2. Since the tunneling current amplifier has a bandwidth <1 kHz, the potential difference between the tip and substrate can not be modified at μs timescales. Therefore a switch is incorporated as shown, which switches the circuit from normal tunneling mode to pulsing mode. During the switching period, we have open circuit for a few milliseconds. Unless otherwise mentioned, experiments have been done with PtIr tips (PicoTips, Molecular Imaging).

5.3 Results and Discussion

Deposition mechanism

At the open circuit potential no adsorbed $[PtCl_6]^{2-}$ is present on HOPG surface. For a PtIr tip, on the other hand, at equilibrium, an adsorbed layer of $[PtCl_6]^{2-}$ is likely to be present. The basic idea of desposition is to apply a large anodic potential pulse on the tip leading to (a) defect generation in HOPG and (b) desorbtion of $[PtCl_6]^{2-}$ ions from tip. In the presence of a defect, the relatively large concentration of platinic ions created near the tip apex will lead to Pt deposition. This mechanism is very similar to that for Ag deposition on HOPG [7, 8] and also has some commonality with the mechanism of Pb deposition on Ag [60] (also see section 2.4).
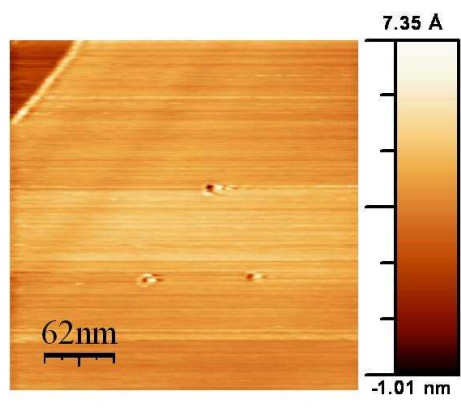
Figure 5.3: Holes formed on HOPG by application of 4.8 V, 0.1 μ by W tip in a solution of $HClO_4$ 0.1 M + H_2PtCl_6 0.5 mM.

Influence of different parameters

In the mechanism described, the pulse is needed to create defects. Defect generation in HOPG has been well investigated [25, 26]. The key point is that in the presence of water, defects can be created by microsecond pulse over a threshold value of ± 4 V. At the threshold voltage domes are formed which are considered intermediaries in the hole formation. In a solution of $HClO_4$ or $H_2PtCl_6 + HClO_4$ holes could be created in the same way (see Fig. 5.3).

Fig. 5.4 shows a series of examples of Pt deposited on HOPG with varying pulse widths. The deposition conditions used are given along with the figures. Pulse width determines the amount of Pt deposited. In $\approx 2\mu$s the reaction is complete as seen from the fact that for 2μs pulse and 5μs pulse, the volume of deposition is similar. For Ag deposition on HOPG, Li et al. [8] use ~ 100 μs pulses and according to their analysis, that is the time required to complete the reaction, although 90% of the reaction is over in $< 10\mu$s. The calculations in section 3.3 on the other hand suggest that reaction occurs much faster(if reaction kinetics is not a limitation); reaction is complete near the tip apex in the sub-μs time scale (see Fig. 5.5). Since even the double layer may not be fully charged at this time scale, a thorough calculation should take into account, electromigration of both metal ions and the supproting electrolyte as well as the reaction kinetics. Another point worth noting is the volume of deposition. For a hemispherical tip of 50 nm radius, and assuming $[PtCl_6]^{2-}$ adsorbed in the same way as on Au(111) [41], there should be a total of ~ 35000 Pt atoms which gives a volume of $\sim 30nm \times 30nm \times 3nm$. The large volume in some cases indicates that Pt and/or Ir from the tip cannot be ruled out.

Not all high voltage pulses create holes. Sometimes deposition occurs without the creation of holes. The high voltage pulses, are then responsible for creation of a large number of very small (< 10 nm) sized particles in a small zone below the tip. Due to their small size, these particles are immobile and can be imaged by the STM (see Fig. 5.6). Fig. 5.7 shows that volume of deposition diminishes with subsequent pulses. In this case the time interval between consecutive pulses is ~ 1 s implying that complete replenishment of $[PtCl_6]^{2-}$ on the
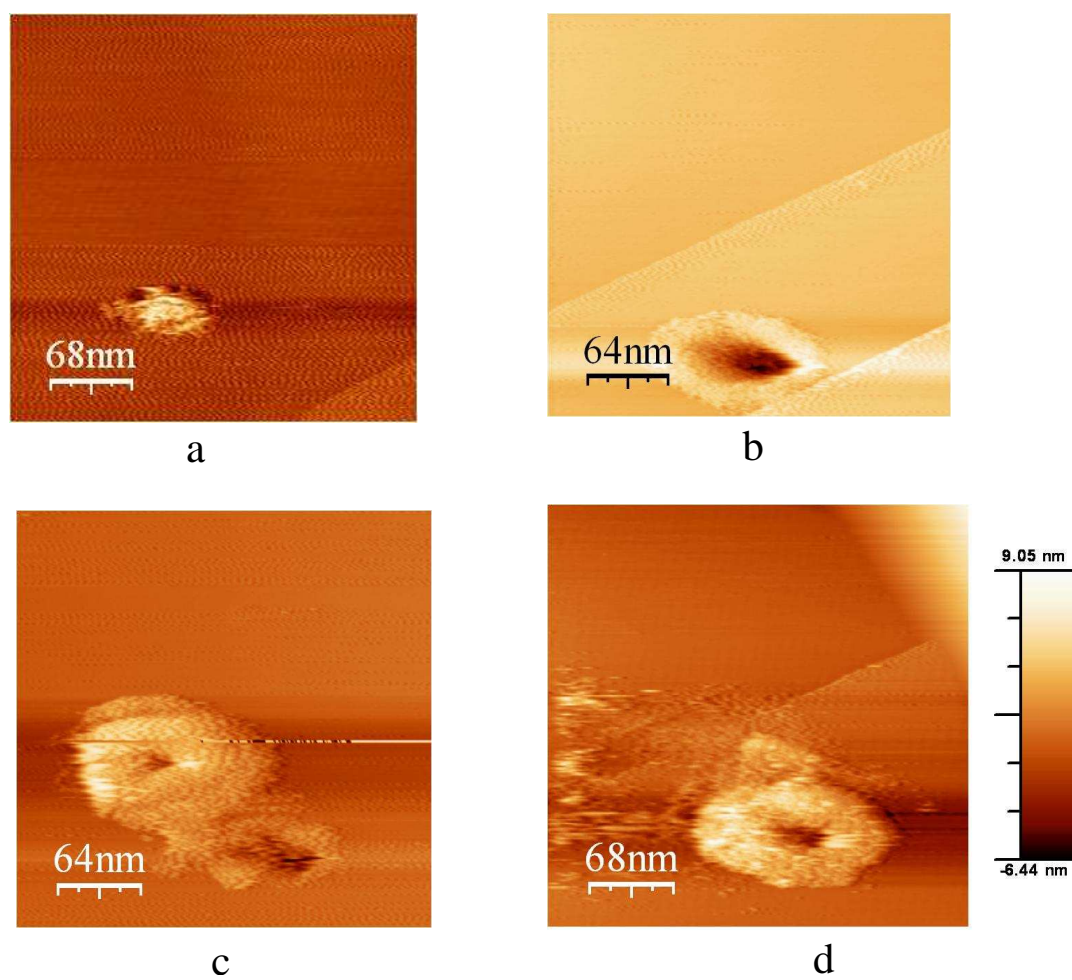
Figure 5.4: Deposition created by applying anodic voltage pulses to PtIr tip. Pulse width is (a) 0.125 μs, (b) 1.25 μs, (c) 2 μs and (d) 5 μs. Rest of the experimental conditions: $g = 6$ Åfrom $I_T = 2$ nA, $\varphi = 6.0$ V and solution - H_2PtCl_6 10 mM + $HClO_4$ 90 mM.
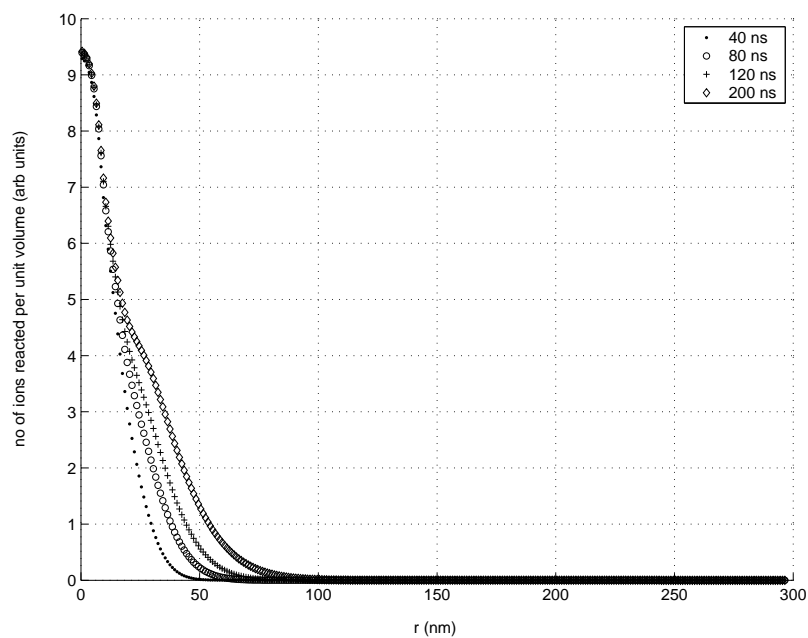
Figure 5.5: Extent of metal deposition as a function of time assuming ions are provided only by the tip and that all ions reaching the substrate react. Simulation conditions – $r_{tip} = 33$ nm, gap $g = 6$ nm, tip angle $\theta = 45°$, diffusion coeff. $D = 10^{-5} cm^2/sec$.
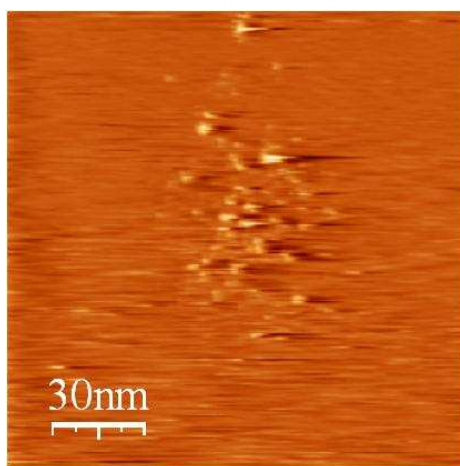
Figure 5.6: Deposition of several 5-10 nm sized particles on HOPG from PtIr tip. Deposition conditions : pulse width 1 μs, $g = 0$ Å from $I_T = 2$ nA, $\varphi = 6.0$ V and solution - H_2PtCl_6 10 mM + $HClO_4$ 90 mM. The larger particles are about 1 nm high.
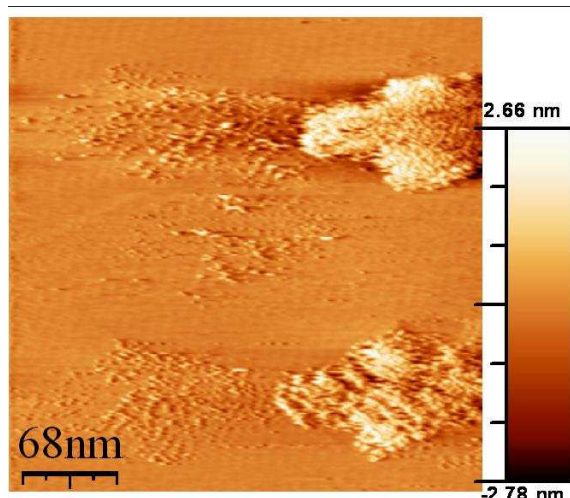
Figure 5.7: Figure illustrating depletion of adsorbed $[PtCl_6]^{2-}$ on the tip. Deposition proceeded cloclwise from upper right corner. The central structure was deposited last. Deposition conditions : pulse width 0.5 μs (corners) and 0.1 μs (centre), $g = 0$ Å from $I_T = 2$ nA, $\varphi = 6.0$ V, solution - H_2PtCl_6 10 mM + $HClO_4$ 90 mM and tip - PtIr.

tip takes several seconds if the tip is maintained at tunneling distances to the substrate. One way to replenish adsorbed $[PtCl_6]^{2-}$ on the tip faster is to retract tip several nanometers away from the substrate. This has been observed. If after several deposition pulses the tip is retracted several 100 nm and reapproached to the substrate the deposition volume increases. If a much higher concentration of H_2PtCl_6 is used, one should expect readsorbtion on the tip is quicker. This is the case as shown in Fig. 5.8 which shows that subsequent deposits (time interval ~1 s) in 0.2 M H_2PtCl_6 solution are nearly the same size. Even in such high concentration, deposition is still restricted to a small zone near the tip apex, showing that deposition occurs from the ions desorbed from the tip and not from ions coming from the solution. Near the tip apex, immediately after application of an anodic pulse on the tip, $[PtCl_6]^{2-}$ ion concentration increases; however further away, electrostatic field pushes $[PtCl_6]^{2-}$ ions away from the substrate surface. At the time scale of $\sim \mu$s, these ions do not yet diffuse back to the surface. This could explain why there is no deposition directly from the solution far away from tip apex. In the case of Ag deposition on HOPG [7, 8] and Pb deposition on Ag [60], pulses ~100 μs are used. Still no deposition is seen far away. It may be due to the low concentration of metal ions used in those experiments.

It is remarked that at potentials ≤ 4 V, there are possibly loose deposits or tip change, due to which imaging becomes very difficult. Experiments with W tips are less repeatable. Tungsten tips oxidize much more readily and are less stable than PtIr tips. Moreover they do not have adsorbed $[PtCl_6]^{2-}$. However as seen in Fig. 5.9 occasionally there are several ≤ 5 nm particles deposited near the hole created by application of anodic pulse on the tip indicating that there is some adsorbtion on the tip.
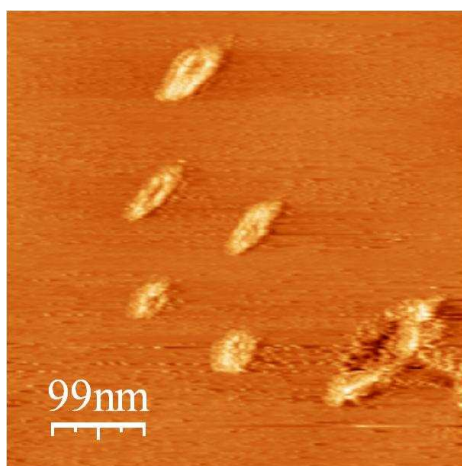
Figure 5.8: Influence of high concentrations of $[PtCl_6]^{2-}$. Replenishment on the tip is considerably faster. Deposition conditions : pulse width 1 μs , $g = 0$ nm from $I_T = 2$ nA, $\varphi = 4.2$ V, solution - H_2PtCl_6 0.5 mM + $HClO_4$ 0.1 M and tip - W.
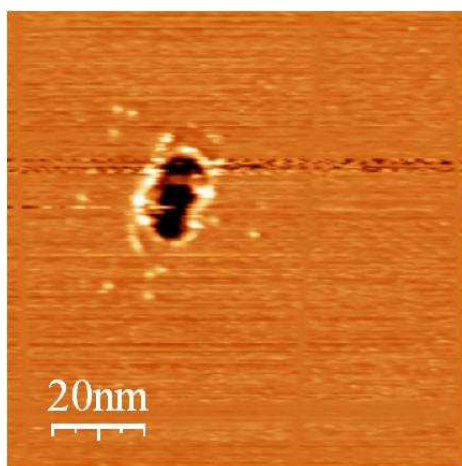
Figure 5.9: With W tips sometimes very small deposits are seen. Deposition conditions : pulse width 1 μs , $g = 2$ nm from $I_T = 2$ nA, $\varphi = 5.0$ V and solution - H_2PtCl_6 0.2 M.

5.4 Summary

A method to deposit Pt from $H_2PtCl_6 + HClO_4$ on HOPG basal plane under an ESTM tip has been described. The depositon works by creation of ∼10 nm sized pits in HOPG and depositing Pt from the $[PtCl_6]^{2-}$ ions that are desorbed from the tip. Anodic voltage pulses on the tip ∼5 V and ∼ 1μs have been used. Two kinds of deposits have been observed – (a) large deposits on holes, ∼50 nm diameter, 2-8 nm high and (b) several ∼10 nm sized particles without the formation of holes. Apparently on this time scale the probability of hole formation is much smaller than one. The mechanism is very similar to that for Ag deposition on HOPG [7, 8]. At tunneling distances between tip and substrate, the time to readsorb $[PtCl_6]^{2-}$ ions onto the tip from the solution can be quite high; consequently the deposition volume decreases with consecutive attempts if the time interval is insufficient. Further investigations are needed to clarify the exact composition of the structures and to understand why there are two different types of depositions under similar conditions.

Chapter 6

Experimental Results – Pt on Au(111)

Platinum catalyzes many technologically important reactions and in order to understand the relationship between the activity and parameters like size and shape, it is desirable to produce nanoparticles of Pt on catalytically inactive substrates. Gold is one such substrate which can be prepared readily with well known surface preparation methods. This chapter describes the deposition of Pt on Au(111) surface induced by the ESTM tip in a solution containing H_2PtCl_6. A new method based on nanosecond pulses is used to create local structures just below the tip. The idea of using nanosecond pulses for nano scale electrochemistry was investigated by Schuster et al. [9]. Nanosecond pulses have been successfully used to etch metals and create sub-μm scale structures [69]. Kirchner et al. [68] have also shown the deposition of Cu on Au(111) with this technique, however using only single pulse for each structure. In this work, as we shall see, this idea is extended to deposit Pt on Au(111) using a train of pulses. The effect of different parameters – voltage amplitude, pulse duration and duty width, tip and concentration are investigated. Structures downto ∼15nm could be created repeatably by this method.

6.1   Background

Uosaki et al. [115] studied growth of Pt on Au(111) from H_2PtCl_6 and Waibel et al. [41] have studied the initial stages of Pt deposition from K_2PtCl_4 and K_2PtCl_6 on unreconstructed Au(111) and Au(100). Some points from their work are worth noting here. At or slightly above the Nernst potential for $Pt/[PtCl_4]^{2-}$ the surface reconstruction for gold is lifted by anion adsorption and the emerging gold islands are partially removed by electrochemical annealing. High resolution STM images on Au(111) at these potentials showed an ordered structure with next neighbour distance ∼0.72 nm and a hexagonal arrangement which was assigned to the $[PtCl_4]^{2-}$ adlayer. Individual $[PtCl_4]^{2-}$ were resolved in the form of pinwheels on Au(100). Due to the stability of the adsorbed $[PtCl_4]^{2-}$ complexes, deposition starts at high overpotential (200mV). Once Pt deposition has started, the overpotential for further deposition is markedly reduced. Deposition of Pt starts at defects like step edges and

holes in the surface or domain boundaries of the adlayer. At higher overpotentials nucleation also takes place on the terraces. Deposition continues via 3-d growth which is also expected due to higher surface energy of Pt compared to Au (Pt: 2.691 J m^{-2}, Au: 1.626 Jm^{-2} [116]). Deposition from $[PtCl_6]^{2-}$ shows the same behaviour which is also expected because deposition occurs from $[PtCl_4]^{2-}$ in both cases; $[PtCl_6]^{2-}$ is not stable at the Pt deposition potentials. In contrast to the work of Waibel et al. [41], Uosaki et al. [115] found epitaxial growth where Pt(111) is formed on Au(111) with the $[PtCl_6]^{2-}$ adlayer on top possibly due to the higher overpotential that they applied.

6.2   Experimental

Gold on mica samples, 1.4 cm×1.1 cm with 150 nm thickness, from SPI$^{®}$ were used for the experiments. Atomically flat terraces were normally found to be few hundred nanometers in size. Some experiments were also done on gold single crystal(8mm diameter × 1 mm thickness, polished downto 0.03μm, orientation accuracy < 1°, MaTecK, Germany). Normally the substrates were flame annealed with a butane-propane flame to increase the size of the terraces. Electrolytes were prepared from $HClO_4$ (Merck, suprapur), Milli-Q water and H_2PtCl_6 (8 wt. % solution in water, Sigma-Aldrich). All measurements were done with home built electrolytical STM. For nanosecond pulses, Avtech AVPP–1–C pulse generator (from Avtech Electrosystems Ltd., Canada) was used. Experiments were done in two electrode setup (no potentiostatic control).

Flame annealing

Flame annealing is a technique used to prepare clean and well-ordered metal surfaces. Developed by Clavilier et al. [117], it was first demonstrated for platinum. The method consists of annealing a polished monocrystal in a hydrogen flame at about 1000°Cfor several minutes. Earlier Bunsen burners were also used for annealing and there are also reports of propane-butane flame being used. The initial recipe involved rapid quenching of the hot crystal in pure water which was later revised in order to avoid gradual destruction of bulk crystallinity due to the heat shock [118] and to fully retain the surface reconstruction in the case of gold [119]. The method is most commonly used for platinum and gold but has also been used on other metals [120]. For gold on mica, the procedure is to bring the flame tip to the gold film at about a 30 degree angle and sweep back and forth (at approx. 1 Hz freq.) for 30 to 60 seconds, keeping the small flame spot on the film a dim orange color. The single crystals are usually heated at yellow heat for several minutes. Fig. 6.1 shows the surface Au(111) after flame annealing with a propane-butane flame for ∼20 minutes.
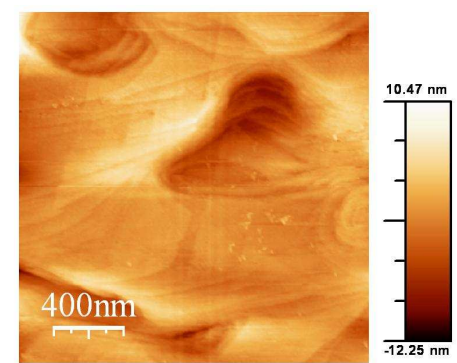
Figure 6.1: STM image of Au(111) surface after flame annealing for 20 minutes at bright orange heat. Electrolyte: H_2PtCl_6 0.1M, tip: PtIr, U_{tip}=0.05 V, U_{sample}=0.0V

6.3 Results and Discussion

Setup and Methodology

Due to the use of a two electrode system, one of which is the STM tip, and by keeping the Faraidaic current < 0.1 nA, we ensure that the substrate/electrolyte is at the Nernst or equilibrium potential. This means that the Au(111) surface is unreconstructed and that there is an adlayer of $[PtCl_6]^{2-}$. The tip/electrolyte potential is also maintained near the Nernst potential by ensuring Faraidaic current is zero (see Fig. 6.2). Unless otherwise mentioned, experiments have been done with PtIr tips (PicoTips, Molecular Imaging). The idea used for Pt deposition is that by applying short pulses when the tip is in close proximity to the surface, the adsorbed $[PtCl_6]^{2-}$ on Au(111) surface convert to Pt only in a region near the tip apex upto which the double layers have been sufficiently charged. Further it is expected that these Pt atoms diffuse and to form stable clusters, ions from the solution are allowed to be readsorbed on Au(111) and to form Pt repeatedly for a certain number of times. The idea is shown schematically in Fig. 6.3.

The setup for the nanosecond pulses is shown in Fig. 7.1. It is remarked that in the presence of the tunneling current amplifier, which has limited bandwidth (∼1 kHz), the potential difference between the tip and substrate can not be modified at time scales much smaller than a millisecond. To overcome this problem, a switch is positioned as shown, which switches the circuit from normal tunneling mode to pulsing mode. During the switching period, it is possible that we have open circuit for a few milliseconds. Given that the system is maintained at equilibrium this should not cause any concerns. The deposition procedure is as follows : (1) make an initial scan of the region; (2) position the tip over the predefined spot at a gap Δz; (3) apply a train of pulses as shown in Fig. 6.4; (4) move to next spot and repeat the procedure; (5) make a final scan of the region.
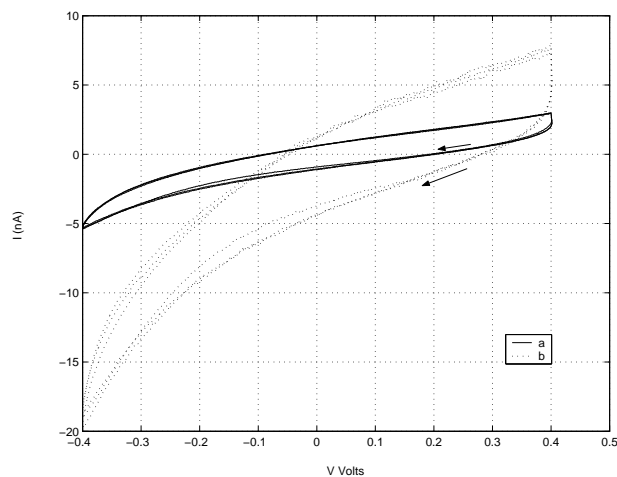
Figure 6.2: Current voltage characteristic in two electrode configuration for two PtIr tips (a) and (b) in 0.1 M H_2PtCl_6 at a scan rate of 0.4 V/sec.
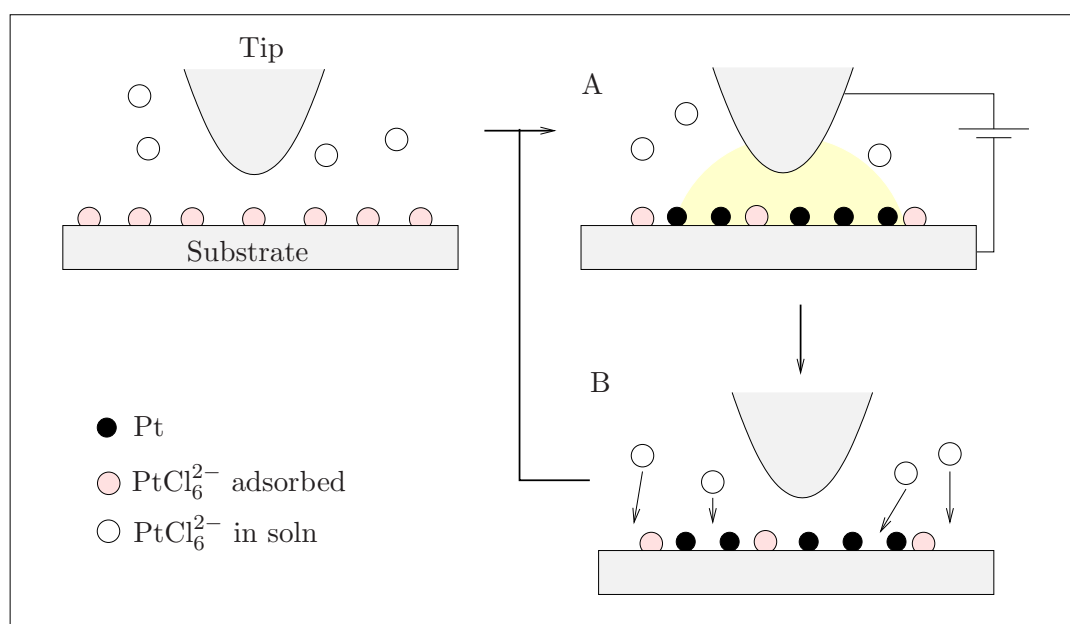
Figure 6.3: Schematic representation of the method of deposition. A: deposition of Pt. B: readsorbtion of $[PtCl_6]^{2-}$ ions on substrate. Deposition is limited to a zone determined by the pulse width.
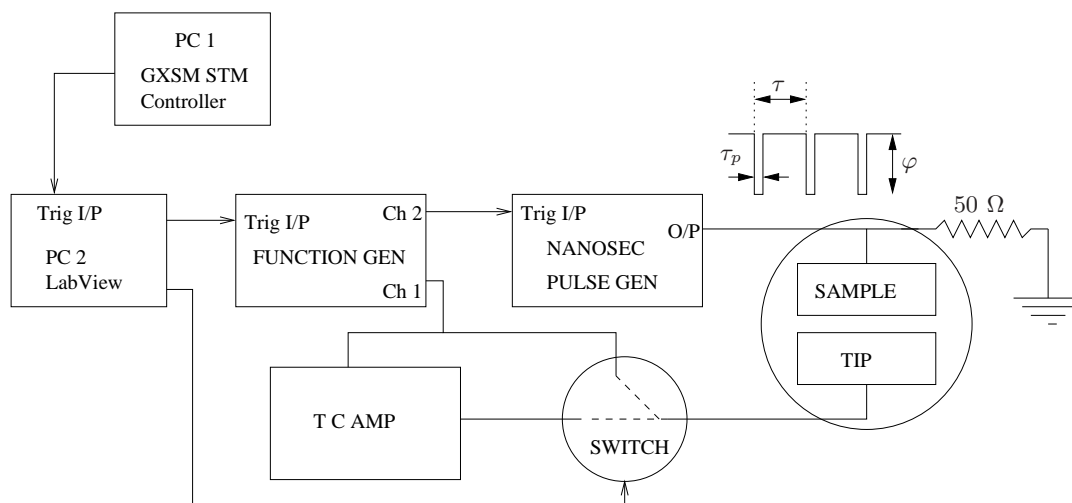
Figure 6.4: Setup of the experiment for deposition by nanosecond pulses. The pulse parameters are also shown.

Influence of different parameters

The control parameters for the deposition are :
  * Pulse amplitude
  * Pulse width
  * Pulse period
  * Number of pulses
  * Tip-sample gap

From the discussion in section 3.3, one expects that pulse width should have the largest influence in determining the size of the clusters. Pulse period is important for replenishing ions in the tip sample gap and for readsorbtion on the surface. During the replenishment part of the pulse cycle, Pt on the surface can diffuse outwards. The time of replensihment and the number of Pt atoms will determine the formation of stable clusters.

The tip geometry and material also has an influence on the deposition. For the normal tip dimensions (∼10s nm diameter) and for electrolyte concentrations ∼0.1 M, as was seen in section 3.3, the tip to sample gap in the nanometer range has no significant influence.

Potential

Theory of metal deposition shows that defects and step edges are preferential sites for deposition. Waibel et al. [41] also showed that in the case of Pt deposition on Au(111), deposition starts at step edges and when the deposition overpotential is increased, there is deposition on the terraces too. For the localized deposition with an ESTM, this is visible in Fig. 6.5. Under the experimental conditions – τ_p 0.1μs, τ 100 μs, no. of pulses 100, g 7 nm from $I_T = 2$ nA and solution - H_2PtCl_6 0.1 M – for $\varphi = 2$ V there is deposition only at the step edges, while for $\varphi = 2.5$ V there is deposition also on the terraces.
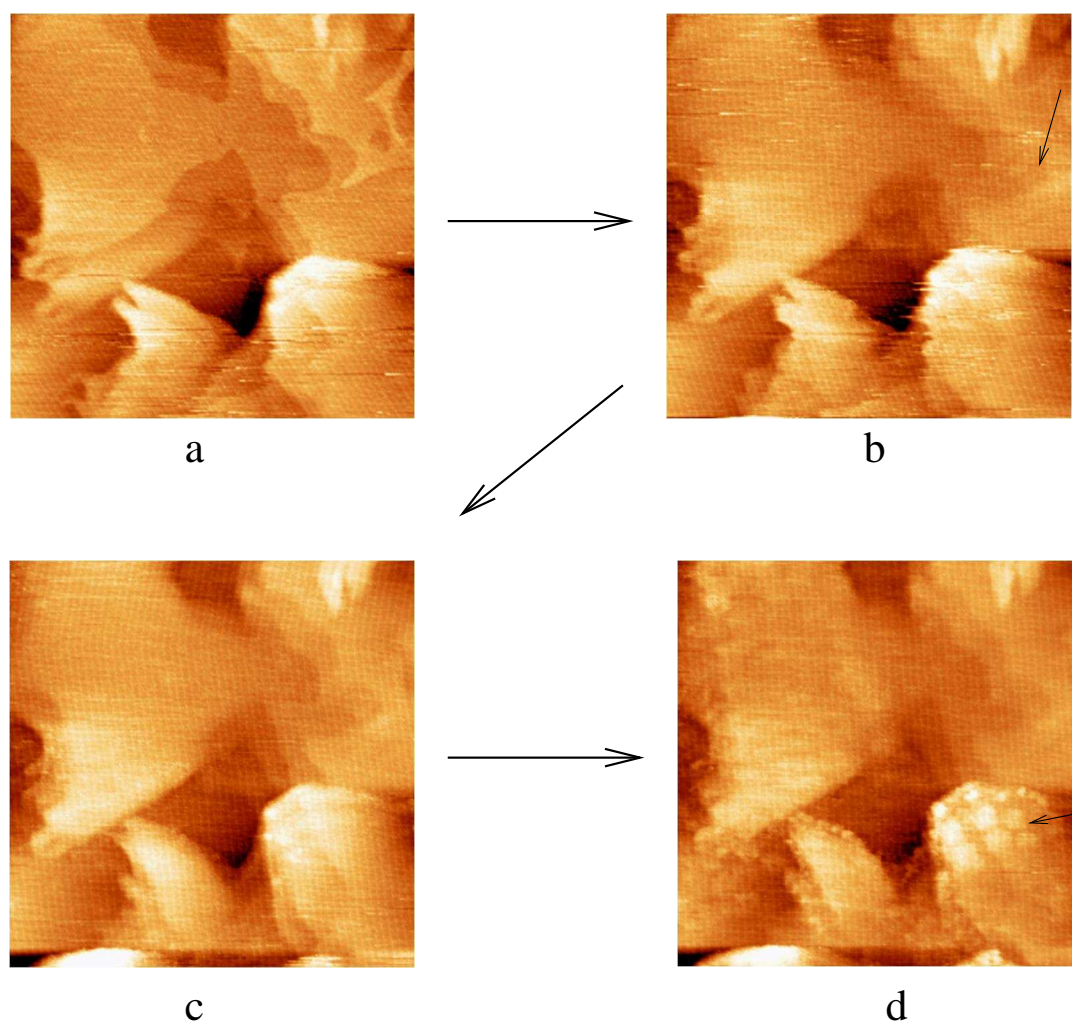
Figure 6.5: Effect of pulse potential amplitude. Pulse parameters: a to b & b to c : $\varphi = 2$ V; c to d : $\varphi = 2.5$ V. Rest of the conditions: τ_p 0.1μs, τ 100 μs, no. of pulses 100, g 7 nm from $I_T = 2$ nA and solution - H_2PtCl_6 0.1 M. Images are 350 nm × 350 nm. Arrows show regions where there are changes.

Pulse parameters

The influence of pulse width is shown in Fig. 6.6. Experimental conditions – τ 100 μs, no. of pulses 100, g 4 nm from $I_T = 2$ nA and solution - H_2PtCl_6 0.2 M. For $\tau_p = 10$ ns to 30 ns the diameter of the deposit is $\sim$50 nm although the deposition is mostly in form of a few closely spaced clusters of size $\sim$10 nm each. Clusters are 1 to 2 monolayers high. For $\tau_p = 40$ ns, there are many more clusters and the overall size is close to $\sim$75 nm. Closer inspection of the image shows that there are also deposits in a more extended region. For $\tau_p = 60$ ns, deposition area > 150 nm. The growth of the deposition diameter with pulse width is consistent with the results in section 3.3 (see Fig. 6.7). In the section 3.4, for a similar system, if the number of metal atoms is high enough, usually a large cluster along with many very small clusters are found to be formed. This contrasts with the fact that here we see a few relatively large clusters. It should however be noted that the Monte Carlo simulation time scale in section 3.3 is much much smaller than the STM observation time scale. On the observation time scale, smaller clusters can be expected to diffuse/disintegrate while even large clusters can divide at the weak links.

In Fig. 6.6 it is seen that from $\tau_p = 10$ ns to 30 ns the deposition diameter and volume does not change. The model of double layer charging at low voltages shows such effect (see Fig. 6.7) where the radius to which the double layer is charged increases rapidly beyond certain pulse width. At high voltage difference between the electrodes, the number of ions in the tip-sample gap maybe insufficient to fully charge the double layer capacitor. This will also have some consequence on the deposition diameter and volume. This aspect needs further investigation.

Pulse period of $\sim 100\mu$s has been found experimentally to work well. From the calculations of diffusion under tip to replenish the ions in the tip-sample gap (section 3.3), this time scale can be expected for blunt tips, which is often believed to be the case with PtIr tips. In an extreme case (see Fig. 6.8) when $\tau \sim 1\mu$s, it is most likely that material from tip has been removed oxidatively leading to the formation of 'multiple' tips. Deposition directly from the tip has been suggested in other systems [60]. The presence of the adsorbed layer probably shifts the oxidation potential of Pt (more precisely PtIr) to more positive values, so that in its absence a smaller positive potential on the tip can oxidatively remove Pt (and/or Ir).

The pulse period is the time for the substrate to readsorb $[PtCl_6]^{2-}$ ($\tau_p \ll \tau$). Allowing complete readsorbtion, number of pulses allows us to estimate the total number of Pt atoms formed on the substrate in the reaction zone. A certain minimum number of atoms is needed to form stable clusters. In the experiments, it is found that n$\sim$100 is sufficient while at n$\sim$10 no deposition is observed at least at a resolution of about 1 nm. From surface adsorbed $[PtCl_6]^{2-}$, one gets 1 atom per $0.72^2\sqrt{3}/2$ nm^2 [41], while for a Pt lattice one needs 1 atom per $0.4^2\sqrt{3}/2$ nm^2. In the absence of any mechanism by which Pt atoms are lost after forming near the tip apex, number of pulses needed to form 2-d Pt cluster is $(0.72/0.4)^2 = 3.24$. Infact from section 3.4, the requirement to form large (and hence stable) cluster is $(n/\sigma^2)_{crit} \approx 1.5 \Rightarrow 0.41$ atom per $0.4^2\sqrt{3}/2$ nm^2, which gives the required number of pulses = $3.24 \times 0.41 = 1.33$. This is a strong indication that at the time scale of 100μs, surface diffusion of Pt is significant.
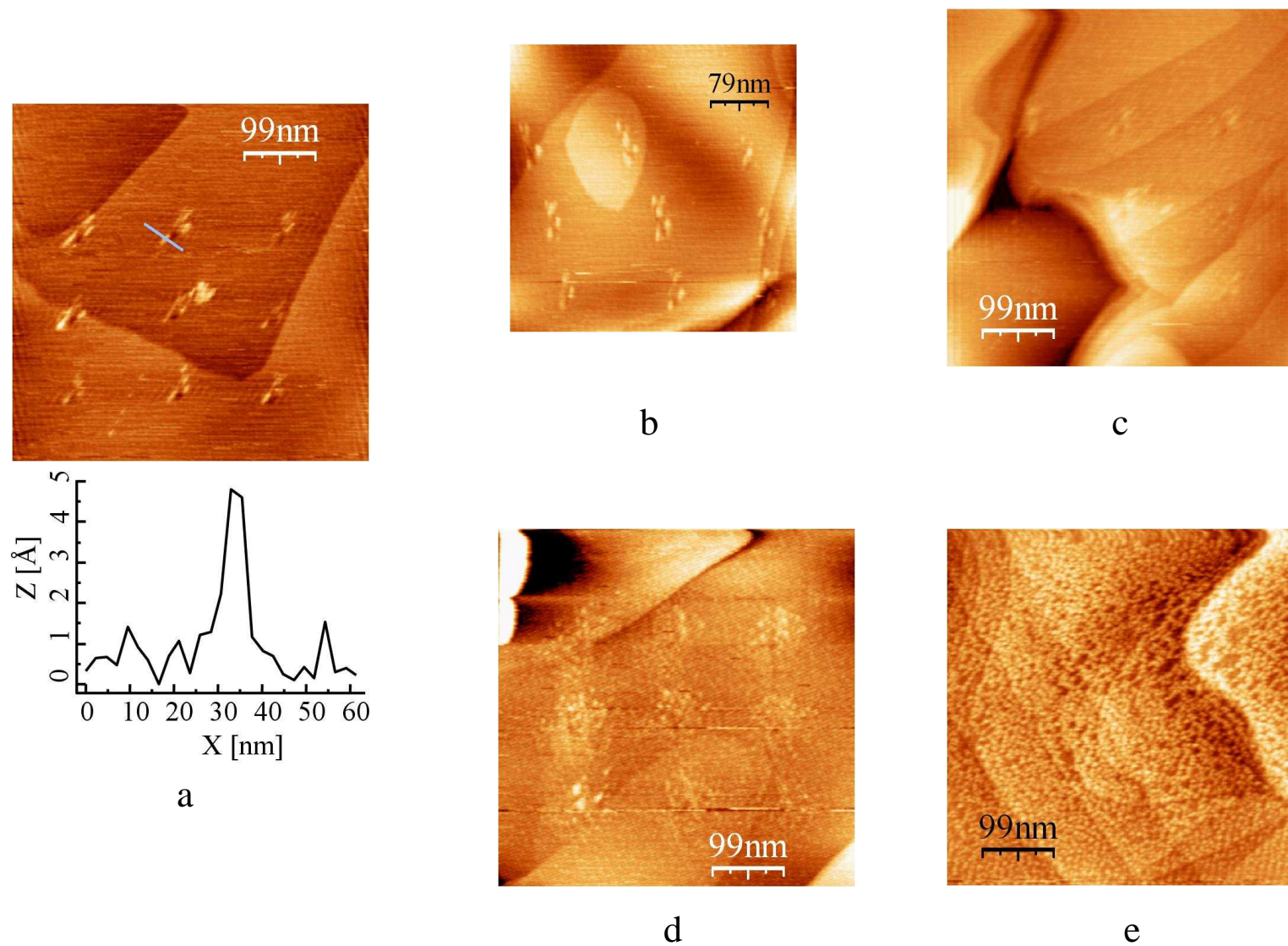
Figure 6.6: Influence of pulse width on Pt deposition. τ_p (a) 10 ns, (b) 20 ns, (c) 30 ns, (d) 40 ns and (e) 60 ns. Rest of the conditions: τ 100 μs, no. of pulses 100, g 4 nm from $I_T = 2$ nA, $\varphi = 3.0$ V and solution - H_2PtCl_6 0.2 M. The profile of a deposited structure is shown in (a). In each case an array of 3×3 deposits was attempted.
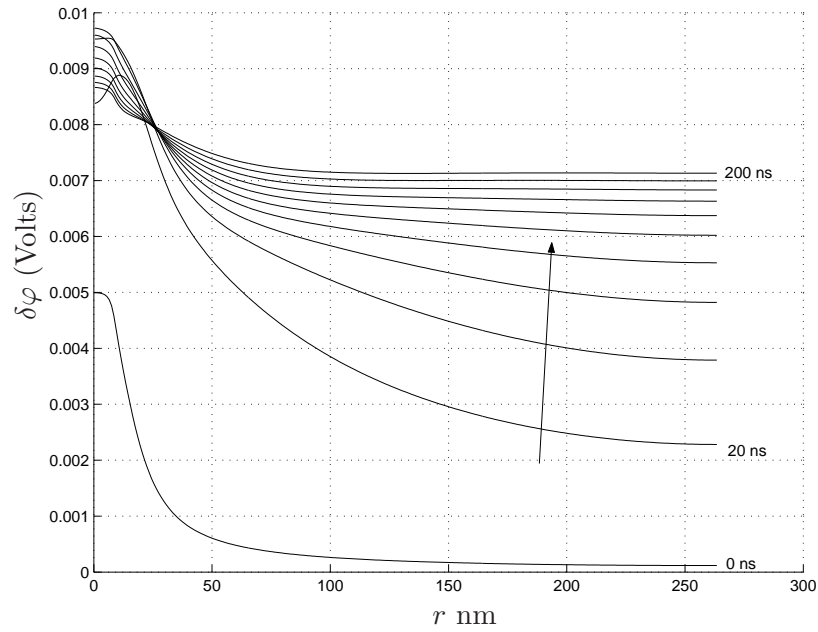
Figure 6.7: Double layer charging as a function of time. Potential drop across $\Delta z = 1$ nm on the sample surface at different times. Simulation conditions – $r_{tip} = 33$ nm, gap $g = 4$ nm, tip angle $\theta = 45°$, 1:1 electrolyte with $q = 1$, concentration 0.1 M, diffusion coeff. $D = 10^{-5} cm^2/sec$, $\varphi_{tip} = 0.01$ V and $\varphi_{sample} = -0.01$ V. Arrow shows increasing time; time interval between consecutive curves = 20 ns.
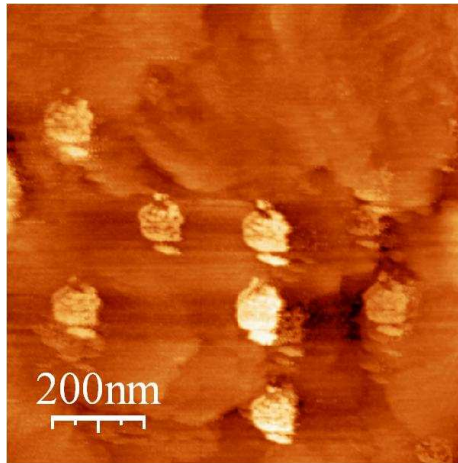
Figure 6.8: Deposition with very small τ, $\tau = 0.2$ μs . Experimental conditions τ_p 0.1μs, no. of pulses 100, g 4 nm from $I_T = 2$ nA, $\varphi = 4.0$ V and solution - $H_2 PtCl_6$ 0.1 M. An array of 4×4 deposits was attempted.
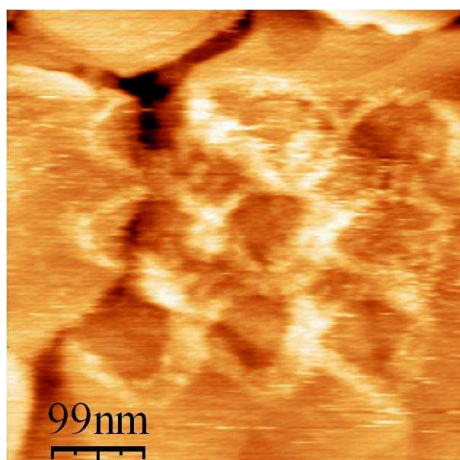
Figure 6.9: Effect of tip geometry. Experimental conditions τ_p 0.1μs, no. of pulses 100, g 4 nm from $I_T = 2$ nA, $\varphi = 4.0$ V and solution - H_2PtCl_6 0.2 M. An array of 3×3 deposits was attempted.

Tip effects

Extremely blunt tips will not allow diffusion to the tip-sample gap. Such a case is seen in Fig. 6.9. The ring-like deposition suggests a tip diameter of $\sim$ 100 nm but with an unusually flat end. Etched W tips have been used occasionally. Under similar conditions, in the case of W tips, there are often random deposits, characteristically different from those shown in Fig. 6.6, which may be attributed to material from tip. W tips are also more prone to oxidation and become unstable after several pulses.

Source of Pt ions

There are three possible sources of $[PtCl_6]^{2-}$ ions – (a) adsorbed $[PtCl_6]^{2-}$ on Au(111) surface, (b) adsorbed $[PtCl_6]^{2-}$ on tip surface and (c) from the solution. If the Pt deposited on the substrate was supplied only by the tip, then there would be a characteristic difference in the deposition size versus pulse width. As is seen in section 3.3, Fig. 3.23(b), or from the studies of Pt deposition on HOPG, the deposition in this case would be restricted to a small zone even if the pulse width is $\approx 1\mu$s. In contrast Pt is deposited over $\approx 1\mu$m region if the pulse width is 1μs. This rules out that the tip alone is contributing the Pt ions. Upon application of a cathodic potential on the substrate, during the double-layer charging phase, the free $[PtCl_6]^{2-}$ ions in the solution are pushed away from the substrate surface. Actually there are two competing factors - electromigration, pushing $[PtCl_6]^{2-}$ ions away from the substrate and diffusion which tries to reestablish $[PtCl_6]^{2-}$ near the substrate. During the charging phase, electromigration will dominate. The above arguments strengthen the hypothesis that Pt deposition occurs from the adsorbed $[PtCl_6]^{2-}$ on Au(111).

6.4 Tip induced surface reconstruction

At substrate potentials more positive than the Nernst potential, $[PtCl_6]^{2-}$ ions are desorbed from the surface. In this potential region, normally Au(111) surface reconstruction will be lifted and a large number of monolayer high islands will be formed []. When the potential is brought back to the Nernst potential, $[PtCl_6]^{2-}$ ions are reabsorbed leading to a flat surface. This phenomenon can be induced by the tip by applying a substrate-positive pulse. If islands have formed over several 100 nm, then under the tip, the readsorbtion of $[PtCl_6]^{2-}$ ions occurs at the time scale of seconds. This could be observed with the STM tip. Fig. 6.10 shows the islands disappearing during a scan after they were formed under conditions given in the caption. This reinforces the hypothesis that Pt deposition by the method discussed occurs from surface adsorbed anions. It also gives an idea of the time involved for ions to diffuse into the tip-sample gap.
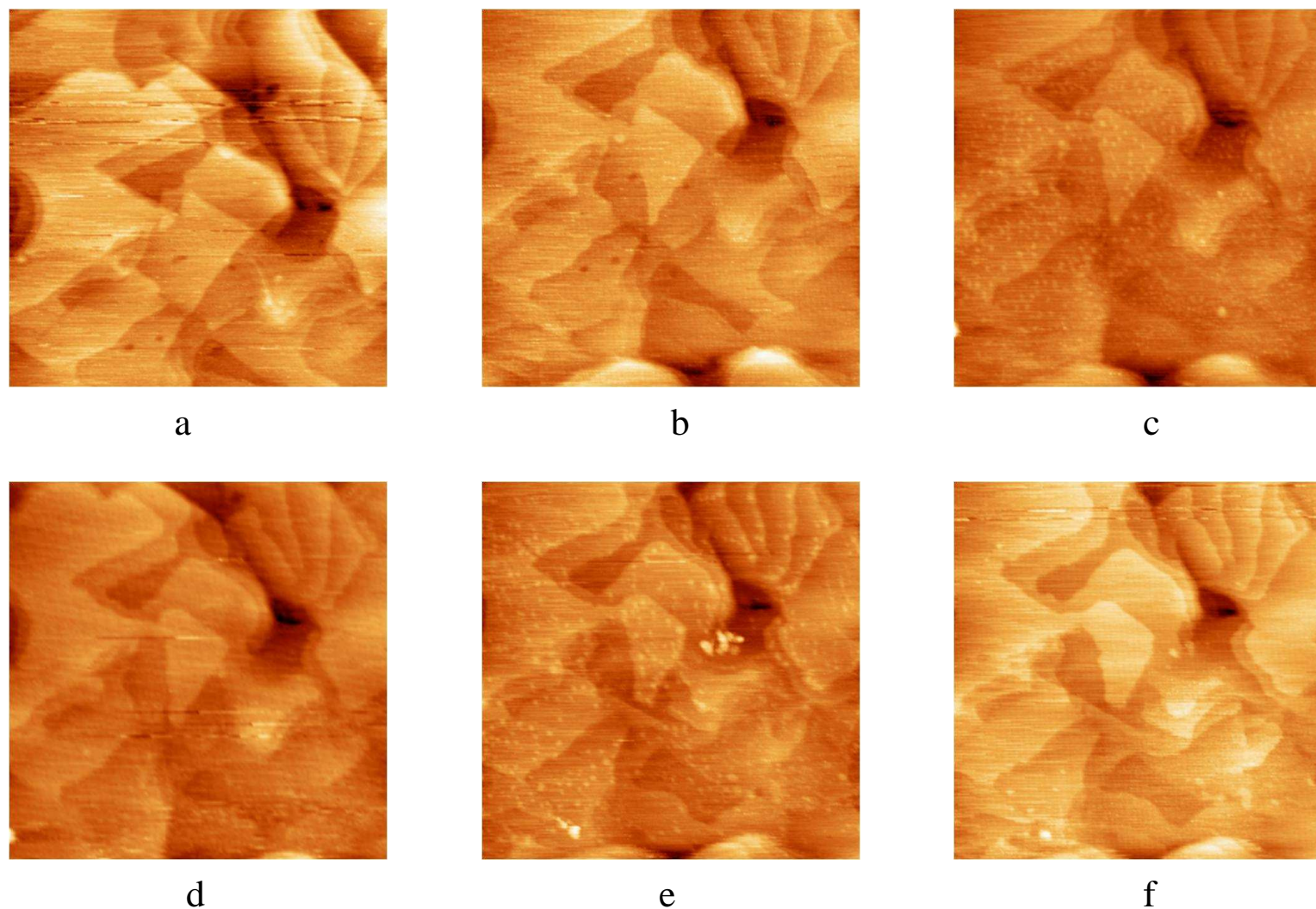
Figure 6.10: Tip induced surface reconstruction. All scans are 350 nm × 350 nm. Imaging condiitons: Tip - PtIr, solution - H_2PtCl_6 0.1 M, $\varphi_{tip} = 0.05$V, $\varphi_{sample} = 0.0$V. Going from **a** to **b** voltage pulses are applied while tip is positioned at centre. Pulse parameters: τ_p 1μs, $\tau = 100$ μs, no. of pulses 100, g 7 nm from $I_T = 2$ nA, $\varphi_{sample} = 2.0$ V. **b** to **c** : $\varphi_{sample} = 3.0$ V and other parameters are same. **c** to **d** : time gap of several seconds. **d** to **e** – voltage pulses as from (b) to (c). **e** to **f** : time gap of several seconds.

6.5 Summary

A method to create Pt clusters by an ESTM locally on Au(111) surface has been described. Clusters of $\sim$10 nm and 1-2 monolayers high can be created from the adsorbed $[PtCl_6]^{2-}$ ions (adsorbed on Au(111)) by applying a train of sub-microsecond voltage pulses between tip and surface. The clusters can be localized within $\sim$50 nm diameter. The deposition procedure uses the idea of electrochemistry by ultra-short voltage pulses and builds on it to use a train of pulses. The pulse parameters – pulse width, pulse period and number of cycles – play key roles in the deposition process. While their effects are interconnected, as a general rule – pulse width is responsible for the deposition size, pulse period is important for replenishment of ions and a critical number of cycles is needed to create stable clusters. The experimental results are more or less consistent with the discussion in Chapter 3. Finally the deposition procedure appears quite universal and should be applicable to many more systems.

Chapter 7

Nanoparticles by Electrochemical Discharges

In the preceeding chapters nanoparticles were formed locally under an ESTM tip. If the tip is replaced by a thin wire and a very high electric potential is applied, electrochemical discharges can be created. This chapter presents a novel method based on electrochemical discharges to produce metal nano-particles in large quantities. In an aqueous electrolyte containing metal ions, large cathodic potential is applied to the working electrode or tip. Large current densities ($j \sim 1\text{A/mm}^2$ at $V \sim 20$ V) lead to the formation of a gas film around the electrode. Electrical discharges are created across the film which leads to the formation of metal nano clusters (typically 10-150 nm). The gas film prohibits the metal to deposit on the electrode. The method has been used to produce nano particles of copper, platinum and gold.

7.1   Electrochemical discharges

Electrochemical discharge phenomena are already known since the work of Fizeau and Foucault [121] in 1844. This phenomenon is known in the field of electrochemistry under the keywords *electrode effects* and *contact glow discharge electrolysis*. Electrode effects has implications in the aluminium production by *Hall-Heroult process* and is therefore widely debated in literature. Systematic studies have been carried out by Guilpin and Garbaz-Olivier [122] and more recently by Vogt [123] and Wüthrich et al. [10]. The phenomenon has also found extensive usage for machining of glass and other non-conducting materials where the process is known as SACE - Spark Assisted Chemical Engraving [124, 125, 126, 127, 128].

The starting point for understanding the phenomenon is the steady state *I-V* (current-voltage) characteristics for a two electrode system in aqueous electrolyte. A schematic of the setup is shown in Fig. 7.1. For the situation where the counter electrode is very large compared to the working electrode, a typical curve is shown in Fig. 7.2. It is remarked that the current at a fixed voltage, shown in the *I-V* curve, is a mean current due to the random (stochastic) evolution of bubbles around the electrode. Furthermore it is the steady-state current i.e. current after the *bubble layer* is completely formed. (The growing and
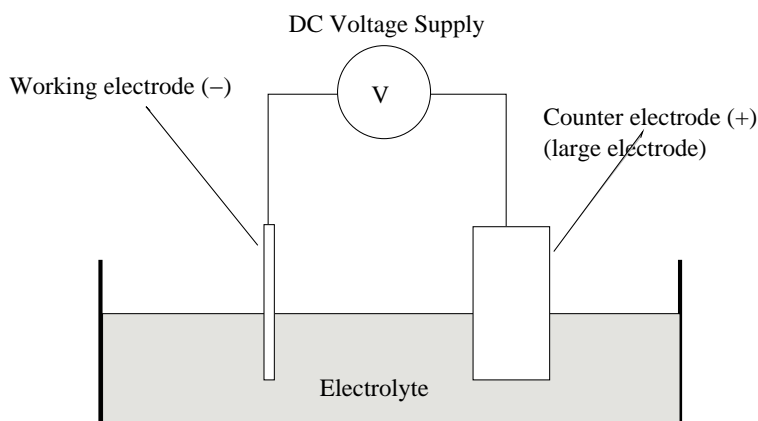
Figure 7.1: Schematic of the setup for producing electrochemical discharges

detached bubbles around the electrode during electrolysis form the *bubble layer*. It consists of an *adherence region* where bubbles are adhered to the electrode surface, a *bubble diffusion region* where the bubble concentration is very high and size a few mm and finally the *bulk region* where bubbles are quite dispersed [129, 130]). Following the description of Fascio [131] and Wüthrich [132], the curve is divided into five regions.

Thermodynamic and Overpotential region

For voltages smaller than the *decomposition potential* V_d no electrolysis happens and no current flows in the system. Typically $V_d \simeq 2$ V.

Ohmic region

In region AB of Fig. 7.2, the mean current I increases nearly linearly with the voltage V and therefore this region is termed the *ohmic region*. The typical voltage in this region is from 2 to 10-12 V. Bubbles are evolving around the working electrode and the bubble layer is relatively compact with the typical size being 1-5 mm. All bubbles have similar diameter of about 100μm. The resistance measured in this range is inversely proportional to the electrode immersion depth and very close to the electrolyte resistance [131].

Limiting Current Region

In the third region, BC of Fig. 7.2, the mean current I reaches a limiting value and is nearly constant. Photographs of the electrode in this region show that both small bubbles (as seen in AB) and large bubbles (typically 300 - 700μm [131]) are formed. Bubble coalescence becomes important in this region. The typical size of the bubble layer is similar to that in the region AB. The temperature of the electrolyte also increases.

This region ends in a critical point C of Fig. 7.2. The critical point is characterized by a a critical voltage V_{crit} and a critical current I_{crit}. Beyond this point, the current decreases
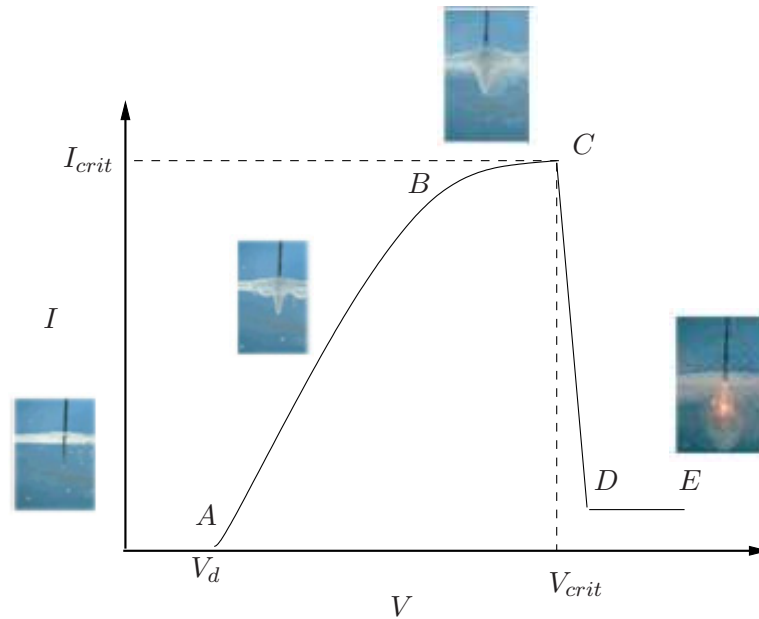
Figure 7.2: Typical static current-voltage *I-V* curve for an electrode in aqueous electrolyte. The photographs show the bubble formation in different regions of the curve. Sparks occur in the region DE. Adapted from reference [131]

severely and almost instantly. Wüthrich [132] elaborates on the point C and considers the transition from BC to CD as a *phase transition*.

Instability Region

In region CD, the mean current drops sharply, electrolyte resistance diverges and a *gas film* is formed around the working electrode. This region is called by Wüthrich et al. [10] the *instability region* because the system can fluctuate between the limiting current region BC and the spark region DE.

Spark Region

In the last region, DE, a gas film is considered to envelop the electrode, completely insulating it from the electrolyte. The mean current is very small (in the mA range). Current in this region occurs as a sequence of very short pulses (a few 100 μs with an amplitude up to 1 A) accompanied by emission of light - hence the name spark region. These discharges are well known *non self sustained arc discharges* [132].

7.2 Stochastic model

Wüthrich [132] has developed a stochastic model to explain the phenomenon of electrochemical discharges. The key points of his model are presented here.
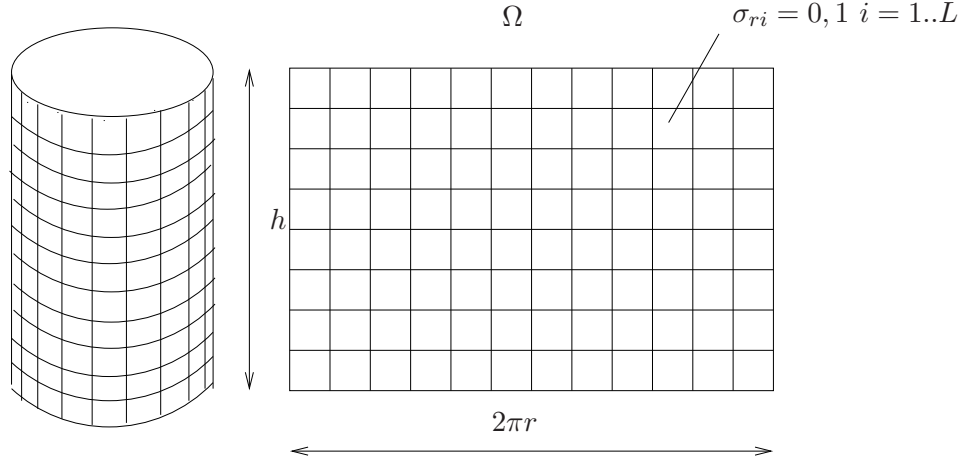
Figure 7.3: Electrode surface Ω is divided into square lattice for the stochastic model. Adapted from reference [132].

The working electrode is divided into a regular lattice of L sites (see Fig. 7.3) and a function σ_{ri} is defined for the ith site where $\sigma_{ri} = 0$ if no bubble is present at site i and $\sigma_{ri} = 1$ if a bubble is growing at that site. For each site i the *probability of occupation* $P_i(t)$ by a bubble at time t can be defined by computing the mean of $\sigma_{ri}(t)$ over N micro-configurations:

$$P_i(t) = \langle \sigma_{ri} \rangle = \frac{1}{N} \sum_{r=1}^{N} \sigma_{ri}(t) \tag{7.1}$$

The *conditional probability* $P(\sigma_{ri}, t \mid \sigma'_{ri}, t')$ that the site i is in the state σ_{ri} at time t, knowing that at time t' it was in the state σ'_{ri} is defined through the relation

$$P_i(\sigma_{ri}, t) = \sum_{j=0}^{1} P(\sigma_{ri}, t \mid \sigma'_{ri} = j, t') P_i(\sigma'_{ri} = j, t') \tag{7.2}$$

The *mean bubble coverage fraction* Θ of the electrode is computed by:

$$\Theta(t) = \langle \Theta_r(t) \rangle = \frac{1}{N} \sum_{r=1}^{N} \Theta_r(t) \tag{7.3}$$

The dynamics of the system are given by the transition between an occupied state $\sigma_{ri} = 1$ and an empty state $\sigma_{ri} = 0$. Two transition probabilities are defined (see Fig. 7.4): (i) η from occupied to empty state is the probability that a growing bubble is detached per unit of time and (ii) λ from an empty to an occupied state is the probability that a bubble is growing on the tool on the site i per unit time. η and λ have been estimated as

$$\eta = \eta_0 \cdot j^m \tag{7.4}$$

$$\lambda = \lambda_0 \cdot j \cdot (V - V_d) \tag{7.5}$$

Figure 7.4: Transition probabilities λ and η. Adapted from reference [132].

where j is the local current density, V is the applied potential, V_d is the water decomposition potential, η_0, λ_0 are constants that depend on electrolyte conductivity, electrode geometry and the electrode surface roughness. $m = 1$ for high current densities.

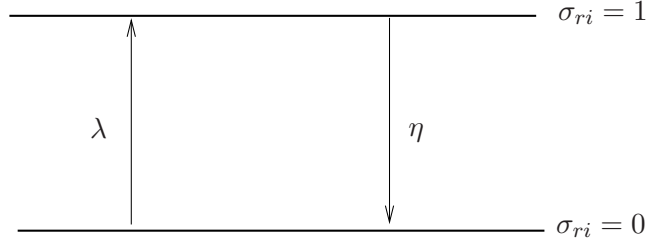Time evolution of the conditional probabilities are given by the following $2L$ *master equations*:

$$\partial_t P_i(\sigma_{ri} = 1, t \mid \sigma'_{ri}, t_0) = -\eta P_i(\sigma_{ri} = 1, t \mid \sigma'_{ri}, t_0) + \lambda P_i(\sigma_{ri} = 0, t \mid \sigma'_{ri}, t_0) \tag{7.6}$$

$$\partial_t P_i(\sigma_{ri} = 0, t \mid \sigma'_{ri}, t_0) = -\lambda P_i(\sigma_{ri} = 0, t \mid \sigma'_{ri}, t_0) + \eta P_i(\sigma_{ri} = 1, t \mid \sigma'_{ri}, t_0) \tag{7.7}$$

This kind of master equation is known as the *telegraph noise equation*. The mean coverage fraction Θ is calculated as:

$$\Theta(t) = \frac{1}{L} \sum_{i=1}^{L} \sum_{j=0}^{1} P_i(\sigma_{ri} = 1, t \mid \sigma'_{ri}, t_0) P_i(\sigma'_{ri} = j, t_0) \tag{7.8}$$

For the stationary case Θ and its fluctuations $\Delta\Theta$ are given by:

$$\Theta = \frac{\lambda}{\eta + \lambda} \tag{7.9}$$

$$\Delta\Theta = \frac{\sqrt{\lambda\eta}}{\eta + \lambda} \tag{7.10}$$

The central result is that in the stationary case when $\Theta = 0.5$, $\Delta\Theta = 0.5$ too. This is significative of a phase transition. What it means is that $\Theta = 0.5$ is a critical point when the entire electrode may be covered by bubbles leading to a sharp drop in current.

Wüthrich [132] further improved upon his model using percolation theory. Percolation theory deals with the effect of varying the richness of interconnections present in a random system. The basic idea is the existence of a sharp transition at which the long range connectivity of the system disappears (or appears). This transition occurs abruptly when some generalized density in the system reaches a critical value (the so called percolation threshold). (For an overview of percolation theory, the reader may see the textbook by Stauffer and Aharony [133]).

In the improved model, bubble coalescence is considered by supposing that neighbouring sites where bubbles are growing form a larger cluster. The stationary occupation probability p of one site is still given by

$$p = \Theta = \frac{\lambda}{\eta + \lambda} \tag{7.11}$$

The *mean cluster size* is defined as

$$S = \sum_{s=0}^{\infty} w_s s \tag{7.12}$$

where w_s is the probability that the cluster to which an arbitrary occupied site belongs contains exactly s sites. This quantity has been calculated from numerical simulations on different kinds of lattices. A key result of percolation theory is the existence of a critical occupational probability p_c called *percolation threshold* at which the mean cluster size becomes infinite. This quantity was determined numerically for 2D square lattices. A criterion for the phase transition from bubble layer to gas film is then provided. It is postulated that a gas film is formed if an infinite cluster in an infinite lattice appears i.e. when the mean occupational probability reaches the percolation threshold p_c.

7.3   Electrochemical discharges for synthesis of nanoparticles

The inspiration to use electrochemical discharges to produce nanoparticles came from Oishi et al. [134]. In their work, anode discharge was conducted between a titanium anode and a LiCl-KCl-CaO melt under 1 atm of Ar at 723 K by applying 500 V dc. After anode-discharge electrolysis a black powder was obtained from the melt which was analysed to be titanium oxide particles having diameter smaller than 150 nm. They could also obtain oxide particles of iron, nickel or copper when the respective metal wires were used as anode.

In an aqueous electrolyte containing metal salt, with the working electrode as the cathode, suitable overpotential can lead to the deposition of metal atoms on the electrode surface; this is the standard electrochemical deposition process. However, if one passes over to the *spark region*, as described earlier, a gas film covers the cathode. Conditions created locally near the electrode are very different from what occurs when one does normal electrochemistry – (a) locally due to hydrogen production, pH can increase considerably, (b) temperature near electrode is much higher, (c) strong stirring is present and (d) current occurs in short bursts of discharges across the gas film. These conditions offer new ways for the production of nanoparticles. Most of the current is used up for production of H_2 bubbles but a part of it converts M^+ to M which group to form clusters. The clusters are prevented from depositing on the electrode surface by the gas film. What controls the size of these clusters is still an open question. Some discussion on this aspect will be provided in a later section.

7.4   Experimental

The setup used for the experiments is shown in Fig. 7.5. The electrochemical cell is adapted from a teflon cell made for use in electrolytical STM. A PYREX® glass is used as the base of the cell. Pt wire (300μm, 99.9%, Advent, England) is used as working electrode and a large ring also of Pt is used as counter electrode. A power supply that can provide about 40 Volts and several amperes of current is used. A micrometric z stage controls the depth of the electrode in the electrolyte. DC motor is used to rotate working electrode upto 5000 rpm. The rotating electrode solves two purposes. One, it stabilizes the gas film. Second, it can be used to control the particle size (described later).
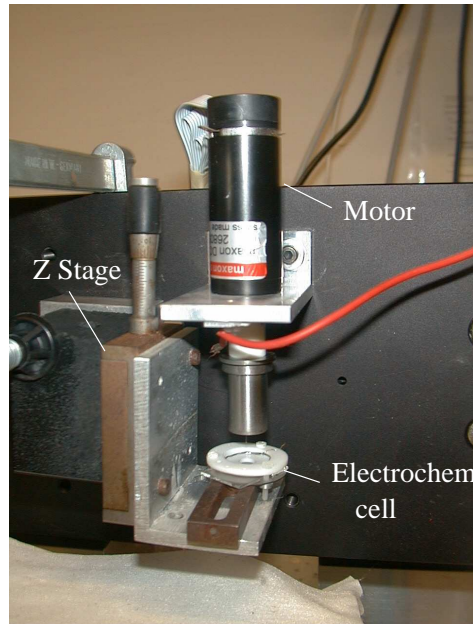
Figure 7.5: Photograph of the actual setup. The cell volume of the electrochemical cell is $\sim 1ml$.

Metal	Solution
Cu	$CuSO_4 + H_2SO_4$
Pt	$H_2PtCl_6 + HClO_4$
Au	$NaAuCl_4 + HClO_4$
$Au + Pt$	$H_2PtCl_6 + NaAuCl_4 + HClO_4$

Table 7.1: Solutions used for experiment

In all experiments a high concentration supporting electrolyte is used with a low concentration of metal salt. Table 7.1 provides a list of electrolytes used for different metal particles. The electrolytes tried are widely used for electrodeposition of the respective metals. During the experiment, which can last for a few hours, the solution volume is maintained constant by manually adding the supporting electrolyte. Steady state *I-V* curves are recorded before, after and sometimes in between the experiment to control that the experimental conditions are similar from start to finish. It is remarked that when the metal salt concentration is higher than about 10mM, there is non-negligible deposition of metal on the working electrode leading to a change in the surface conditions and thereby in the *I-V* curve.

To observe the size and shape of the metal particles, SEM (Scanning Electron Microscope) is used. Elemental composition of particles was determined by EDX (Energy Dispersive X-ray analysis) in certain cases. To observe under SEM or STM, particles thus produced are deposited on HOPG by simply putting a drop of electrolyte on the HOPG surface and

letting it dry. Of practical importance is that the metal salt should be almost completely used up else it will also crystallize on HOPG obscuring the nanoparticles. To observe the smallest particles by STM, the solutions were filtered using 0.01μm membrane filters (from GE Osmonics®).

7.5   Results and Discussion

The *I-V* curves for H_2PtCl_6 0.5mM + $HClO_4$ 1M at different rotation speeds are shown in Fig. 7.6 and for the different solutions used are shown in Fig. 7.7. The *I-V* curves are characteristic of the electrochemical discharge phenomenon described earlier. The first figure shows that V_{crit} depends on ω but we donot see any clear trend. The curves '2000rpm (before)' and '2000rpm (after)' are typical in the sense that after a few hours of continuous run, temperature of the solution rises and V_{crit} decreases with temperature [135]. Not surprisingly the differences of small concentrations of $PtCl_6^{2+}$ or $AuCl_4^+$ are negligible.

Platinum

One of the first results on Pt (Fig. 7.8) with no electrode rotation, shows a wide distribution of particles. The smallest visible are ~ 30 nm while there are several in the range of ~ 200 nm. EDX results (Fig. 7.9) confirm that particles are composed of Pt. The very large polycrystalline structures are probably particles that were deposited on the working electrode and which later on dropped into the solution. While the shape below 70 nm is unclear, at sizes ≥ 80 nm particles are mono crystals typical of Pt fcc crystal. Fig. 7.10 shows STM images of particles created at 2000 rpm. Evidently stable particles ≤ 10 nm size are also created by this method. Since no additives were added to the solutions to stabilize the particles from further growth, over a period of time, agglomeration is possible as seen in Fig. 7.10(b).

Copper

Copper shows distinctly different behaviour from the case of platinum. Fig. 7.11 and Fig. 7.12 show particles created from $CuSO_4 + H_2SO_4$ without electrode rotation. The smallest particles visible are < 50 nm and the largest 400 nm. All the particles are spherical in form. The lack of sharpness in the SEM images is due to incomplete usage of the $CuSO_4$ salt, which is then also present on the HOPG surface.

Platinum + Gold

There is considerable interest in alloy nano particles. Fig. 7.13 shows the results of our method using H_2PtCl_6 0.25 mM $+NaAuCl_4$ 0.25 mM $+HClO_4$ 1 M, with $\omega = 2000$ rpm. On the HOPG surface, there is a uniform distribution of particles ranging in size from 80 nm to 140 nm with the majority around 125 nm (Fig. 7.13(a). These particles appear spherical (Pt nano particles of this size were crystallites).

Interestingly on the HOPG surface at certain regions there exist very well defined cubic particles of ~ 400 nm, several of which are found close to each other. These are likely salt
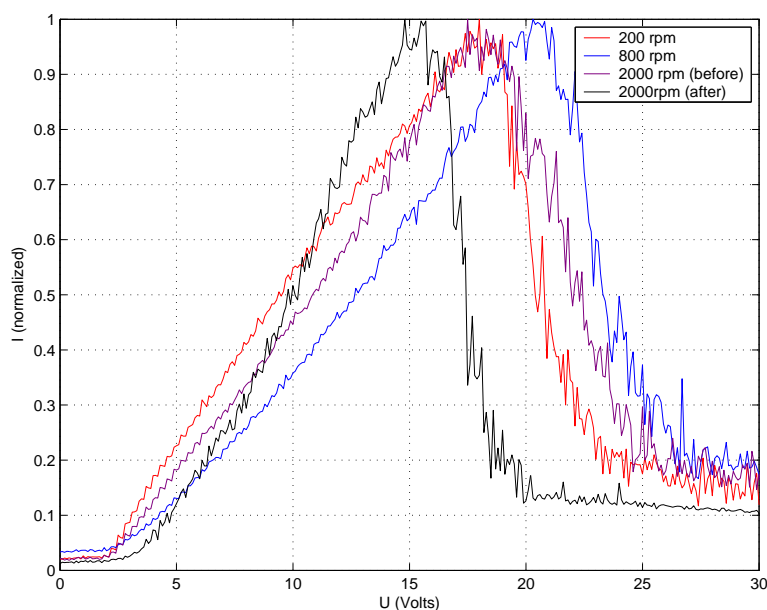
Figure 7.6: The *I-V* characteristics shown for different rotation speeds. Electrolyte: H_2PtCl_6 0.5mM $+HClO_4$ 1M, working electrode (Pt): $300\mu m$ dia, depth: 0.5mm. The curves 2000rpm (before) and (after) were taken before and after a $\sim$ 4 hour run at 25 V and $\sim$ 0.1 A. Potential scan speed : 10 V/s.
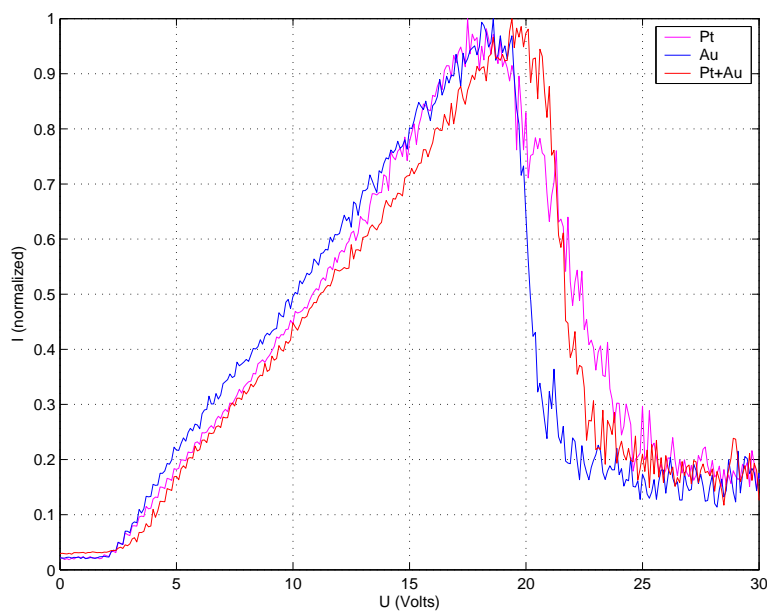
Figure 7.7: *I-V* curves for 3 different solutions. Pt: H_2PtCl_6 0.5 mM, Au:Na_2AuCl_4 0.5 mM, Pt+Au:H_2PtCl_6 0.25 mM $+$ Na_2AuCl_4 0.25 mM. Supporting electrolyte: $HClO_4$ 1 M, working electrode (Pt): $300\mu m$ dia, depth: 0.5 mm, rotation speed: 2000 rpm. Potential scan speed : 10 V/s.
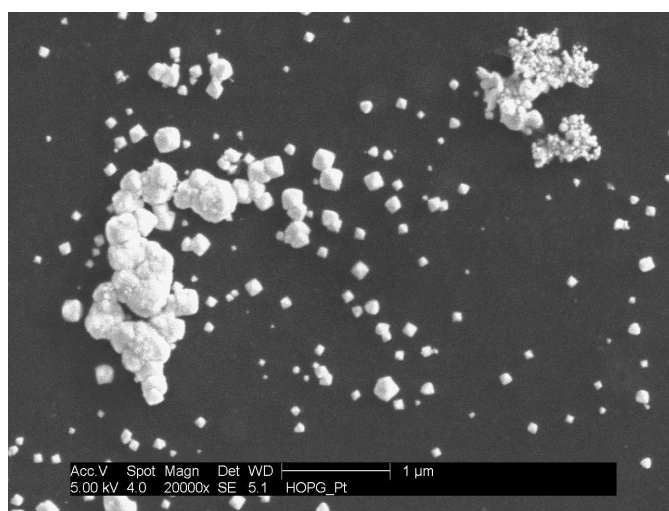
Figure 7.8: SEM micrograph of Pt nano and sub-micron particles formed by electrochemical discharges in $H_2PtCl_6 + HClO_4$.
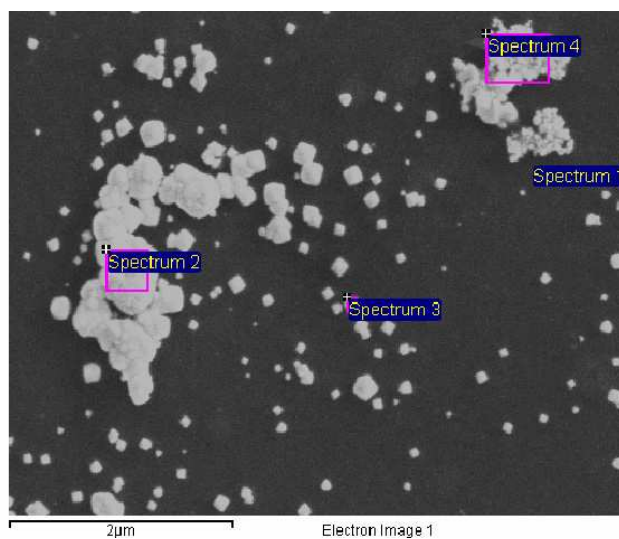
Spectrum	C	Pt	Total
Spectrum1	100	0	100
Spectrum2	4.82	95.18	100
Spectrum3	49.23	50.77	100
Spectrum4	22.68	77.32	100

All results in weight %.

Figure 7.9: SEM micrograph of Pt particles with the elemental composition at different regions measured by EDX.
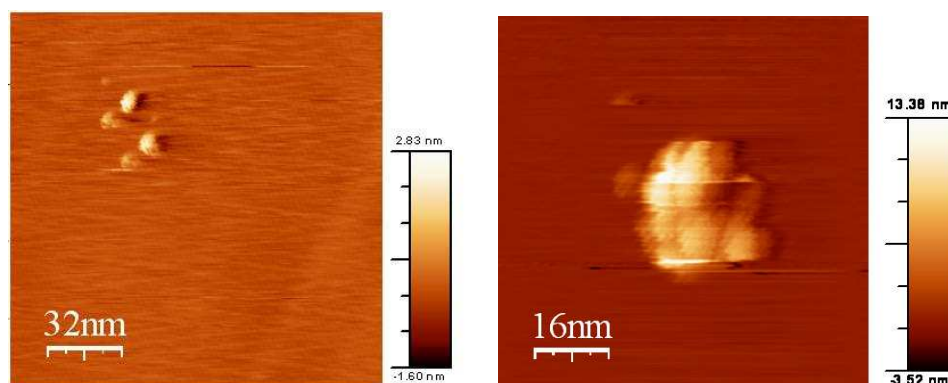
(a) STM images reveal ∼10 nm sized particles.

(b) Agglomerates are also possible.

Figure 7.10: STM images of Pt particles on HOPG, created under the conditions: H_2PtCl_6 0.5 mM + $HClO_4$ 1 M, $U = 30$ Volts, I 0.1 A, $\omega = 2000$ rpm. The solution was filtered using 0.01μm membrane filter.

Figure 7.11: SEM micrograph of Cu nano particles formed by electrochemical discharges in $CuSO_4 + H_2SO_4$.
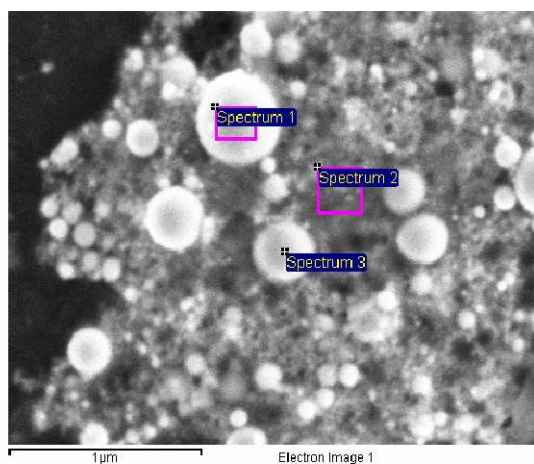
Spectrum	C	O	Si	S	Cu	Pt
Spectrum1	41.87	8.21	-	-	37.32	12.59
Spectrum2	23.19	39.73	5.08	18.41	5.78	7.80
Spectrum3	51.40	20.55	-	10.14	8.24	9.67

All results in atomic %.

Figure 7.12: SEM micrograph of Cu particles with the elemental composition at different regions measured by EDX.
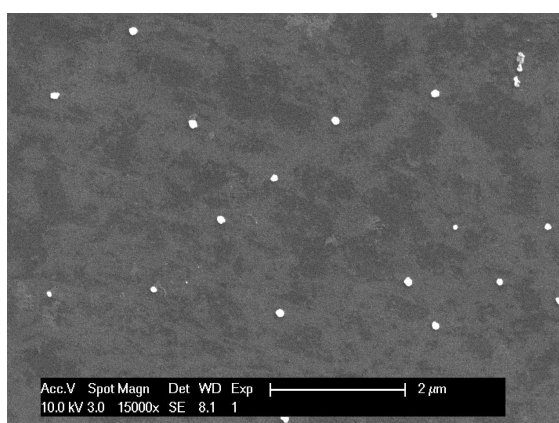
(a) Nano particles distributed uniformly over HOPG surface
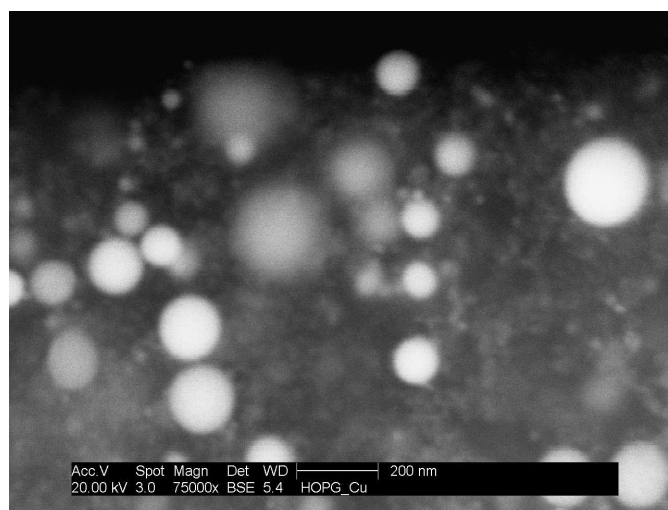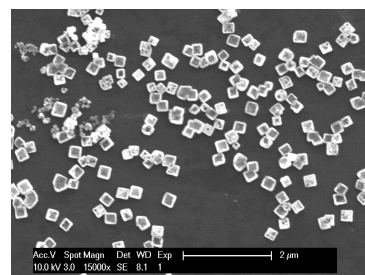

(b) Cubic particles, likely salt, present on some regions

Figure 7.13: SEM micrograph of nano particles formed by electrochemical discharges in $H_2PtCl_6 + NaAuCl_4 + HClO_4$ with $\omega = 2000$ rpm.

crystals formed during evaporation of the solution. The salt will crystallize where the last droplets of the solution remain explaining why these are found only at certain regions and why several of them are found close to each other.

7.6 Particle size

The mechanism of growth of particles is not well understood. One possibility is that the size is determined by the amount of electronic charge carried in each discharge and the concentration of metal ions near the gas film. A typical discharge lasts for about 10 μs and carries a current of about 1 A. For metal ions, M^+, with concentration of 0.5 mM and assuming that the discharge electron either creates a metal atom from M^+ or hydrogen atom from water in the ratio of their concentrations, one discharge gives a metal particle of $\sim$300 nm diameter. Formation of such a large particle in one go is unlikely. Moreover much smaller particles have been experimentally observed. The more probable growth mechanism is progressive nucleation – discharges produce metal atoms which form some stable nuclei which in turn grow by adding atoms during successive discharges. Agglomeration of small particles has also been observed.

We try to control the size of the particles by using a rotating electrode. The rotating electrode causes the solution near it to rotate too, which in turn provides centrifugal force to the particles to move away from the electrode. In the spark region of the $I-V$ characterisctic (Fig. 7.2), electrolyte flow near the working electrode is very difficult to estimate or measure. For this reason, a simple model, *Taylor-Couette flow*, is considered. This model should be sufficient to explain the basic idea of particle size control.

Taylor-Couette problem describes the flow of a fluid between concentric rotating cylinders. It is one of the most widely studied systems in classical fluid dynamics. For the case when the inner cylinder is rotating with angular velocity, ω, and the outer cylinder is at rest, the fluid velocity as a function of radius r is given by

$$v_\theta = \frac{\omega \kappa^2 r_o}{1 - \kappa^2} \left[\frac{r_o}{r} - \frac{r}{r_o} \right] \tag{7.13}$$

where v_θ is the angular velocity, $\kappa = \frac{r_i}{r_o}$, ratio of inner to outer radii, r_i and r_o are inner and outer radii respectively.

Under the assumption of Taylor-Couette flow, work done in bringing a particle of mass m from the outer radius, r_o, to a distance r from axis of rotation is given by

$$W_m(r) = \int_{r_o}^{r} m\Omega(r)^2 r dr = \int_{r_o}^{r} m \left\{ \frac{\omega \kappa^2 r_o}{1 - \kappa^2} \left(\frac{r_o}{r} - \frac{r}{r_o} \right) \frac{1}{r} \right\}^2 r dr \tag{7.14}$$

$\Omega(r)$ being the angular velocity at r.

This is the potential energy stored in the system when a particle of mass m is brought from r_o to r. Let us define as our system, all particles of mass m in the electrolyte. Further
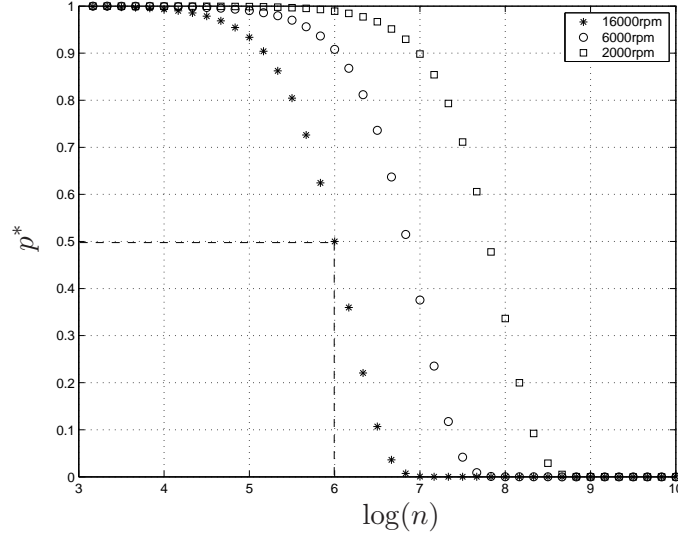
Figure 7.14: p^* (see text for definition) versus *cluster size*. *Pt* particles; $r_i = 0.5$ mm, $r_r = 0.525$ mm, $r_o = 10$ mm. The dashed line shows size corresponding to $(p^* = 0.5)$.

assuming that these particles do not coalesce with each other or with any other particles, then at thermal equilibrium, the system will follow Boltzmann stastistics:

$$p_m(W_m(r))\delta r = p_m(r)\delta r = \frac{\zeta(r)e^{-\frac{W_m(r)}{k_b T}}\delta r}{\int_{r_o}^{r_i} \zeta(r)e^{-\frac{W_m(r)}{k_b T}}\,dr} \tag{7.15}$$

where $p_m(W(r))\delta r$ is the fraction of particles between r and $r + \delta r$, $\zeta(r) \propto 2\pi r$ is the *density of states* at r.

We define the quantity p^* as

$$p^*(m) = \frac{\int_{r_i}^{r_r} p_m(r)dr}{\int_{r_i}^{r_r} p_{m\rightarrow 0}(r)dr} \tag{7.16}$$

where r_r is the radius in the electrolyte upto which the reaction $M^+ + e^- \rightarrow M$ can take place. $p^*(m)$ is the ratio of probability of finding a mass m particle to the probability of finding a zero mass particle in the reaction zone. Since the mass m is directly related to the number of atoms in the cluster, $p^*(m)$ can also be written as $p^*(n)$ or $p^*(\Phi)$ where n is the number of atoms and Φ is the diameter (assuming spherical particles) corresponding to mass m.

For the case of *Pt* atoms, and the geometry – $r_i = 0.5$ mm, $r_r = 0.525$ mm, $r_o = 10$ mm; p^* is plotted as a function of *cluster size* for different ω (Fig. 7.14).What it basically shows is that large particles have very low probability of being found near the gas film compared to small particles. The effect of ω, is better seen in the Fig. 7.15, which plots the diameter $\Phi(p^* = 0.5)$ versus ω assuming spherical particles.
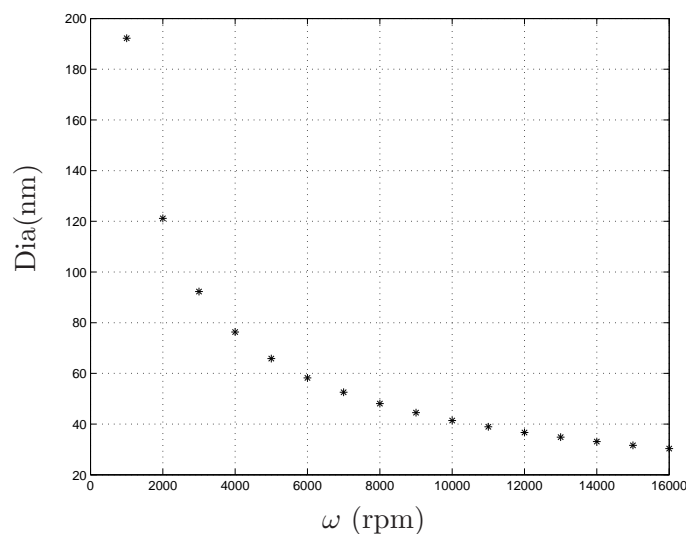
Figure 7.15: Size of clusters versus ω for $p^* = 0.5$. *Pt* particles; $r_i = 0.5mm$, $r_r = 0.525mm$, $r_o = 10mm$.

7.7 Outlook

In summary, a general and simple method to produce metal nano-particles based on the phenomenon of electrochemical discharges is demonstrated. This method allows to create particles from 10-150 nm and it works for several metals - *Cu, Pt, Au, Pt+Au*. A mechanism to control the size is developed based on rotation speed of the working electrode. It is estimated that this method should allow to control the size of particles to ~ 10 nm with readily available components.

The mechanism of nucleation and growth in this system is poorly understood. Further systematic studies of particle size distribution and composition should help clarify this. It appears that this method would be particularly suitable for production of alloy nanoparticles which is in general quite challanging. Due to the local increase in the pH near the tool electrode, this method may also be applicable for the production of metal oxide nanoparticles. Noble metal particles are of particular interest to the fuel cell community for their catalytical properties. The particles produced by our method need to be analysed for their catalytical behaviour. Future work should focus on these areas.

Chapter 8

Conclusion

Nanostructuring by Electrolytical STM is a field rich with possibilities. This thesis describes two methods for ESTM based nanostructuring – (a) deposition from adsorbed ions on the tip and (b) deposition by train of ultra-short voltage pulses. Mathematical models have been built to understand these and similar processes. Another related method based on electrochemical discharges has been developed to produce nanoparticles in large quantities.

8.1 Achievements

Modelling

An attempt has been made to quantitavily understand the important mechanisms involved in "structuring" induced by an ESTM tip. For a nanostructuring task multiple processes can take place simultaneously, however the dominant process can usually be identified. In particular three methods have been described – (a) double-layer mixing, (b) ultra-short voltage pulses and (c) diffusion governed deposition. Models based on finite difference method, developed during the course of the thesis can be used to estimate the charge and electric field distribution within the tip-substrate gap and thereby determine the structure size. The models provide important insights and are useful in optimization – e.g. it can be used to predict the optimal gap for structuring based on double-layer mixing or it can help predict the optimal pulse width for a given concentration while using ultrashort voltage pulses or it can be used to estimate the time needed to replenish ions into the zone below the tip. Some of the modelling results concerning double-layer charging by ultra-short voltage pulses and diffusion could be confirmed by experiments. For double-layer mixing, modelling results could be matched with some results found in literature.

Monte Carlo simulations have been used to predict the size of clusters that can form on the substrate surface under the ESTM tip. The analysis uses size of reaction zone and the number of metal atoms as inputs. This study is restricted to 2d growth with high binding energy between metal/substrate. A criterion is established for the formation of stable clusters – there exists a critical value of surface density of atoms above which large and therefore stable clusters are formed.

Pt on HOPG

The first system studied experimentally was Pt deposition on HOPG in a solution containing $[PtCl_6]^{2-}$ ions. The conclusion here is that a PtIr tip at equilibrium has a layer of $[PtCl_6]^{2-}$ ions adsorbed on the surface which can be deposited on the substrate by $\sim$1 μs, $\sim$5 V pulses (substrate negative). Two kinds of deposits were observed. One is relatively large deposits – $\sim$50 nm in diameter and $\sim$5 nm in height – usually on holes. In this case, given the large volume, tip atoms are also probably transferred to the substrate. The second type of deposits consists of several $\sim$5 nm diameter, $\leq$ 1nm high particles in a zone of about 50 nm. The purpose of the relatively high voltage is to either create defects and pin the Pt atoms or to ensure the formation of very small particles that are immobile on the surface. At lower voltages, tip oxidation or loosely fixed particles inhibit STM imaging. This system is very similar to localized Ag deposition on HOPG [7, 8].

Pt on Au(111)

The second system studied is Pt deposition on Au(111) also in $[PtCl_6]^{2-}$ containing electrolyte. Here a novel deposition technique has been evolved – a train of about 100 nanosecond pulses of $\sim$3 V, and $\sim$100 μs period creates clusters of diameter $\sim$10 nm and 1-2 monolayers high in a zone of about 50 nm. Depositon occurs from the $[PtCl_6]^{2-}$ ions adsorbed on the gold surface. The pulse parameters – pulse width, pulse period and number of cycles – play key roles in the deposition process. While their effects are interconnected, as a general rule – pulse width is responsible for the deposition size, pulse period is important for replenishment of ions and a critical number of cycles is needed to create stable clusters. This method of structuring is quite universal and should be applicable to a large number of systems.

Nanoparticles by electrochemical discharges

The phenomenon of electrochemical discharges has been applied to the generation of nanoparticles. The method has been shown to work for several metals – Cu, Pt, Au, Pt+Au. In order to obtain a well determined size of particles with narrow size distribution, the rotation speed of the working electrode has been identified as the key parameter and a relationship has been found connecting particle size and rotation speed. The likely mechanism of formation of nanoparticles is progressive nucleation and growth. From an application point of view, this method seems particularly suitable for large scale production of alloy nanoparticles.

8.2   Outlook

Models built in this work to explain structuring by ESTM can be improved in several ways. One key drawback of the model is the use of a fixed grid size in space. The consequence is that right below the tip, the number of grid points has to be kept small. This may lead to numerical artefacts in certain calculations. The use of variable grid size can lead to significant improvement without sacrificing simulation time. It would also be interesting to compare with other computational techniques like finite element or Monte Carlo.

Monte Carlo studies on 2d cluster formation suggest a phase transition between a phase containing several small clusters and a phase containing few very large clusters. Seen in this respect, the critical surface density of atoms is the transition point. This 'phase transition' should be analysed further specially with the percolation theory.

Localized deposition with ESTM using a train of ultra-short voltage pulses is proposed as a method applicable for several systems. Since deposition occurs from adsorbed ions on the sample surface, controlling the extent of adsorbtion is important. Experimentally this means combining potentiostaic control with nanosecond voltage pulses. In trying to model this method for Pt on Au(111), it is assumed that Pt atoms on Au(111) surface can diffuse by hopping from one lattice site to a neighbouring one. However the presence of adsorbed $[PtCl_6]^{2-}$ ions will modify the surface diffusion. Similarly adsorbtion of $[PtCl_6]^{2-}$ ions is going to be modified by the presence of Pt on the surface. Atomic resolution high speed STM inside electrolyte to resolve adsorbate dynamics may help to understand these issues.

The method of electrochemical discharges for fabrication of nanoparticles is yet to be well understood. Under the conditions that exist in the 'spark region', locally near the tool electrode there is significant change in pH and temperature, vigorous stirring is present and current occurs in short bursts of discharges across the gas film. Experimentally there is scope to profit from the extra-ordinary conditions during discharges – e.g. the extreme pH near the gas film may be used to produce metal oxide nanoparticles. At the theoretical level, a model is needed which takes these effects into account to explain the open questions – where do the particles form or in other words to what extent do the discharges penetrate into the electrolyte beyond the gas film; how are the particles transported out of the reaction zone – important to estimate the time spent in the reaction zone and therefore connected to the size of the particles. Investigations on particle size distribution and particle composition should help to better understand the mechanism of particle formation.

Appendix A

Basics of nucleation and growth

Supersaturation

Nucleation process is understood as a first order phase transition where the driving force is the quantity

$$\Delta\mu \equiv (G_{old} - G_{new})/M \equiv \mu_{old} - \mu_{new} \tag{A.1}$$

known as *supersaturation* where G_{old} and G_{new} are the minimum Gibbs free energy of the old and the new phases respectively (Fig. A.1) and M is the total number of molecules (or atoms). (μ_{old} and μ_{new} are, respectively, the chemical potentials of the old and new phases at the corresponding minima.) This basic equation holds for a large number of processes - condensation of vapours, boiling, evaporation, sublimation, condensation of solute etc.

Of interest to us is electrochemical deposition ($\varphi < \varphi_e$). In this case the old phase is an electrolyte containing M^+ and the new phase is the electrolyte without M^+ which in turn is deposited on the electrode as M. φ_e is the equilibrium or *Nernst* potential. The role of the chemical potentials is now played by the respective electrochemical potentials $\overline{\mu}_{old}$ and $\overline{\mu}_{new}$ so that eq. (A.1) is replaced by

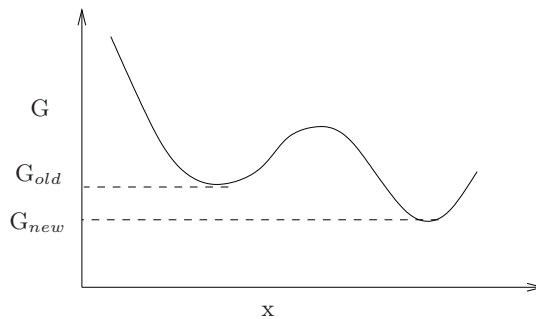$$\Delta\mu \equiv \overline{\mu}_{old} - \overline{\mu}_{new} \tag{A.2}$$

Figure A.1: Gibbs free energy for two phases shown against a generalized coordinate x. The generalized coordinate could be temperature, pressure, potential etc.
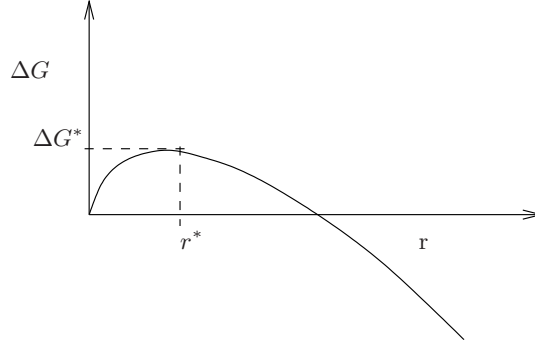
Figure A.2: Gibbs free energy change versus cluster size. r^* is the critical nucleus radius and ΔG^* is the energy barrier to be overcome.

This further simplifies to

$$\Delta\mu(\varphi) = z_i e \eta \tag{A.3}$$

where z_i is the valency of the solute ions, e is the electronic charge and $\eta \equiv \varphi_e - \varphi$ is the overpotential.

Nucleus size

For the case of homogeneous nucleation, change in the Gibbs free energy for the formation of a cluster of size n is given by

$$\Delta G(n) = -\Delta\mu n + S(n) \tag{A.4}$$

where $S(n)$ is the term associated with the formation of the interface between the two phases. For a 3-dimensional spherical cluster of radius r, $n \propto r^3$ and $S(n) \propto r^2$. Then eq.(A.4) becomes

$$\Delta G(n) = -\Delta\mu \frac{r^3}{r_o^3} + \sigma(r) 4\pi r^2 \tag{A.5}$$

where σ is the surface energy per unit area and r_o is the radius of an individual atom/molecule. For a 2-dimensional circular cluster

$$\Delta G(n) = -\Delta\mu \frac{r^2}{r_o^2} + \lambda(r) 2\pi r \tag{A.6}$$

where λ is the line energy per unit length.

The plot of ΔG vs r is shown in Fig. A.2. From this figure one sees that the newly formed nucleus is stable only when its radius exceed a critical size, r^*. A nucleus smaller than r^* dissolves into the solution to reduce the overall free energy, while a nucleus larger than r^* is stable and continues to grow bigger. ΔG^* is the energy barrier that a nucleation process must overcome.

For the case of heterogeneous nucleation (nucleation on a substrate), the expressions are modified due to an additional interface but the basic idea remains the same.

Rate of nucleation

A nucleus is formed from a critical number of adatoms randomly distributed over the surface, represented as

$$nM_{ad} \leftrightarrow (M_n)_{nucleus} \tag{A.7}$$

For a 2-d cluster formed by electrochemical deposition, the formation of the nucleus could be a slow process and the rate may be governed by the rate of production of M_{ad}. Then the rate of formation of nuclei is related to the overpotential η. From eq. (A.6) one can show that

$$\Delta G^* = \frac{(\pi \lambda r_o)^2}{z_i e \eta} \tag{A.8}$$

From this the rate equation can be written as

$$k_n = N_0 D_c \Gamma exp(-\frac{(\pi \lambda r_o)^2}{k_B T z_i e \eta})$$
$$k_n = k_n^0 exp(-\frac{a}{\eta}) \tag{A.9}$$

where N_0 is the number of active sites for nucleation, D_c is the adatom flux and Γ is a hydrodynamic factor.

For 3-d nucleation the rate equation becomes

$$k_n = k_n^0 exp(-\frac{b}{\eta^2}) \tag{A.10}$$

Various theories take into account the fact that the number of nuclei formed on possible sites is a function of time. Fleischmann and Thirsk [136] assumed that all possible sites of nucleation are active sites of identical reactivity toward nucleation. They further considered that the probability of conversion of these sites to nuclei is constant over time. Consequently the nucleation rate can then be written as the rate of disappearance of active sites according to the first order kinetic expression

$$\frac{dN(t)}{dt} = k_n(\eta)[N_0 - Nt] \tag{A.11}$$

where η is the overpotential, $k_n(\eta)$ is the rate constant of nucleation for one site (s^{-1}), N_0 is the number of active sites available per unit surface area which is regarded as independant of η. Integrating eq. (A.11) with the initial conditions $N = 0$ at $t = 0$, one obtains

$$N(t) = N_0[1 - exp(-k_n(\eta)t] \tag{A.12}$$

The value of N increases with time and tends towards the limiting value N_0. Two limiting cases can be considered depending on the value of k_n :

1. For very large k_n, the nucleation rate is high and given by:

$$\frac{dN}{dt} = N_0 \delta(t) \tag{A.13}$$

where $\delta(t)$ is the Dirac delta function. Nucleation takes place at $t = 0$ on all active sites; this is known as *instantaneous nucleation*.

2. For very low k_n and for short times, eq. (A.11) can be expanded as

$$N(t) = k_n N_0 t \qquad (A.14)$$

The number of nuclei increases linearly with time. In this case nuclei are formed continuously over time and this is termed as *progressive nucleation.*

Markov and Kashchiev [137] considered several types of active sites with different critical overpotential of nucleation, η_c, coexisting at the electrode surface. In this case the maximum number of nuclei is equal to the number of active centres at a given value of supersaturation:

$$N_s = \int_0^\eta z(\eta_c) d\eta_c \qquad (A.15)$$

where η is the applied overpotential, η_c is the critical overpotential at which a potentially active site will be activated, and $z(\eta_c)$ is the function that expresses the density of active sites for which the critical overpotantial has the value of η_c. This general expression can also be written as

$$N(t) = N_s(\eta)[1 - exp(-k_n(\eta)t] \qquad (A.16)$$

where $N_s(\eta)$ is the number of saturated active sites, which depends on η.

Fletcher and Lwin [138] have proposed a model that considers different rates of nucleation on differet types of active sites. *"Nucleation rates depend non-linearly on activation energies, so that only a small spread in activation energies at different active sites would be sufficient to create a rather broad distribution of nucleation rates".* Under the assumption that all active sites have the same nucleation overpotential, one gets the following equation:

$$N_t = \int_0^\infty N_\infty[1 - exp(-k_n(\eta)t]\Theta(k)dk \qquad (A.17)$$

where N_∞ is the total number of active sites, $k_n(\eta)$ is the kinetic constant at nucleation sites and $\Theta(k)dk$ is the fraction of active sites with a rate constant between k and $k + dk$. Extrapolation to long times gives $\lim_{t\to\infty} N(t) = N_\infty$.

Growth of clusters

Dominant mode of growth of clusters is by addition of monomers. Monomer attachment frequency could be

- volume diffusion controlled

- surface diffusion controlled

- direct impingement controlled

- interface transfer controlled

Coalescence may also play an important role in the growth of clusters.

Appendix B

Metal Deposition Mechanisms

[Adapted from Budevski et al. [139].]

A metal, Me, is electrochemically deposited on an electrode, S, by making the electrode potential more negative than the Nernst equilibrium potential $E_{Me/Me^{z+}}$. This is known as *overpotential deposition (OPD)*. In certain cases several monolayers of Me can be deposited on S at potentials slightly positive of the equilibrium potential – *underpotential deposition (UPD)*. Electrochemical deposition is influenced by a number of factors - charge transfer, mass transport, chemical reaction steps. In the limit of deposition occuring near the thermodynamic equilibrium, i.e. when kinetic influence can be ignored, two factors play the dominant roles : (i) the binding energy between adsorbed metal and substrate and (ii) the crystallographic misfit between Me and S. Following the notations of Budevski et al. [139], we define

$\Psi_{Me_{ads}-Me} =$ Binding energy between Me_{ads} and Me
$\Psi_{Me_{ads}-S} =$ Binding energy between Me_{ads} and S

Three different growth modes are identified based on the parameters - binding energy and crystallographic misfit.

- Volmer-Weber growth – When $\Psi_{Me_{ads}-Me} > \Psi_{Me_{ads}-S}$, growth occurs on the substrate by the formation of 3-d islands. In this case at Nernst equilibrium the concentration of Me_{ads} on the substrate is quite low, therefore growth occurs on unmodified substrate. Crystallographic misfit plays no role here.

- Frank-van der Merwe growth – When $\Psi_{Me_{ads}-Me} < \Psi_{Me_{ads}-S}$ and there is negligible crstallographic misfit, growth occurs layer-by-layer or epitaxially. Since $\Psi_{Me_{ads}-Me} < \Psi_{Me_{ads}-S}$, several monolayers of Me can already exist on S at equilibrium (UPD deposition).

- Stranski-Krastanov growth – When $\Psi_{Me_{ads}-Me} < \Psi_{Me_{ads}-S}$ and there is considerable crstallographic misfit, the 2-d UPD phase of Me_{ads} on the substrate can have a different structure compared to the bulk Me phase. Then initial growth is in the form of layers

125
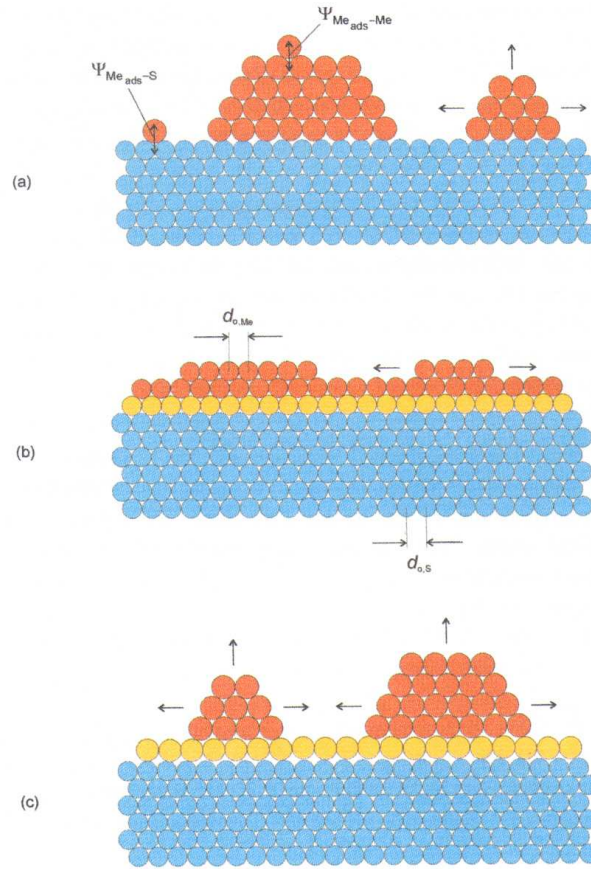
Figure B.1: Schematic representation of different growth modes in metal (Me) deposition on foreign substrate (S). (a) "Volmer-Weber" growth mode (Me island formation), (b) "Frank-van der Merwe" growth mode (Me layer-by-layer formation), and (c) "Stranski-Krastanov" growth mode (Me island on layer). From reference [139].

> upto a few monolayers (which often carry internal strain) and subsequent growth occurs in the form of 3-d islands on the underlying layers. The misfit between the initial 2-d phase and the 3-d Me phase is removed by dislocation defects.

In systems where Me UPD is formed, alloy formation between Me and S is also possible. Often these 2-d or 3-d alloy phases act as centres for nucleation and growth for 3-d Me phase in OPD range.

Bibliography

[1] P. Vettiger, M. Despont, U. Drechsler, U. Drig, W. Hberle, M. I. Lutwyche, H. E. Rothuizen, R. Stutz, R. Widmer, and G. K. Binnig, IBM Journal of Research and Development **44**, 311 (2000).

[2] D. M. Kolb and F. C. Simeone, Electrochim. Acta **50**, 2989 (2005).

[3] E. Budevski, G. Staikov, and W. J. Lorenz, Electrochim. Acta **45**, 2559 (2000).

[4] Z. X. Xie and D. M. Kolb, J. Electroanal. Chem. **481**, 177 (2000).

[5] S. G. Garcia, D. R. Salinas, C. E. Mayer, W. J. Lorenz, and G. Staikov, Electrochim. Acta **48**, 1279 (2003).

[6] P. Zahl, M. Bierkandt, S. Schrder, and A. Klust, Rev. Sci. Instrum. **74**, 1222 (2003).

[7] W. Li, J. A. Virtanen, and R. M. Penner, Appl. Phys. Lett. **60**, 1181 (1992).

[8] W. Li, G. S. Hsiao, D. Harris, R. M. Nyffenegger, J. A. Virtanen, and R. M. Penner, J. Phys. Chem. **100**, 20103 (1996).

[9] R. Schuster, V. Kirchner, X. H. Xia, A. M. Bittner, and G. Ertl, Phys. Rev. Lett. **80**, 5599 (1998).

[10] R. Wüthrich, C. Comninellis, and H. Bleuler, Electrochim. Acta **50**, 5242 (2005).

[11] G. Binnig, H. Rohrer, C. Gerber, and E. Weibel, Appl. Phys. Lett. **40**, 178 (1982).

[12] G. Binnig, H. Rohrer, C. Gerber, and E. Weibel, Physica B+C **109 & 110**, 2075 (1982).

[13] G. Binnig, H. Rohrer, C. Gerber, and E. Weibel, Phys. Rev. Lett. **50**, 120 (1983).

[14] G. Binnig, C. F. Quate, and C. Gerber, Phys. Rev. Lett. **56**, 930 (1986).

[15] R. Wiesendanger, *Scanning Probe Microscopy and Spectroscopy* (Cambridge University Press, 1994), section 1.2.

[16] J. Bardeen, Phys. Rev. Lett. **6**, 57 (1961).

[17] J. G. Simmons, J. Appl. Phys. **34**, 1793 (1963).

[18] R. Wiesendanger, *Scanning Probe Microscopy and Spectroscopy* (Cambridge University Press, 1994), chap. 8.

[19] M. A. McCord and R. F. W. Pease, Appl. Phys. Lett. **50**, 569 (1987).

[20] T. R. Albrecht, Ph.D. thesis, Stanford University (1989).

[21] M. F. Crommie, C. P. Lutz, and D. M. Eigler, Science **262**, 218 (1990).

[22] D. Eigler and E. Schweizer, Nature **344**, 524 (1990).

[23] Y. Sugimoto, M. Abe, S. Hirayama, N. Oyabu, O. Custance, and S. Morita, Nature Materials **4**, 156 (2005).

[24] M. Ringger, H. R. Hidber, R. Schlögl, P. Oelhafen, and H.-J. Güntherodt, Appl. Phys. Lett. **46**, 832 (1985).

[25] T. R. Albrecht, M. M. Dovek, M. D. Kirk, C. A. Lang, C. F. Quate, and D. P. E. Smith, Appl. Phys. Lett. **55**, 1727 (1989).

[26] R. M. Penner, M. J. Heben, N. S. Lewis, and C. F. Quate, Appl. Phys. Lett. **58**, 1389 (1991).

[27] H. J. Mamin, Appl. Phys. Lett. **69**, 433 (1996).

[28] D. M. Kolb, Electrochim. Acta **45**, 2387 (2000).

[29] R. Sonnenfeld and P. K. Hansma, Science **232**, 211 (1986).

[30] P. Lustenberger, H. Rohrer, R. Christoph, and H. Siegenthaler, J. Electroanal. Chem. **243**, 225 (1988).

[31] J. Wiechers, T. Twomey, D. M. Kolb, and R. J. Behm, J. Electroanal. Chem. **248**, 451 (1988).

[32] C. E. Bach, R. J. Nichols, W. Beckmann, H. Meyer, A. Schulte, J. O. Besenhard, and P. D. J. koudakis, J. Electrochem. Soc. **140**, 1281 (1993).

[33] J. Wiechers, T. Toomey, D. M. Kolb, and R. J. Behm, J. Electroanal. Chem. **248**, 451 (1988).

[34] L. A. Nagahara, T. Thundat, and S. M. Lindsay, Rev. Sci. Instrum. **60**, 3128 (1989).

[35] M. Dietterle, T. Will, and D. M. Kolb, Surf. Sci. **327**, L495 (1995).

[36] J. F. W. M. Poensgen, J. Frohn, M. Giesen, and H. Ibach, Surf. Sci. **274**, 430 (1992).

[37] M. Giesen, R. Randler, S. Baier, H. Ibach, and D. M. Kolb, Electrochim. Acta **45**, 527 (1999).

[38] M. Giesen and D. M. Kolb, Surf. Sci. **468**, 149 (2000).

[39] A. S. Dakkouri, Solid State Ionics **94**, 99 (1997).

[40] E. Budevski, G. Staikov, and W. J. Lorenz, *Electrochemical phase formation and growth : an introduction to the initial stages of metal deposition* (VCH Verlagsgessellschaft mbH, Weinheim, Germany, 1996).

[41] H.-F. Waibel, M. Kleinert, L. A. Kibler, and D. M. Kolb, Electrochim. Acta **47**, 1461 (2002).

[42] L. A. Kibler, M. Kleinert, and D. M. Kolb, Surf. Sci. **461**, 155 (2000).

[43] M. A. Schneeweiss, D. M. Kolb, D.-Z. Liu, and D. Mandler, Can. J. Chem. **75**, 1703 (1997).

[44] H. Hagenström, M. A. Schneeweiss, and D. M. Kolb, Langmuir **15**, 2435 (1999).

[45] G. E. Poirier, Chem. Rev. **97**, 1117 (1997).

[46] G. Nagy, J. Electroanal. Chem. **409**, 19 (1996).

[47] G. Nagy and T. Wandlowski, Langmuir **19**, 10271 (2003).

[48] M. Hugelmann and W. Schindler, Surf. Sci. **541**, L643 (2003).

[49] W. Schindler, M. Hugelmann, and P. Hugelmann, Electrochim. Acta **50**, 3077 (2005).

[50] W. J. Lorenz, G. Staikov, W. Schindler, and W. Wiesbeck, J. Electrochem. Soc. **149**, K47 (2002).

[51] D. M. Kolb, G. E. Engelmann, and J. C. Ziegler, Solid State Ionics **131**, 69 (2000).

[52] D. M. Kolb, R. Ullmann, and T. Will, Science **275**, 1097 (1997).

[53] R. Ullmann, T. Will, and D. M. Kolb, Chem. Phys. Lett **209**, 238 (1993).

[54] D. M. Kolb, R. Ullmann, and J. C. Ziegler, Electrochim. Acta **43**, 2751 (1998).

[55] G. E. Engelmann, J. C. Ziegler, and D. M. Kolb, Surf. Sci. **401**, L420 (1998).

[56] G. E. Engelmann, J. C. Ziegler, and D. M. Kolb, J. Electrochem. Soc. **145**, L33 (1998).

[57] W. Schindler, D. Hofmann, and J. Kirschner, J. Electrochem. Soc. **148**, C124 (2001).

[58] D. Hofmann, W. Schindler, and J. Kirschner, Appl. Phys. Lett. **73**, 3279 (1998).

[59] W. Schindler, P. Hugelmann, M. Hugelmann, and F. X. Kärtner, J. Electroanal. Chem. **522**, 49 (2002).

[60] R. Widmer and H. Siegenthaler, Electrochem. Commun. **7**, 421 (2005).

[61] R. L. McCarley, S. A. Hendricks, and A. J. Bard, J. Phys. Chem. **96**, 10089 (1992).

[62] C. Lebreton and Z. Z. Wang, J. Vac. Sci. Technol. B **14**, 1356 (1995).

[63] C. Lebreton and Z. Z. Wang, Surf. Sci. **382**, 193 (1997).

[64] T. Solomun and W. Kautek, Electrochim. Acta **47**, 679 (2001).

[65] J. R. LaGraff and A. A. Gewirth, J. Phys. Chem. **98**, 11246 (1994).

[66] M. Kock, V. Kirchner, and R. Schuster, Electrochim. Acta **48**, 3213 (2003).

[67] R. Schuster, V. Kirchner, P. Allongue, and G. Ertl, Science **289**, 98 (2000).

[68] V. Kirchner, X. Xia, and R. Schuster, Acc. Chem. Res. **34**, 371 (2001).

[69] A. L. Trimmer, J. L. Hudson, M. Kock, and R. Schuster, Appl. Phys. Lett. **82**, 3327 (2003).

[70] S. H. Ahn, S. Ryu, D. K. Choi, and C. N. Chu, Precision Engineering **28**, 129 (2004).

[71] J. A. Kenney, G. S. Hwang, and W. Shin, Appl. Phys. Lett. **84**, 3774 (2004).

[72] R. T. Pötzschke, G. Staikov, W. J. Lorenz, and W. Wiesbeck, J. Electrochem. Soc. **146**, 141 (1999).

[73] P. Berenz, X. Xiao, and H. Baltruschat, J. Phys. Chem. B **106**, 3673 (2002).

[74] X. Xiao, M. Nielinger, and H. Baltruschat, Electrochim. Acta **48**, 3093 (2003).

[75] P. Buffat and J.-P. Borel, Phys. Rev. A **13**, 2287 (1976).

[76] K. F. Peters, J. B. Cohen, and Y.-W. Chung, Phys. Rev. B **57**, 13430 (1998).

[77] S. H. Choi, K. L. Wang, M. S. Leung, G. W. Stupian, N. Presser, B. A. Morgan, R. Robertson, M. Abraham, E. E. King, B. Teuling, et al., J. Vac. Sci. Technol. A **18**, 1326 (2000).

[78] R. Rossetti, S. Nakahara, and L. E. Brus, J. Chem. Phys. **79**, 1086 (1983).

[79] R. Grisel, K.-J. Weststrate, A. Gluhoi, and B. E. Nieuwenhuys, Gold Bull. **35**, 39 (2002).

[80] G. C. Bond, Gold Bull. **34**, 117 (2001).

[81] Y. Takasu, N. Ohashi, X.-G. Zhang, Y. Murukami, H. Minagawa, S. Sato, and K. Yahikozawa, Electrochim. Acta **41**, 2595 (1996).

[82] O. Savadogo and A. Essalik, J. Electrochem. Soc. **143**, 1814 (1996).

[83] J. A. A. van den Tillaart, B. F. M. Kuster, and G. B. Marin, Catal. Lett. **36**, 31 (1996).

[84] T. Frelink, W. Visscher, and J. A. R. van Veen, J. Electroanal. Chem. **382**, 65 (1995).

[85] G. Cao, *Nanostructures and Nanomaterials. Synthesis, Properties and Applications* (Imperial College Press, London, 2004).

[86] K.-H. Meiwes-Broer, ed., *Metal Clusters at Surfaces. Structure, Quantum Properties, Physical Chemistry* (Springer Verlag, Berlin, 2000).

[87] J. Turkevich, J. Hillier, and P. C. Stevenson, Discuss. Faraday Soc. **11**, 55 (1951).

[88] A. Henglein, B. G. Ershov, and M. Malow, J. Phys. Chem. **99**, 14129 (1995).

[89] M. Boutonnet, J. Kizling, and P. Stenius, Colloids Surf. **5**, 209 (1982).

[90] M. L. Steigerwald, A. P. Alivisatos, J. M. Gibson, T. D. Harris, R. Kortan, A. J. Muller, A. M. Thayer, T. M. Duncan, D. C. Douglas, and L. E. Brus, J. Am. Chem. Soc. **110**, 3046 (1988).

[91] J. D. Jackson, *Classical Electrodynamics* (John Wiley, New York, 1998).

[92] H. L. von Helmholtz, Wied. Ann. **7**, 337 (1879).

[93] G. Gouy, J. Chem. Phys. **9**, 457 (1910).

[94] D. L. Chapman, Philos. Mag. **25**, 475 (1913).

[95] O. Stern, Z. Electrochem. **30**, 508 (1924).

[96] D. C. Grahame, Chem. Rev. **41**, 441 (1947).

[97] A. J. Bard and L. R. Faulkner, *Electrochemical methods : fundamentals and applications* (Wiley, 2000), section 1.2.

[98] A. J. Bard and L. R. Faulkner, *Electrochemical methods : fundamentals and applications* (Wiley, 2000), section 13.3.

[99] A. N. Frumkin, Z. Physik. Chem. **164A**, 121 (1933).

[100] J. Hoshen and R. Kopelman, Phys. Rev. B **14**, 3438 (1976).

[101] H. Huang, G. H. Gilmer, and T. D. de la Rubia, J. Appl. Phys. **84**, 3636 (1998).

[102] C. L. Liu, J. M. Cohen, J. B. Adams, and A. Voter, Surf. Sci. **253**, 334 (1991).

[103] D. W. Pohl, IBM Journal of Research and Development **30**, 417 (1986).

[104] K. Besocke, Surf. Sci. **181**, 145 (1987).

[105] P. Zahl, M. Bierkandt, S. Schrder, and A. Klust, Rev. Sci. Instrum. **74**, 1222 (2003).

[106] Http://gxsm.sourceforge.net/.

[107] J. P. Ibe, P. P. Bey, S. L. Brandow, R. A. Brizzolara, N. A. Burnham, D. P. DiLella, K. P. Lee, C. R. K. Marrian, and R. J. Corlton, J. Vac. Sci. Technol. A **8**, 3570 (1990).

[108] Y. Nakamura, Y. Mera, and K. Maeda, Rev. Sci. Instrum. **70**, 3373 (1999).

[109] J. V. Zoval, J. Lee, S. Gorer, and R. M. Penner, J. Phys. Chem. B **102**, 1166 (1998).

[110] F. Gloaguen, J. M. Leger, C. Lamy, A. Marmann, U. Stimming, and R. Vogel, Electrochim. Acta **44**, 1805 (1999).

[111] G. Lu and G. Zangari, J. Phys. Chem. B **109**, 7998 (2005).

[112] J. L. Zubimendi, L. Vazquez, P. Ocon, J. M. Vara, W. E. Triaca, R. C. Salvarezza, and A. J. Arvia, J. Phys. Chem. **97**, 5095 (1993).

[113] I. Lee, K.-Y. Chan, and D. L. Phillips, Appl. Surf. Sci. **136**, 321 (1998).

[114] I. Lee, K.-Y. Chan, and D. L. Phillips, Ultramicroscopy **75**, 69 (1998).

[115] K. Uosaki, S. Ye, H. Naohara, Y. Oda, T. Haba, and T. Kondo, J. Phys. Chem. B **101**, 7566 (1997).

[116] E. Bauer and J. H. van der Merwe, Phys. Rev. B **33**, 3657 (1986).

[117] J. Clavilier, R. Faure, G. Guinet, and R. Durand, J. Electroanal. Chem. **107**, 205 (1980).

[118] Y. Uchida and G. Lehmpfuhl, Surf. Sci. **243**, 193 (1991).

[119] N. Batina, A. S. Dakkouri, and D. M. Kolb, J. Electroanal. Chem. **370**, 87 (1994).

[120] M. Dietterle, T. Will, and D. M. Kolb, Surf. Sci. **327**, L495 (1995).

[121] H. Fizeau and L. Foucault, Annales de Chimie et de Physique XI, 3ème série p. 370 (1844).

[122] C. Guilpin and J. Garbaz-Olivier, Spectrochimica Acta B **32**, 155 (1977).

[123] H. Vogt, Electrochim. Acta **42**, 2695 (1997).

[124] H. Kurafuji and K. Suda, Annals of the CIRP **16**, 415 (1968).

[125] B. Bhattacharyya, B. N. Doloi, and S. K. Sorkhel, Journal of Materials Processing Technology **95**, 145 (1999).

[126] Y. P. Singh, V. K. Jain, P. Kumar, and D. C. Agarwal, Journal of Materials Processing Technology **58**, 24 (1996).

[127] R. Wüthrich and V. Fascio, International Journal of Machine Tools and Manufacture **45**, 1095 (2005).

[128] R. Wüthrich, K. Fujisaki, P. Couthy, L. Hof, and H. Bleuler, Journal of Micromechanics and Microengineering **15**, S276 (2005).

[129] P. Boissonneau and P. Byrne, Journal of Applied Electrochemistry **30**, 767 (2000).

[130] L. J. J. Janssen, Electrochim. Acta **34**, 161 (1989).

[131] V. Fascio, Ph.D. thesis, Swiss Federal Institute of Technology, EPF Lausanne (2002), 2691.

[132] R. Wüthrich, Ph.D. thesis, Swiss Federal Institute of Technology, EPF Lausanne (2003).

[133] D. Stauffer and A. Aharony, *Introduction to Percolation Theory* (Taylor & Francis, London, 1998).

[134] T. Oishi, T. Goto, and Y. Ito, J. Electrochem. Soc. **149**, D155 (2002).

[135] R. Wüthrich and L. Hof, International Journal of Machine Tools and Manufacture **46**, 828 (2006).

[136] M. Fleischmann and H. R. Thirsk, Electrochim. Acta **2**, 22 (1960).

[137] I. Markov and D. Kashchiev, Jornal of Crystal Growth **13-14**, 131 (1972).

[138] S. Fletcher and T. Lwin, Electrochim. Acta **28**, 237 (1983).

[139] E. Budevski, G. Staikov, and W. J. Lorenz, *Electrochemical phase formation and growth : an introduction to the initial stages of metal deposition* (VCH Verlagsgessellschaft mbH, Weinheim, Germany, 1996), section 1.2.

Curriculum Vitae

Ashwin LAL

Date of Birth	24.01.1975
Nationality	Indian
Address	Chemin d'Entre-Bois 59, Lausanne 1018, Switzerland
email	ashwin.lal@epfl.ch

Educational Qualification & Job experience

Sept. 2003-2007	Ecole Polytechnique Fédérale de Lausanne (EPFL), Switzerland
	Ph.D. project at the Laboratoire de systemes robotiques
Sept. 2001-Aug. 2003	Ecole Polytechnique Fédérale de Lausanne (EPFL), Switzerland
	Project on Positioning and Sensing with Scanning Probe and
	Nanometric Scale Reference
Apr. 2000-Aug. 2001	AIMIL Ltd., New Delhi, India
	Development engineer at Institute for Research and
	Product Development
Apr. 1999-Mar. 2000	Applied Materials South East Asia, Singapore
	Field serveice engineer for physical vapour deposition systems
Sept. 1998-Apr. 1999	Indian Institute of Technology, New Delhi, India
	Project work
1993-1998	Indian Institute of Technology, Kanpur, India
	M.Sc. Physics (Integrated)

Computing

C, Matlab, Mathematica, LabView, ProEngineer, Ansys (beginner).
Systems – Windows, Linux, Unix.

Languages

Hindi, English, French (working knowledge).